UNIVERSITY OF OKLAHOMA

GRADUATE COLLEGE

PHASE-CORRECTING DATA ASSIMILATION AND APPLICATION TO STORM-SCALE WEATHER PREDICTION

A Dissertation

SUBMITTED TO THE GRADUATE FACULTY

in partial fulfillment of the requirements for the

degree of

Doctor of Philosophy

By

KEITH A. BREWSTER
Norman, Oklahoma
1999

UMI Number: 9940297

PHASE-CORRECTING DATA ASSIMILATION
AND APPLICATION TO STORM-SCALE
WEATHER PREDICTION

A DISSERTATION APPROVED FOR
THE SCHOOL OF METEOROLOGY

BY

Frederick H. Carr

Eugenia Kalnay

[illegible]

[illegible]

Luther White

ACKNOWLEDGMENTS

The author is grateful for advice and support from the members of my doctoral committee, especially Drs. Fred Carr and Kelvin Droegemeier. I appreciate the support and collegiality among all the members of the ARPS and HubCAPS teams at CAPS. In particular, Dr. Ming Xue was very helpful on many ARPS issues as well as being willing to help with general computing questions. Discussions with Dr. Vince Wong were quite valuable in the process of tuning the ARPS model parameters, particularly the radiation and surface physics. Dr. Jian Zhang is acknowledged for her work in producing and supporting the cloud analysis portion of ADAS, as well as the precipitation scoring programs which were used in this work.

Some data for this work was obtained from systems supported by the School of Meteorology. Radar data and some radar data software utilities came from the National Severe Storms Laboratory. Other data come by way of the Oklahoma Climate Survey and the Joint Office for Science Support, managed by NOAA and NCAR.

This research is supported by the Center for Analysis and Prediction of Storms, which is funded by NSF grant ATM91-20009 and a supplemental grant through the NSF from the FAA. Further support for the author came from a Centennial Research Assistantship from the University of Oklahoma.

Computing support was provided by the Environmental Computing Applications System at the University of Oklahoma, and the San Diego Supercomputer Center.

TABLE OF CONTENTS

LIST OF TABLES

LIST OF ILLUSTRATIONS

ABSTRACT

Advances in numerical modeling, computer speed, and high-resolution observing systems are driving a trend toward high resolution numerical modeling using grid resolutions of 30 km and less. Recently, for example, the Center for Analysis and Prediction of Storms (CAPS) has undertaken real-time forecast efforts at scales of 27, 9 and 3 km. There is a need for data assimilation techniques that can be used at these scales and take maximum advantage of data such as the Oklahoma Mesonet and the operational Doppler radar network. It is also necessary that the assimilation techniques be efficient, so that lead time can be maximized for 0-12 hour forecasts.

Two assimilation methods are presented to address these needs: the ARPS Data Assimilation System (ADAS), and a method of directly correcting phase errors in a forecast, as part of a data assimilation strategy.. ADAS uses a modified Bratseth successive correction scheme to analyze surface and upper air data. Unique terms allow for the proper handling of raw Doppler radial velocity data. Because the Bratseth scheme converges to the solution found by optimal interpolation, the relative accuracy and density of data from the diverse sources is taken into account.

One of the unique attributes of the sensitive operational Doppler radars is that they can observe atmospheric boundaries (such as fronts and thunderstorm outflow boundaries) well. It is common for numerical forecasts to have position errors in such features as well as in thunderstorm cells and convective complexes. It is proposed that the problem of correcting a numerical forecast field can be simplified if such phase errors are directly addressed. An objective method of determining and correcting phase errors in forecasts is described and tested under various scenarios, including simple dynamic models, an observing system simulation experiment (OSSE) involving the

forecasting of ongoing convection, and a real data case involving predictions of the development of severe thunderstorms.

It is shown that the phase correction is effective in producing an analysis field that agrees with the data and preconditions the fields for the application of objective analysis. In the OSSE, the scheme is quite successful in achieving a long-term positive effect on the thunderstorm forecast. In the real-data case, the phase correction had a positive influence on subsequent forecasts for both a front and a complex severe thunderstorm situation. The improvement lasted between 2 and 3 hours for a 3-km forecast, which is at or beyond the expected limit of predictability for thunderstorms.

Chapter 1 Introduction

1.1 Regional and Storm-scale Weather Forecasting

During the past 20 years thunderstorm modeling has advanced as an accepted research tool for studying the dynamics and morphology of thunderstorms. At the same time, new operational mesoscale instrument systems such as the wind profiler demonstration network, state scale mesonets and the WSR-88D radar network (Weather Surveillance Radar-1988 Doppler, Klazura, et al., 1993) are increasing our ability to monitor the atmosphere at the meso-β- (20-200 km) and meso-γ- (2-20 km) scales. Although the WSR-88D radar network was primarily intended to provide precipitation monitoring and allow for short-term (0-30 min.) warning for hazardous weather, including severe thunderstorms and tornadoes, the radial wind and hydrometeor reflectivity data from the radars also represent rich sources of data that can be used to improve forecasts of weather, particularly of those features that impact quantitative precipitation forecasts and forecasts of significant weather.

Improved modeling capability, data availability, and increasing computer processing power lead to the hope of increasing the accuracy of short term (0-12 hour) forecasts of precipitation, thunderstorm initiation and evolution as envisioned early this decade (Lilly, 1990, Droegemeier, 1990). Prediction of thunderstorms which evolve to produce severe weather, aviation hazards or flooding rains is of particular importance. Beyond the effects of individual storms, lines and clusters of storms are often observed to affect the weather at larger scales (e.g., Stensrud and Fritsch, 1993). The mesoscale development of the atmosphere has been shown to be sensitive to the initiation of convection, that is when or where convection begins will change the mesoscale features over the ensuing 24 hours (e.g., Fritsch and Chappel, 1980).

An important area for research is the incorporation of radar and other high-resolution data in analyses used for initializing forecasts of thunderstorms and mesoscale weather (e.g., Droegemeier, 1997). A property of Doppler radar data is that they are incomplete. That is, they only provide the radial component of the wind (the radial velocity) and a measure of the total hydrometeor density (the reflectivity) within each sampled volume of the atmosphere. Techniques must be developed to exploit the information in radar data and, where possible, to deduce the unmeasured wind components and other atmospheric variables. Some schemes devised to use radar data involve retrieval of model fields not observed by radar by making use of time-series of radar data (e.g., Shapiro et al., 1995a). Another approach follows a more traditional objective analysis procedure of applying local corrections to forecast fields based on surrounding observations (Bergthórssen and Döös, 1955 and Bratseth, 1986, among many others) -- data from many sensors, including radar data, can be added as increments to a background forecast. A difficulty in using storm-scale forecast fields as analysis background fields arises from small scale features (such as fronts, thunderstorms or outflow boundaries) that may have been properly developed in the model but mispositioned in some way -- a phase error in the forecast. The initialization must then tear down the misforecasted disturbances and then rebuild them in the proper location, a difficult task when you may have just radar winds as observations on the smallest scale. Instead, one can try to directly address phase errors; in other words, use the radar-observed variables to determine the phase errors, then adjust *all variables* of the background field for the position errors in the background. Such phase-corrected fields can then be used as initial conditions for the model, as pre-conditioned backgrounds for objective analysis techniques and retrievals, or as a starting point in a three- or four-dimensional variational data assimilation scheme.

As an aside, in addition to the correction of a single forecast as part of an analysis, a phase-correction scheme could be adapted to combine ensembles of storm-scale forecasts to produce a consensus forecast. When there are phase differences among the members of a forecast ensemble, a consensus created by averaging the forecasts grid-point-by-grid-point is likely to produce an ensemble average with weak or smeared-out features compared to any one of the ensemble member's forecast. Considering one forecast as the control, the phase differences among the ensemble can first be calculated relative to the control. The phase differences can be averaged to obtain a consensus, and each of the members phase adjusted toward that consensus. Then, the ensemble mean could be calculated by averaging each of the phase-adjusted ensemble members.

1.2 Convective Initiation

The pioneering work of Byers and Braham (1949) confirmed that low-level convergence in a conditionally unstable atmosphere is responsible for the formation of thunderstorms. This convergence is often produced by low-level air mass boundaries. Low-level boundaries can consist of synoptic scale fronts or drylines (e.g., Koch and McCarthy, 1982, Bluestein and Jain, 1985,), sea-breeze or other terrain-induced discontinuities (Pielke and Segal, 1986, Wilson et al., 1992), outflow boundaries (gravity currents) from mesoscale systems including squall lines (e.g., Carbone et al., 1990, Weckworth and Wakimoto, 1992), or outflow boundaries from individual thunderstorms (e.g., Wilson and Mueller, 1993).

Rhea (1966) found that among storms that formed within 370 km (200 n mi.) of a Great Plains dryline, the first storm of the day was within 18.5 km (10 n mi.) of the dryline 78% of the time. Also, recent work using Doppler radars (Wilson and Schreiber, 1986, Wilson et al., 1988) and visible satellite imagery (Purdom, 1982) has shown that many of the convective cells which develop under synoptically quiescent conditions, and were once generally thought to be random in nature, are triggered by the interaction of the outflow boundaries from their predecessors. In the plains of eastern Colorado, under a variety of conditions, 80% of the thunderstorms were found to develop along radar-observed discontinuities (Wilson and Schreiber, 1986).

It should be stressed that not all low-level boundaries produce convection. The vertical velocity associated with low-level convergence along the boundary must be strong enough to overcome any capping inversion; the atmosphere must be at least conditionally unstable to convection; the incipient convective updraft must be able to survive entrainment of upper level air which may be significantly less buoyant, and so on.

In addition to convergence along boundaries such as the dryline and outflow boundaries, there are other mechanisms for inducing low-level convergence sufficient to trigger thunderstorms. Principal among these are mechanical lifting due to upslope over mesoscale terrain features, and pressure perturbations associated with gravity waves (Uccellini, 1975, Uccellini and Koch, 1987). For the former, the outlook for successful prediction of initiation is good as long as the important terrain feature is resolvable, and the mechanism driving the wind, whether it is a larger scale pressure gradient or differential heating of sloped terrain, is well forecast. The gravity wave situation is a bit more complicated. Internal gravity waves whose source could be geostrophic adjustment or jet streaks or shearing instabilities (Uccellini and Koch, 1987, Djuric', 1987) are difficult phenomena to try to predict and would require, at minimum, that their source and ducting layer be accurately predicted. A vexing part of this problem is the relatively fast rate of propagation of the waves and their manifestation as a weak surface pressure perturbation (0.2 - 5 mb, as summarized by Uccellini and Koch, 1987, which often lies within the range of measurement error). It is hoped that gravity waves that are significant and long-lived enough to affect convective initiation will have strong enough signals in the surface pressure observations and might appear in the radar data (as observed for a wintertime 5 mb amplitude wave by Ramamurthy et al., 1993) so as to be detected and their future propagation predicted.

Shallow gravity currents from thunderstorms (generally having a depth of 3 km or less) are discussed here as "air mass boundary" features as they represent cold-air outflow boundaries and are typically detectable by surface observations of temperature and pressure and often by radar. As such they show greater promise for detection and treatment in assimilation schemes, though their shallow depth poses a problem for radar detection at long range.

Another important issue is the precise location along such boundaries that thunderstorms form. For example, along-dryline features that create zones of locally-enhanced convergence have been identified as important for determining the location of thunderstorm initiation (Koch and McCarthy, 1982), and studies of thunderstorm outflow boundaries in Colorado (Wilson, et al., 1992) have identified micro-α scale (200 m - 2 km) features as signatures for impending thunderstorm development. A studies of convection initiated along the Florida sea-breeze front (Wakimoto and Atkins, 1994) revealed that horizontal convective rolls (HCRs) in the planetary boundary layer of wavelength 5 km or less were significant in defining areas of enhanced cumulus development. Also, Weckworth and Wakimoto (1992) found Kelvin-Helmholtz waves above the cold air of a gust front from a mesoscale convective system, which were, in places, perpendicular to the leading edge (perpendicular to the environmental low-level shear). Interaction of these waves, with wavelength of 3-5 km, was seen as significant in the initiation and organization of the subsequent convection. Rao et al. (1999) used high resolution modeling, including the effects of small scale topographical features, in a sea-breeze simulation and found interaction among HCRs with scales of less than 1-km to be important in building larger HCRs that could trigger moist convection.

These sub-meso-γ scale features will likely be difficult to forecast with a numerical model initialized with largely meso-β scale data. Creating such waves in a model may be possible with high enough resolution, but predicting the precise position of the troughs and crests is not promising. The influence of such small scale features may thus be a factor limiting success in predicting convective initiation.

In summary, the prediction of precise locations for thunderstorm initiation is a very difficult problem and in some situations requires that the forecast model generate small scale waves and properly position their generation and accurately forecast their propagation. Since there are generally not enough data in the currently available operational systems to even attempt to initialize the smallest scale triggering mechanisms, it may be necessary in many situations to analyze the initial thunderstorm circulation as soon as possible after initiation of convection and radar detection. If the model is able to generate the proper waves, but not necessarily pinpoint their location, a phase-correction scheme may have great utility for initializing the model at thunderstorm initiation time.

1.3 Radar-Observed Atmospheric Boundaries

The WSR-88D radar provides not only information on precipitating systems but is sensitive enough to detect turbulence-induced refractive index gradients and insects in the atmosphere's boundary layer. Under most conditions, measurements in the optically clear air are limited to a volume enclosed by a circle of radius 60 km from the radar site, extending to the top of the boundary layer (typically 1 to 3 km, Doviak and Zrnic', 1984). Outside that region, clear-air returns are often found in the immediate vicinity of significant atmospheric boundaries (within a few km either side). Figure 1.1 shows a dramatic example of a set of atmospheric boundaries stretching across Central

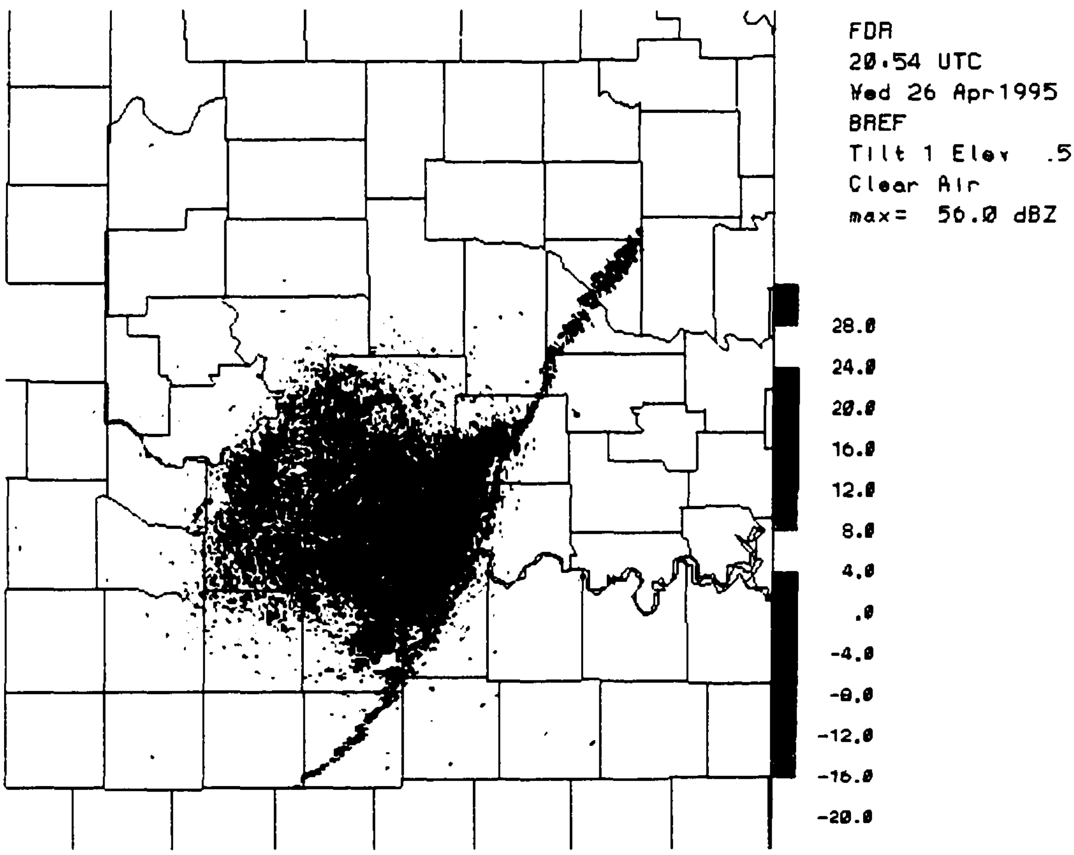

Figure 1.1 Frederick, Oklahoma radar (KFDR), showing non-precipitation radar echoes due to a front stretching from central Oklahoma into northern Texas.

Oklahoma. Due to the value of such boundaries in defining weather changes and their significance in convection initiation, radar returns from atmospheric boundaries are quite valuable to the human forecaster. The challenge is convey this information to a numerical model.

However, atmospheric boundaries, particularly those marking significant wind shifts, are sources of turbulence, and the vertical motion associated with their low-level convergence, cause a local increase in the height of the boundary layer. These two effects help to increase radar reflectivity in the optically clear air above the mean boundary layer depth, and thus are detectable at a greater distance than more quiescent air motions. Also, when such a boundary exists at close range, where the radar volume can resolve motions on a 2-4 km scale, waves transverse to the boundary can sometimes be detected.

It is hypothesized that proper use of Doppler radar information that reveals the location and strength of atmospheric boundaries will lead to more accurate predictions of convection initiation and early storm development. In order to go beyond simple extrapolative techniques this information must be assimilated into a mesoscale model. So one goal of this research is to seek ways of utilizing these radar data describing meso-β to meso-α scale boundaries, to improve numerical weather prediction for phenomena on the scale of tens to hundreds of kilometers (with grid spacing of 2 to 10 km).

1.4 Analyses for Regional Modeling

There are a number of efforts to produce analyses and forecasts in real-time at regional scales, that is with grid scales of 3-30 km and domain size ranging from about 600 x 600 km to 3000 x 3000 km. Many of these efforts are summarized by Mass and Kuo (1998), and amended by Snook (1998). A typical system run at a university or regional center away from the National Centers for Environmental Prediction (NCEP) is configured to accept larger-scale data from a model run by a national forecasting center, typically NCEP's Eta or Rapid Update Cycle (RUC) model. These data are remapped to the regional model's high resolution vertical and horizontal grids. Most of these forecasts are produced using the larger scale model's initial condition or short term forecast, without benefit of additional local or mesoscale data. Any improvements, then, of the forecasts from their coarser scale parents, are presumably due to the increased resolution of the terrain and to any improved model parameterizations or surface physics that might be tuned for a local area.

It is desirable to take advantage of the increasing number of networks of local-scale observations such as the Oklahoma mesonet, the Forecast Systems Lab (FSL) Mesonet in Colorado. Thus the forecasts produced by FSL as part of the Local Analysis and Prediction System (LAPS, Albers et al., 1996) and those done at the Center for Analysis and Prediction of Storms (CAPS) which make of use of an analysis system known as the ARPS (Advanced Regional Prediction System, Droegemeier, 1997) Data Assimilation System (ADAS) make use of such data. NCEP itself has been running a 10-km version of the Eta model which uses a variational analysis scheme developed by Parrish (Parrish et al., 1996, Rogers et al., 1998) that can include mesoscale data, including those from the operational Doppler radar network (WSR-88D, or NEXRAD) via the NEXRAD Information Dissemination Service (NIDS) radar data files. Also, regional forecasts for research have been done using assimilation methods (commonly known as nudging) and National Center for Atmospheric Research (NCAR) and Pennsylvania State University (Penn State) regional forecast model, the MM5 model (e.g., Stauffer et al., 1991 and Stauffer and Seaman, 1994).

The analysis component of the LAPS system (Albers, 1994, Albers, 1995) is largely based on the Barnes analysis method (Barnes, 1963), with some modification to account for variable data densities. It is formulated to produce analyses at the earth's surface and at 50-hPa pressure levels in the vertical. In 1994, the LAPS scheme was first adapted to run in a region outside of Colorado in order to initialize the ARPS model over Oklahoma. This set of programs, known as Oklahoma-LAPS, or OLAPS (Brewster, 1996) was used in the real-time modeling done at CAPS in 1994 and 1995 (Droegemeier, 1996, and Xue et al, 1996). However, it was found that the interpolation required to convert the OLAPS grids (on pressure coordinate surfaces) to the ARPS coordinate (a vertically stretched height, terrain-following coordinate) risked the loss of important details such as the magnitude of a capping inversion. Interpolating back-and-forth between these coordinates is an impediment to accurate and efficient use of data from more than a single time in continuous data assimilation mode.

To overcome those limitations, the ADAS program was developed at CAPS by this author. It is based on the Bratseth analysis scheme (Bratseth, 1986) which is a successive corrections method that converges to the optimal interpolation solution (Gandin, 1963). In other words, it is able to properly account for variability in station spacing, variability in accuracy among different observing systems and the error in the background field (typically a larger scale forecast or a forecast from the ARPS model, itself). Furthermore ADAS is formulated on the ARPS model coordinate surfaces, thus eliminating inaccuracies and inefficiencies due to interpolation between vertical coordinate surfaces. It is a unique application of the Bratseth method to storm-scale weather analyses, including the analysis of Doppler radar data. Unlike LAPS it is capable of combining radial velocities from more than one radar, and properly accounts for the error in the measurements when combining radial velocities with other data. Some of the LAPS empirical treatments of remotely sensed data for creating analyses of cloud variables (cloud and rainwater) were adapted for the ARPS vertical coordinate, refined and modified to include specification of latent heating profiles in regions of precipitation by other CAPS scientists (Zhang et al., 1998) and are included as part of the ADAS system. ADAS is fully described in Chapter 3 and is used as part of the real-time experiments presented in Chapters 7 and 8.

1.5 Other Storm-Scale Data Assimilation Techniques

There exist other methods of assimilating radar and other high resolution data into a numerical model. Principal among these are three-dimensional variational (3D-VAR) methods, wind and thermodynamic retrieval approaches and the adjoint methods.

In the 3D-VAR method, the fit to the data and the background field are expressed as a functional to be minimized and constraints are applied to ensure the solution will be relatively smooth and balanced for the forward model forecast (e.g., Parrish, 1996). It bears some similarity to optimal interpolation, with some additional advantages. Some advantages to the 3D-VAR methods are that the model prognostic variables can be transformed to the observed variables, even if the observations are integrals of the model variables along some remotely sensed path. A potential pitfall involves the specification of the balance among the variables. On large scales the balance can be specified as near geostrophic. More complex balance relationships can be expressed for ageostrophic flows, but many of the more interesting features such as thunderstorm outflow boundaries and non-hydrostatic thunderstorm circulations can have complex states that might not fit the balance constraints. Nevertheless, for large portions of a typical mesoscale domain, such balance relationships are useful and valid, so this 3D-VAR scheme is part of the Eta operational forecast model data assimilation cycle at NCEP.

The wind and thermodynamic retrieval methods are founded on the idea that given a time series of radar data observations, the equations of motion for the atmosphere and some conservation relations for radar reflectivity, one can solve for the 3D wind fields, and then, given a time series of 3D winds one can solve for the buoyancy, and finally, the pressure perturbations -- the "many-for-the-price-of-one" proposition first put forward by Gal Chen (1978) and Hane and Scott (1978). Over time, variants of the schemes have come forward and been subjected to testing and intercomparison (e.g., Shapiro et al., 1995b and Lazarus et al., 1999). In fact, the Shapiro "two-scalar" technique has been successfully used to forecast a severe supercell thunderstorm

(Weygandt et al., 1998) using the ARPS model. A problem with the retrieval method is that a solution can be found in the region of the high resolution data (generally within the thunderstorm), but where there are no high resolution data, enclosed "holes" in the gridded fields must be filled and the solution along the edge of the storm blended into the larger scale forecast field (Ellis, 1997). For this reason, ADAS includes the retrieval data as an input data type and has been used for this blending task (unpublished tests).

Another drawback to the retrieval methods is that the taking of derivatives in time and space, generally using centered finite differences in the radar coordinate space, results in a diminished solution region compared to the size of the original radar-observed volume. Five complete radar volumes are needed in order to get the time derivatives needed for the complete solution. While the radar is observing only the clear air returns and during the initial growth phase of a storm, there may be large and important regions where a solution is not possible.

The adjoint technique can be described as a method of fitting models to observations. The numerical model solution is variationally fit to data collected over time by minimizing a functional which sums the difference between the evolving solution and the data, and one or more smoothness constraints. The functional is a feature shared with 3D-VAR, such that this method can be termed "4D-VAR" with time being the additional dimension. Constraints on the smoothness of the solution (in time and space) can also be added. The adjoint is thus a mathematically sophisticated way to obtain an initial condition that will agree with the data and be dynamically consistent with the numerical model being used.

The variational techniques are iterative in application, as the minimizing model state must be found among many degrees of freedom compared to the number of observations. In the case of the adjoint, the time dimension requires that model forecasts are employed in finding the solution. A forward model is run and the differences from the observations are collected in the cost function. Then the adjoint of the numerical model is used in a "backward forecast" to obtain the derivatives needed to find the minimum of the cost function, and the process is repeated until convergence is found. The need to make many runs of the model makes the technique computationally expensive. Nevertheless, successful solutions of the adjoint have been found for observed thunderstorms (e.g., Sun et al., 1991 and Sun, 1994) and for high resolution observations of the atmospheric boundary layer near thunderstorm outflows (Sun and Crook, 1994).

Some computational savings can be achieved if one solves for time-averaged fields during the assimilation period. This idea and the use of a simplified set of equations for just the radar-observed quantities form the foundation of the technique known as the "simple adjoint" (Qiu and Xu, 1992). Its most common application is for solving for the time-averaged wind using Doppler radial velocity data. Successful results were obtained using very high resolution data over small domains (5 x 5 km) using Phoenix II field project data in (Xu et al., 1994a and Xu et al., 1994b), and in an 8 x 12 km airport domain using Terminal Doppler Weather Radar data (Xu et al., 1995). This method shows promise for the future operational use, but the testing to date has largely been done using small domains and high-time resolution radar data (1-minute radar scans), unlike the operational needs for large domains with multiple radars and 5-10 minutes between volume scans.

It is worth noting that Sun (1994) found that accurate specification of the background thermodynamic fields improved the convergence of the adjoint technique and that Xu et al. (1995) found that providing the result of the previous high-resolution wind field (a "persistence" first guess) to the simple-adjoint improved its rate of convergence. Both demonstrate that improving the first guess can be very beneficial to these advanced assimilation techniques. Although the adjoint techniques are not used here, the phase-correction technique could be applied to background fields provided to such techniques as a way of improving their efficiency and perhaps their accuracy.

1.6 Research on Correcting Phase Errors

The concept of directly addressing location errors has seen some consideration in the literature. Thiebaux et al. (1990) noted that forecast position errors of major features were negatively affecting quality control decisions in the NCEP operational models. They showed improvement in quality control decisions when the background fields were adjusted for possible position errors before computing observation-forecast residuals that are used in those decisions. Mariano (1990) has developed an oceanic analysis technique based on the considering position errors in the gulf stream current and its ring vortices. Mariano's technique is called "contour analysis"; it involves contouring two or more fields, considering the optimal location of each contour, then inverting to obtain gridded data. It is intended for melding of location information from different sources (e.g. a forecast and satellite map of gulf stream meanders) and requires a complete specification of the field from the two sources.

The idea of phase-correcting assimilation for storm scale models was presented and tested in some simple one-dimensional models in previous work by this author (Brewster, 1991). It was found that knowledge of phase errors determined from one variable in the dynamic system could effectively be used to update the system, correct errors in all the fields and improve the forward forecast of the system state. This work, and its extension to two-dimensional testing is described in more detail as part of Chapter 5 of this document. The technique was then successfully applied to a three-dimensional thunderstorm simulation (Brewster, 1998), and details of those experiments are presented in Chapter 6.

Hoffman et al. (1995) developed a method for expressing the error in a forecast in terms of a "distortion error" consisting of a displacement of each analyzed field (compared to the forecast) and an amplification of the anomaly. Correlation maximization and RMS reduction were explored as a means for finding the displacement error similar to Brewster (1991). It was also shown how this could produce new analyses from forecast fields using data to provide the correction. The method was demonstrated using single fields of data such as SSM/I precipitable water (or integrated water vapor, IWV), ERS-1 backscatter wind data, and a 500-hPa geopotential height field. No forecast experiments were performed.

Hoffman and Grassotti (1996) extended the work of Hoffman et al. (1995) by performing distortion analyses on the precipitable water fields of European Center for Medium Range Weather Forecasting (ECMWF) analyses (on a 2.5° X 2.5° archived grid) made without benefit of those data. They used the position and amplitude corrected fields to make new forecasts. The work focused on fronts and marine tropical cyclones in the otherwise observation-sparse South Pacific ocean, using those large-scale grids. They minimized a functional formed by

$$J = J_r + J_d + J_a \qquad (1.1)$$

where J_r is a specific measure of the fit of the distorted field to the data, J_d is a measure of the smoothness of the displacement vectors, and J_a is a measure of the magnitude of the displacement vectors. The functional is minimized after transforming the data to spectral space. The spectral transform and the smoothness constraints are designed to focus the displacements on the large-scale displacement errors. Hoffman and Grassoti showed that the distortion analysis improved the ECMWF analyses by decreasing the differences between the analyses and satellite IWV observations; further, subjective improvements in the shape and scale of frontal features were noted.

Alexander et al. (1998) used a technique termed "digital warping" to transform water vapor fields using SSM/I IWV observations and the Pennsylvania State University-National Center for Atmospheric Research MM5 mesoscale model. The scheme is based on warping or "morphing" done in movies to transform images from one character or shape to another. It takes N pairs of "tie points" which connect areas of similar features between the observation and background field. The meteorological fields are then transformed from the original to a warped field by applying a third order transformation of the grid locations and minimizing the difference in the third order translation with respect to the translations dictated by the "tie points". The authors used 130 manually-entered tie points to described the warping of IWV fields in a mid-Atlantic frontal system, a North Atlantic cyclone, and the 13 March 1993 "superstorm" cyclone in the Southeast United States. The transformation was applied to all of the model's moisture fields, and the resultant fields were then used as part of the initial conditions in the MM5 model. Forecasts made from these initial conditions were compared to control runs made without benefit of the warping, and to forecasts made using nudging.

Forecasts made with the warping were judged to be superior than the other forecasts, and improvements were noted in fields such as the surface pressure even though the transformation was only applied to moisture variables. Clearly feedback through improved rainfall and diabatic heating was influencing the surface pressure and thus the wind forecasts.

Strum et al. (1999), in work ongoing at this writing, are developing a general user interface (GUI) to manually identify phase corrections to apply to the Navy's Coupled Ocean/Atmosphere Mesoscale Prediction System (COAMPS). Early results show that short term improvements can be made to forecasts by applying a uniform-in-height phase correction to a model run with grid spacing of 24-km and with a convective parameterization scheme. In their case, other model errors had eliminated the phase correction advantage by about 6 hours after the phase correction.

Fiedler (1999) manually identifies spurious convective storms in the ARPS model and targets them for removal in a technique labeled "storm surgery". The technique seeks to modify the wind fields as well as the moisture and hydrometeor variables in the model. In order to remove the three-dimensional circulation associated with the storm, the model's horizontal wind fields are first broken down into divergence and vorticity components. A cylinder of a manually-determined radius is prescribed in order to fit the targeted storm, and the vertical velocity and associated divergence/convergence couplet is removed from the model's vertical velocity and divergence fields, respectively. Then the horizontal wind components are reconstructed solving a Helmholz equation from the now-corrected divergence and vorticity components of the wind. Fiedler also demonstrates that this method can be used to insert cells in the model, by replacing the storm circulation in the model fields in locations where the model had failed to trigger convection.

1.7 Statement of Hypothesis

It is my hypothesis that radar and small-scale surface data can be assimilated in a non-hydrostatic model using a successive-correction Bratseth-type analysis, gradually introducing the analysis increments into the model, and using the radar data as part of a scheme to correct any phase errors in the background forecast field. This scheme has advantages of being computationally inexpensive, so it can be done on desktop workstations in real-time. Also, it is an "all-weather" approach in that a solution can be found in every situation, even in the case of limited data such as during the receipt of "clear-air" echoes, and at the time of storm initiation. Furthermore, the fields generated in this method can also be used to improve background fields employed in other methods, thus serving to reduce the number of iterations needed to reach a solution, improving the accuracy of the final solution, and possibly increasing the likelihood that the minimization methods will reach the proper local minimum in the event there are multiple minima (Li, 1994). Herein I assert, and seek to demonstrate, that phase correction will be improve a successive corrections analysis scheme, by improving the accuracy of the background field.

The use of raw radar data and radar retrievals in a Bratseth analysis scheme, and its general application at this small scale, are original contributions to the science. The ADAS analysis software has been developed to be fully flexible for many different sources of input data and has been used in groundbreaking weather forecasting experiments at CAPS (e.g., Droegemeier, 1997). Furthermore, it is a package that has gained acceptance outside of CAPS, and is finding use in real-time and research applications at other institutions.

Phase correction, applied to data assimilation, is a unique innovation. Phase correcting techniques have been used with other data, but some of the testing presented herein preceded other published work.

In this dissertation I will first complete the introductory material by introducing the ARPS model. Then, the ADAS and phase correcting analysis schemes will be fully described. Tests of the phase correction at one- and two-dimensions using simple models will be presented. Therein it will be shown how the phase correction using a single variable can improve the forecasting of all variables. Those tests will be followed by an observation system simulation experiment (OSSE) using a thunderstorm simulation with the full ARPS model. Finally, demonstrations of the combination of ADAS and phase correction scheme using real data will be made with a frontal analysis and a forecast of a severe thunderstorm outbreak.

Chapter 2
ADVANCED REGIONAL PREDICTION SYSTEM, ARPS

2.1 Model Description

The model used for the 3-dimensional numerical modeling in this study is the Advanced Regional Prediction System (ARPS), developed at the Center for Analysis and Prediction of Storms (CAPS). It is a non-hydrostatic forecast model with a terrain-following height (σ_z) coordinate system. The basic features and equations, including information about the ARPS accessory programs mentioned in this chapter, are documented in the ARPS User's Guide (Xue et al., 1995).

The forecast experiments for this work employed the ARPS 1.5 order turbulent kinetic energy based closure equations (Wong et al., 1994, Xue et al., 1995), the boundary layer mixing formulation of Sun and Chang (1986), a two-path multi-spectral radiation scheme with cloud, aerosol and water vapor absorption and scattering (Chou and Suarez, 1994), and the Tao ice microphysical parameterization (Tao and Simpson, 1993). The ARPS two-layer soil model and surface flux parameterization (Xue et al., 1995, Wong et al., 1998) based on the soil model of Noilhan and Planton (1989) was used. No parameterization of cumulus convection was used.

Several options, including the grid spacing, vertical stretching, time step and initial conditions varied among the tests made, and those options will be described with each set of experiments and are tabulated in Appendix A and Appendix B, while some of the information common among the real-data tests is described below.

2.2 Initialization of Land Surface Features

Terrain for the real-data cases was produced using the terrain analysis program in the ARPS package. Raw data were obtained from a 5-minute resolution terrain database at the National Center for Atmospheric Research (NCAR). The raw data were interpolated to the 12-km ARPS grid using a 3-pass Barnes scheme.

The land surface features used in the real-data cases were computed using an ARPS algorithm that interpolates soil and monthly mean vegetation data. The four most prominent soil types in each model grid square were identified from the raw data. The types and their relative fraction are stored in a static file and the flux characteristics of each are used in the model's surface heat and moisture surface flux calculations. Soil-type data came from the United States Department of Agriculture's State Soil Geographic Data Base CD-ROM (STATSGO, USDA, 1994). The STATSGO soil data were produced from soil survey maps and enhanced, where necessary, with LANDSAT satellite data. It has a resolution of approximately 2 km. Vegetation fraction and land-use data came from the Environmental Protection Agency (EPA) and NOAA National Geophysical Data Center's global ecosystems database CD-ROM (Kineman, 1992). The data were produced from NOAA-11 AVHRR satellite-based observations converted to monthly averages with approximately 1-km resolution.

The surface and deep soil moisture were initialized using daily precipitation data for four months prior to each case and a simple soil moisture budget based on the antecedent precipitation index (Mewes, 1998).

Terrain and surface features for the 3-km runs were interpolated from the 12-km data. This was done to ensure consistency between the boundary and the forecast fields for the 3-km runs. Running the 3-km model run with higher resolution surface and terrain data was considered, but even with the 12-km interpolated data, some small scale noise was being generated in the model which seemed to be associated with the soil surface data, so higher resolution data were not introduced for these runs.

2.3 Background and Boundary Conditions

Since the ARPS model is run on a regional domain, it requires an external model (or ARPS itself run over a larger domain) to specify time-varying conditions on the lateral boundaries. An external model solution is used on the upper boundary of the ARPS model as part of the damping of high frequency waves in the stratosphere, and an external model is also used to provide background conditions for the analyses from which the model forecast cycle is begun. For this work, the external model used was NCEP's Rapid Update Cycle (RUC, Bleck and Benjamin, 1993), as received in real-time at CAPS. The RUC model is a version of FSL's Mesoscale Analysis and Prediction System (MAPS, Benjamin et al., 1994); it has a hybrid isentropic-σ_p coordinate. The RUC used for this work has a horizontal resolution of 60-km and is run over a domain covering the contiguous United States. The RUC is run continuously with a 3-hour intermittent data assimilation mode. Data from US rawinsondes, surface airways observations, aircraft, and wind profilers comprise most of the data used in the RUC model. The RUC forecast data were interpolated to the ARPS model grid using second order interpolation. Prior to receipt at CAPS the model had been interpolated from the RUC's hybrid coordinate to 25 hPa pressure surfaces.

Chapter 3 ARPS DATA ASSIMILATION SYSTEM, ADAS

3.1 Analysis Program

The analysis program of the ARPS Data Assimilation System, ADAS, interpolates observations onto the ARPS grid, combining the observed information with a background field. The background field can be provided by climatology, a single sounding, a larger scale forecast, or a forecast at the same scale with an earlier initial time. This chapter describes the analysis and assimilation techniques in ADAS. Some details about the options used in this work vary with the forecast experiments and are described further in the results chapter.

While many operational centers have used a Statistical (or Optimal) Interpolation scheme (OI) for data analysis, Bratseth (1986) has shown that an iterative scheme (also known as a successive correction scheme) of the proper design can converge to OI. An iterative scheme can offer computational savings over OI in that large matrix solutions need not be found. Also, some iterations can be done using broad-scale data, followed by iterations using higher resolution data to analyze smaller scale features. Finally, iterations can be interspersed with model time-steps to form a dynamic initialization (Newtonian relaxation or nudging) process (Lorenc et al., 1991).

As in the OI scheme, the Bratseth interpolation method accounts for the relative error between the background and the error in each observation source, and accounts for the relative positions and density of the observations, so is less sensitive to large variations in data density than the Barnes schemes (Carr et al., 1996). The Bratseth method has been used successfully in research (e.g., Sashegyi et al., 1993 and Ioannidou and Pedder, 1999) and in operational mesoscale modeling (e.g., Lorenc et al., 1991). Operational use of ADAS itself was previously reported in Brewster (1996).

3.2 Theoretical Formulation

ADAS uses a successive correction scheme, known as the Bratseth method, which is described in this section, (largely following Shashegyi et al., 1993). The variable, s, is analyzed at grid points x using observations $s^o{}_j$. For iteration n:

$$s_x(n) = s_x(n-1) + \sum_{j=1}^{nobs} \alpha_{xj}\left[s_j^o - s_j(n-1)\right] \tag{3.1}$$

where the same equation has been applied at the observation locations, j, to arrive at the analysis at those points for the previous iteration, s_j:

$$s_j(n) = s_j(n-1) + \sum_{k=1}^{nobs} \alpha_{jk}\left[s_k^o - s_k(n-1)\right] \tag{3.2}$$

where

$$\alpha_{xj} = \frac{\rho_{xj}}{m_j} \quad \text{and} \quad \alpha_{jk} = \frac{\left(\rho_{jk} + \hat{\sigma}^2\delta_{jk}\right)}{m_k} \tag{3.3}$$

are the weights applied to each observation. In Eq. 3.3, $\hat{\sigma}^2$ is the ratio of observation error variance to background error variance which are interpolated from tables provided for each data source and background type. δ_{jk} is the Kronecker delta; it is zero unless $j=k$, when it is unity. The spatial correlation, ρ, is modeled as Gaussian:

$$\rho_{jk} = \exp\left(\frac{-\left|\vec{r}_{jk}\right|^2}{R^2} \right) \exp\left(\frac{-\left|\Delta z_{jk}\right|^2}{R_z^2} \right) \qquad (3.4)$$

where $\vec{r}_{jk}$ is the horizontal separation of each data-to-grid-point pair for Eq. 3.1 and each data pair for Eq. 3.2, while Δz is the vertical separation. The weights have been normalized by the density of observations around each observation location:

$$m_k = \sigma_n^2 + \sum_{l=1}^{nobs} \rho_{kl} \qquad (3.5)$$

Note that on the initial pass, $n=1$, the analysis at the observation locations, $s^o{}_j(0)$, is given by a tri-linear interpolation of the background field.

An option is provided to analyze data more in the fashion of an isentropic analysis. This option models the vertical correlation as a function of difference in potential temperature rather than height:

$$\rho_{ij} = \exp\left(\frac{-\left|r_{ij}\right|^2}{R^2} \right) \exp\left(\frac{-\left|\Delta\theta_{ij}\right|^2}{R_\theta^2} \right) \qquad (3.6)$$

The height-based vertical correlation function was used in this work.

In order to speed convergence toward observations and to bring in data of different scales, the horizontal correlation distance factor, R, can be reduced from the initial pass to the final pass.

$$R(n) = \kappa_v \kappa_n R_o \tag{3.7}$$

where κ_v represents the variation of the scaling distance in the correlation model among the variables, allowing for shorter correlation distance for variables such as moisture which tend to have smaller horizontal structure. In this work, κ_v=0.9 for moisture, and 0.9 for the wind components, and is 1.0 otherwise. κ_n is a scaling parameter for each pass, and $\kappa_n R_0$ is the scale length which allows a telescoping of scales as one uses more dense data and accounts for the smaller scale errors in the model with successive iterations.

It should be noted that the use of a telescoping correlation scale parameter (κ_n not constant) makes this application an unusual application of the Bratseth technique and since the correlation scale changes with each pass, the convergence to a particular OI solution is no longer a feature of the technique. However, the technique does trend toward each OI solution for as many passes as κ_n remains fixed, and within that time retain the properties of OI in terms of accounting for varying data density and the relative error between observation and background and among different observation types. In this way the method can account for the different scales of error that might appear in the model, rather than being fixed on some average scale of forecast error.

3.3 Application in ADAS

The background field for ADAS can come from any of the ARPS initialization methods; for example, from a single sounding, a larger-scale model forecast or a previous ARPS model forecast. When data from a larger scale model are used, a preprocessing program uses quadratic interpolation to remap the model data from the

$$\rho_{jk} = \exp\left({-\left|\bar{r}_{jk}\right|^2} \middle/ {R^2} \right) \exp\left({-\left|\Delta z_{jk}\right|^2} \middle/ {R_z{}^2} \right) \tag{3.4}$$

where $\bar{r}_{jk}$ is the horizontal separation of each data-to-grid-point pair for Eq. 3.1 and each data pair for Eq. 3.2, while Δz is the vertical separation. The weights have been normalized by the density of observations around each observation location:

$$m_k = \sigma_n^2 + \sum_{l=1}^{nobs} \rho_{kl} \tag{3.5}$$

Note that on the initial pass, $n=1$, the analysis at the observation locations, $s^o{}_j(0)$, is given by a tri-linear interpolation of the background field.

An option is provided to analyze data more in the fashion of an isentropic analysis. This option models the vertical correlation as a function of difference in potential temperature rather than height:

$$\rho_{ij} = \exp\left({-\left|r_{ij}\right|^2} \middle/ {R^2} \right) \exp\left({-\left|\Delta\theta_{ij}\right|^2} \middle/ {R_\theta{}^2} \right) \tag{3.6}$$

The height-based vertical correlation function was used in this work.

In order to speed convergence toward observations and to bring in data of different scales, the horizontal correlation distance factor, R, can be reduced from the initial pass to the final pass.

$$R(n) = \kappa_v \kappa_n R_o \qquad (3.7)$$

where κ_v represents the variation of the scaling distance in the correlation model among the variables, allowing for shorter correlation distance for variables such as moisture which tend to have smaller horizontal structure. In this work, κ_v=0.9 for moisture, and 0.9 for the wind components, and is 1.0 otherwise. κ_n is a scaling parameter for each pass, and $\kappa_n R_0$ is the scale length which allows a telescoping of scales as one uses more dense data and accounts for the smaller scale errors in the model with successive iterations.

It should be noted that the use of a telescoping correlation scale parameter (κ_n not constant) makes this application an unusual application of the Bratseth technique and since the correlation scale changes with each pass, the convergence to a particular OI solution is no longer a feature of the technique. However, the technique does trend toward each OI solution for as many passes as κ_n remains fixed, and within that time retain the properties of OI in terms of accounting for varying data density and the relative error between observation and background and among different observation types. In this way the method can account for the different scales of error that might appear in the model, rather than being fixed on some average scale of forecast error.

3.3 Application in ADAS

The background field for ADAS can come from any of the ARPS initialization methods; for example, from a single sounding, a larger-scale model forecast or a previous ARPS model forecast. When data from a larger scale model are used, a preprocessing program uses quadratic interpolation to remap the model data from the model grid to the ARPS forecast grid. For this work, the background comes from either the RUC operational numerical model from NCEP (Benjamin et al., 1994) or from an ARPS forecast with an earlier initial time.

In ADAS, five variables are analyzed on the ARPS σ_z coordinate grid: u and v grid-relative wind components, pressure, potential temperature and specific humidity. Other variables could be added with straight-forward modification to the code.

The vertical velocity, w, is diagnosed from the horizontal winds using the continuity equation and a constraint of a zero wind velocity in the direction normal to the model terrain, at the bottom and at either the top of the model domain or a user-specified height for the upper boundary condition. Generally the user-specified height would be approximately the height of the tropopause and would be consistent with the bottom of the layer that will be treated with Rayleigh damping to inhibit vertical velocity in the stratosphere

Any inconsistency between these constraints and the analyzed horizontal velocity field is resolved by distributing the apparent error in the horizontal divergence with height, and the w field is adjusted after that error is removed. After w has been found for each column, the horizontal wind fields may be adjusted to satisfy the condition that the total mass divergence is zero everywhere. In certain cases, this may help to ensure a smooth start for the ARPS model. For the ADAS analyses reported here the tropopause height was estimated to be 13 km, the horizontal divergence error is distributed linearly in height, and the horizontal wind adjustment was not employed.

Observed data are classified into four types: 1) single-level observations, typically surface observations; 2) multiple-level observations or upper-air observations (such as rawinsondes and wind profilers); 3) raw Doppler radar observations; and 4) radar-retrieved data. Radar retrieved data are observations obtained from algorithms which use a time-sequence of Doppler radar data to deduce all three Cartesian wind components, temperature and pressure. Each observation type has its own data arrays, but aside from the raw Doppler radar winds, they are all analyzed in the same way. Routines for reading sounding, wind profiler and surface observations in LAPS format (as archived for the 1994 and 1995 VORTEX field project) have been implemented. Other sounding and surface data sources can be added.

Raw radar data (Doppler winds and reflectivity) are first averaged into data columns, in a separate program. In this step all radar data within each grid volume are averaged and then output in a compact form for later processing. If there is a very small percentage of a grid volume covered by valid radar data, or if there is a high standard deviation among the data in the volume, the average for that grid volume is set to missing. The primary purpose of the step is to average the data to the resolution of the model grid being used, reducing the volume of data used. Storing the data as columns is done for convenience in programming the location searching as all data in a column share the same x,y location in space. Programs are available to process NIDS and WSR-88D Archive Level-II radar data tapes. For this work, the Archive Level-II data were used.

Tables 3.1 and 3.2 show the value of the correlation range in the horizontal and vertical dimensions, and the data use switches set for the real-data experiments presented in this work. In the tables, "U/A" refers to upper-air data, namely radiosondes and wind profiler data, "Sfc" refers to surface observations. The values were chosen in order to first converge toward a solution supported by the rawinsonde observations, then to take in surface data and iterate using correlation distances telescoping toward a solution that can be supported by the surface data, including mesonet data which are available for the cases studied.

Table 3.1 Parameter values for ADAS with 12-km dx

Pass	R	R_z	Use U/A	Use Sfc
1	400 km	300 m	yes	no
2	300	300	yes	no
3	200	200	yes	yes
4	80	200	no	yes
5	60	200	no	yes
6	50	100	no	yes

Table 3.2 Parameter values for ADAS with 3-km dx

Pass	R	R_z	Use U/A	Use Sfc	Use Radar
1	200 km	300 m	yes	yes	no
2	80	200	no	yes	no
3	40	200	no	yes	no
4	40	100	no	yes	no
5	10	100	no	no	yes
6	10	100	no	no	yes

Upper-air observation error and model background errors are specified as a function of height. and are read from tables, one per input data source. Tables 3.3, 3.4 and 3.5 list the RUC model background errors, the error of observations assigned to the NWS radiosonde data and the error of the surface aviation observations used in these runs. Note that the error in humidity is reported as a percentage, relative humidity, this is converted to an error in specific humiditry, q_v, using the background temperature and pressure; this accounts for a dependency on humidity, and hence humidity error, with season. The RUC background errors were estimated from information supplied by FSL (via the World Wide Web) about the RUC 0-12 hour forecast error. Because the scale of the analyses done for this work is much smaller than that of the RUC model, the RUC errors reported in the tables are enhanced from the reported errors, especially near the surface, to empirically account for the lack of representation of these smaller scales in the RUC model. This serves to give somewhat higher weight to the surface observations, making a closer fit to the observations. This was tuned via operational test runs.

Table 3.3 Background Error Table for ADAS

AGL	press	Temp	RH	winds	
0. m	3.0 hPa	3.0 C	30. %	5.0 ms^{-1}	5.0 ms^{-1}
100.	3.0	3.0	30.	5.0	5.0
500.	2.5	3.0	20.	5.0	5.0
1000.	2.5	3.0	20.	5.0	5.0
1500.	2.5	3.0	20.	5.0	5.0
2000.	2.0	2.5	20.	5.0	5.0
3000.	2.0	2.0	20.	5.0	5.0
4000.	2.0	2.0	20.	5.0	5.0
5000.	2.0	2.5	20.	5.0	5.0
5500.	2.0	2.5	20.	5.0	5.0
7000.	2.0	2.5	20.	6.0	6.0
8000.	2.0	2.5	20.	6.0	6.0
9000.	2.0	2.5	20.	7.0	7.0
10000.	2.0	2.5	20.	7.0	7.0
12000.	2.0	2.5	20.	7.0	7.0
16000.	2.0	3.0	20.	8.0	8.0
20000.	2.0	3.0	20.	8.0	8.0

Table 3.4 Observation Errors Assigned to U.S. NWS Radiosonde Data

AGL	press	temp	RH	winds	
0. m	0.6 hPa	1.2 C	5. %	2.0 ms^{-1}	2.0 ms^{-1}
111.	0.6	1.2	5.	2.0	2.0
540.	0.6	1.2	5.	2.0	2.0
988.	0.6	1.2	5.	2.0	2.0
1457.	0.6	1.0	5.	2.0	2.0
1949.	0.6	1.0	5.	2.0	2.0
2466.	0.6	1.0	5.	2.0	2.0
3012.	0.6	1.0	5.	2.0	2.0
3591.	0.6	1.0	5.	2.5	2.5
4206.	0.6	1.0	5.	2.5	2.5
4865.	0.6	1.0	7.	2.5	2.5
5574.	0.6	1.0	7.	2.5	2.5
6343.	0.6	1.0	7.	3.0	3.0
7185.	0.6	1.0	10.	3.0	3.0
8177.	0.6	1.0	10.	3.5	3.5
9163.	0.6	1.0	12.	3.5	3.5
10362.	0.5	1.5	15.	3.5	3.5
11774.	0.5	1.8	15.	3.5	3.5
13507.	0.5	1.8	15.	3.5	3.5
15795.	0.4	2.0	15.	3.0	3.0

Table 3.5 Observation Errors Assigned to Surface Aviation Obs

pres	temp	RH	u	v
1.22 hPa	0.60 C	5. %	1.0 ms^{-1}	1.0 ms^{-1}

3.4 Treatment of Doppler Radar Data

A unique aspect of this application of the Bratseth scheme is the use of Doppler radial velocities to correct the horizontal winds. The Doppler radial velocities are converted to increments of u and v wind components by subtracting the observed radial wind, v_r, from the dot product of the analysis wind and the observing angle (radar azimuth, ϕ). The imputed correction is assigned a direction parallel to the azimuth, *i.e.*

$$u' = \cos\phi\left[v_r - (\cos\phi u + \sin\phi v)\right] \qquad (3.8)$$

$$v' = \sin\phi\left[v_r - (\cos\phi u + \sin\phi v)\right] \qquad (3.9)$$

The covariance between two Doppler radial winds requires special treatment in that the correlation between two radial wind observations is affected by the azimuth angle separation between the data. As described by Cole (1994),

$$\mathrm{cov}(s_i, s_j) = \cos(\phi_i - \phi_j)\left[\sigma^2(s_i)\sigma^2(s_j)\right]\rho(\vec{X}_i, \vec{X}_j) \qquad (3.10)$$

where s_i and s_j are two separate observations and ρ is a correlation based on the relative locations ($\vec{X}_i$ and $\vec{X}_j$) of the two observations.

So, for example, if radial velocities at a given point are available from two radars observing perpendicular to each other, the covariance model correctly indicates the observations are not correlated.

Similarly for mixed data types, the covariance is reduced from that of two complete wind observations:

$$\left(u_i',u_j'\right)=\cos\left(\phi_i-\pi/2\right)\left[\sigma^2(s_i)\sigma^2(s_j)\right]\rho\left(\vec{X}_i,\vec{X}_j\right) \qquad (3.11)$$

and

$$\left(v_i',v_j'\right)=\cos\left(\phi_i\right)\left[\sigma^2(s_i)\sigma^2(s_j)\right]\rho\left(\vec{X}_i,\vec{X}_j\right) \qquad (3.12)$$

where u_i' and v_i' are increments from a radial wind observation and u_j' and v_j' are from a complete wind observation (e.g., an anemometer or a rawinsonde).

More complex means of dealing with Doppler radar data include dual-Doppler wind algorithms and Doppler retrieval schemes. The Doppler retrieval schemes employ a time-sequence of radar-observed winds and reflectivity to diagnose the total wind field as well as temperature and pressure information. Wind data generated in any of those manners would be ingested by ADAS through the radar-retrieval-data arrays and aren't subject to the special correlation calculations presented in Eqs. 3.10-3.12. Retrieved wind data were not used in experiments presented here.

3.5 Cloud Analysis

A module is included in ADAS which constructs a complete cloud analysis using surface observations of cloud cover and height, radar and satellite data (Zhang et al., 1998 and Zhang, 1999). The procedure and code were adapted from the cloud analysis of the Local Analysis and Prediction System (LAPS, Albers et al., 1996) developed at the NOAA Forecast Systems Lab. The ADAS version allows the user to select which of the variables from the cloud analysis will contribute to the final output file, and one can control the thresholds applied to radar data. The cloud analysis uses its identification of the cloud type (stratus, stratocumulus or cumulus based on depth and thermodynamic profile) to estimate in-cloud vertical velocities. Tests using the ARPS model have shown that vertical velocities determined in this way generally do not last long in the model as the model forcing overwhelms the initial state. Since these initial velocities can trigger condensation in regions of conditionally unstable air masses, there is a risk that the initial vertical velocity can trigger convection that is sometimes spurious due to incorrect cloud type determination. For that reason, the cloud vertical velocity was not used here.

Separately, ADAS has an optional algorithm to initialize microphysical variables using only radar data. This system uses the reflectivity and background temperature and humidity, to assign mixing ratios of the water species. Temperature is adjusted to provide buoyancy to counteract the weight of the rain. This scheme is not used in this work, and is more fully documented by Brewster (1998b).

3.6 Automated Data Quality Control

ADAS includes a few quality-control steps. The surface data are first analyzed to the observation locations to compare with each other, and data are rejected if the pre-analysis of neighboring observations differs significantly from the observation. The quality control threshold is set as a multiple of (generally 4 times) the combined expected observation and background error, based on the following formula,

$$\Delta o_{thr} = \mu_{thr}\sqrt{\left(\sigma_{bkgd}^2 + \sigma_{obs}^2\right)} \tag{3.13}$$

where Δo_{thr} is maximum allowable magnitude of difference of observation from the analysis of other stations, μ_{thr} is a threshold-setting multiplier (commonly 3.0-4.0) based on subjective confidence in each data source, σ^2_{bkgd} is the expected error variance of the background field, and σ^2_{obs}. is the expected error variance of the observations. Other data are quality-controlled by comparing the observations to the background field interpolated to the observation site. Thresholds of allowed differences from the background are set fairly high (by means of the data error tables provided, e.g., Table 3.3, and Eq. 3.13) to allow for instrument error and errors in representativeness. Representativeness error is especially important in the case of radar data being compared to large-scale gridded forecasts. Statistics are reported in the standard output showing the number and percentage of data points rejected in this manner.

Also part of the quality control system is a means to manually exclude data at specified surface stations. This is useful for manual editing and for real-time use when there may be stations that regularly have unrepresentative observations due to siting problems or instrument faults. A file is read containing a list of stations and variable numbers which are excluded from the analysis (they are flagged as rejected by the quality control). At this time the blacklist procedure is implemented only for surface data.

3.7 Incremental Analysis Updating

The ADAS incremental analysis updating scheme is designed to gradually apply the ADAS-determined increments over time during the execution of the ARPS model. As discussed in Chapter 1 and following the work of Bloom et al. (1996), gradually applying the increments over time may reduce shocks to the model caused by any unbalanced analysis increments and may allow the unobserved variables to adjust to the changes due to the increments from the observed variables. Modifications have been made to both the ADAS software and the ARPS model to add incremental analysis updating. The procedure is to stop the model at a time near the observation time and ADAS is run to calculate increments using the model prediction as a background. The increments (difference between the final ADAS analysis and the model state at that time) are written to a file; the model is then restarted, and the increments are applied fractionally over time at a user-specified time-step interval. The fraction of the total increment applied at each time is calculated so that the updates sum to the analysis increment calculated by ADAS. Options exist to allow the user to control the time period over which the increments are applied and which variables are affected.

The software allows the increments to either be divided equally over the update period or applied using a triangular function so that the increments start near zero, increase to a maximum in the middle of the nudging window and then decrease to zero by the end of the nudging period; this is depicted in Fig. 3.1. Consistent with the work of Bloom et al. (1996), and lacking extensive testing of the triangular time-weighting, the time weighting was constant in the work presented here. Because the spatial and time filtering in the model can act to damp increments applied from one time step to the next in the leap-frog scheme the user is provided the option of applying a small gain to the increments. For this work the constant-in-time weighting was employed and a 1.1 gain was applied to the increments to account for the time-filtering. The gain was determined subjectively by comparing the result of the forecast-update process to the observations and the result of the analysis alone at the initial time (not shown).

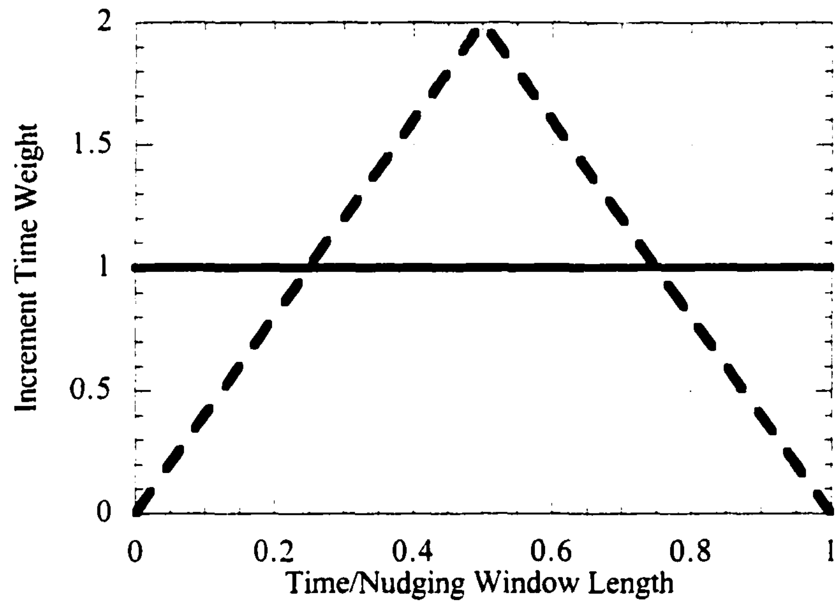

Fig 3.1 Time weighting factor applied to the analysis increments in the ADAS nudging scheme. Solid is option 1, fixed increments, and dashed, option 2, triangular time weighting.

Chapter 4 Phase Correcting Technique

4.1 Introduction

As described in the first chapter, it is proposed that data assimilation may be improved by using high resolution data, such as radar data, to address the position or phase errors in the model forecast background field before applying other corrections or retrievals. In this way the atmospheric structures generated by the forecast model can be preserved by applying translation corrections to other variables. Then, without relying on any inductive or retrieval processes necessary for time-dependent schemes, an incomplete measure of the wind field, such as the Doppler radial velocity, can have an impact on the other model variables.

I have developed a phase correction method which can be applied to a non-hydrostatic grid point model (Brewster, 1991, Brewster, 1998a). Complete details of the method are presented in this chapter, including the process of finding the three dimensional field of horizontal phase correction vectors, and three ways to apply the corrections to the forecast fields.

4.2 Estimation of Phase Error

The phase correction method seeks a local translation, described by a field of translation vectors, $\delta\bar{x}$, to apply to the forecast field in order to distort it to match the observed data. There are several methods one might use to find the best shift vector; two studied here are (1) minimize the mean square difference from the observations, or (2) maximize a correlation between the shifted fields and the observations.

To minimize the squared differences from the observations, a functional based on squared errors is formed:

$$J[\delta\bar{x}] = s\left(|\delta\bar{x}|l^{-1}\right)\sum_{j=1}^{n\,\mathrm{var}}\alpha_j\sum_{i=1}^{nobs}\frac{\left\{T\left[\bar{F}(\bar{x}_i+\delta\bar{x})\right]-o_j(\bar{x}_i)\right\}^2}{\sigma_{i,j}^2} \tag{4.1}$$

where o is the observation, $\bar{x}_i$ is the observation location, $\delta\bar{x}$ is the horizontal displacement vector, $\sigma_{i,j}^2$ is the expected observation variance, which, in general, is a function of variable, data source and height, $\bar{F}$ is the forecast field smoothed by a 9-point filter in two dimensions; the smoothing is done to avoid fitting small-scale noise to the observations . T represents a transformation, if necessary, from the forecast variables to the observed quantity. For example, the transformation could be a projection to a radial velocity, the conversion of liquid water to reflectivity, or an integration of moisture to obtain precipitable water. Each variable is weighted according to α, which may account for the total number of observations of each type or the anticipated usefulness of a particular variable in determining the displacement error.

The leading term on the right hand side, s, is a distance-dependent function that serves as a penalty for straying too far from the original position. The function used here is from Thiebaux et al. (1990):

$$s\left(|\delta\bar{x}|l^{-1}\right) = \frac{\exp\left(|\delta\bar{x}|l^{-1}\right)}{\left(1+|\delta\bar{x}|l^{-1}\right)} \tag{4.2}$$

where l is a length scale parameter. For the 1-D tests, l is fixed at 8 grid lengths; in other parts of this work, this l is set as:

$$l = 0.5\sqrt{L_{x\,vol}^2 + L_{y\,vol}^2}$$

where L_{xvol} and L_{yvol} are the lengths of the test volumes (discussed below) in the x and y directions, respectively.

To maximize the correlation, ρ, a correlation equation is written:

$$\hat{\rho}[\delta\bar{x}] = \sum_{j=1}^{n\,\mathrm{var}} \alpha_j \rho\left[\bar{f}_j(\bar{x} + \delta\bar{x}), o_j\right] \tag{4.3}$$

where the variables have the same meaning as in Equation 4.1.

The algorithm to find the solution for either method proceeds by dividing the domain into small overlapping test volumes. The size of the volumes is flexible, and is determined by considering the data density, the scale of displacement error one is seeking to correct, and the size of any discrete precipitation systems resolvable by the model. One needs to have sufficient data in most volumes to make a valid calculation of the RMS or correlation without being dominated by any single observation. Yet it is desirable if one can consider volumes that are as small as the size of individual thunderstorm cells. For these reasons, an iterative approach using a cascade of test volumes sizes is used. First, the large-scale phase errors are found using large scale data and large grid volume sizes, then the displacements are refined to correct small-scale errors using smaller test volume sizes and high resolution data. In the context of correcting a thunderstorm forecast, one can think of the process as correcting the position of a squall-line first, then adjusting the relative location of individual cells. A volume size of 8-12 horizontal grid lengths and 5-7 vertical grid lengths is the minimum size used here for the final iteration.

For each of the grid volumes tested, the algorithm gathers the data that lie within the volume. It then seeks the displacement in location of the grid that will minimize the RMS or maximize the correlation between the observations and the distorted grid. The

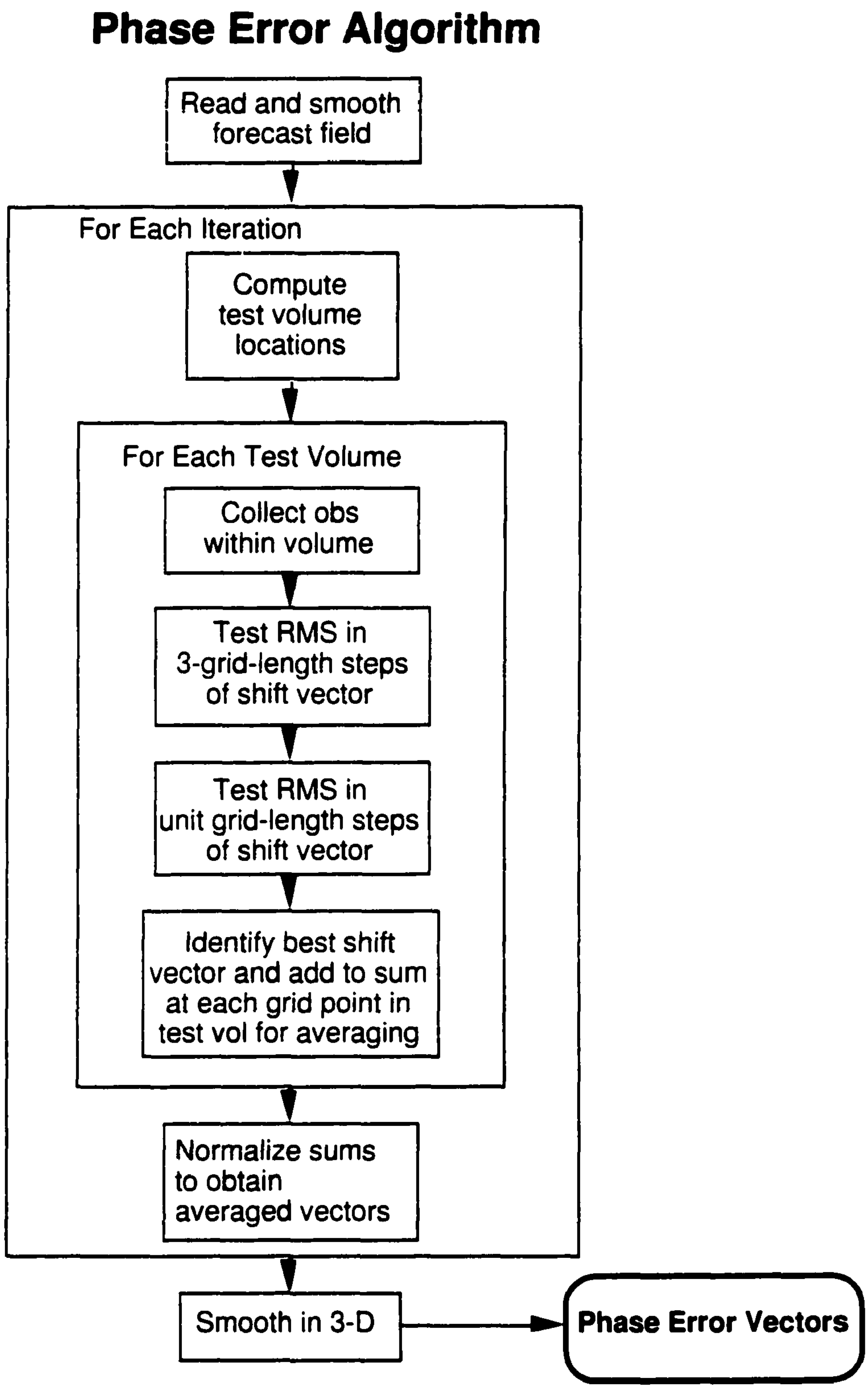

Figure 4.1 Flow chart for determining phase error field.

algorithm considers horizontal displacements of the forecast grid in intervals of three grid lengths in both x and y directions and for each of the sub-volumes. Searching is refined to unit grid length shifts within a square of width 5 grid lengths centered on zero offset and in any other area where the value of the test function has not exceeded twice the minimum value found within 5 grid lengths of zero offset. In the regions where two or more sub-volumes overlap, the components of the shift vectors found in each of the overlapping volumes are averaged. Where there are no data in an individual volume, $\delta\bar{x}$ is set to zero for that particular volume.

Table 4.1 shows the dimensions and data usage for the phase correction applied to the real-time data in this work. Volume dimensions are given in grid-lengths, and the grid length of this work is 3-km. In the table, "overlap" is the overlap of one test volume with its neighbor. "N_x" refers to the number of volumes in each of the x and y directions, and N_z the number of volumes counting in vertical (a total of $N_x \times N_x \times N_z$ volumes in the iteration). "U/A" refers to upper-air data, namely profiler and radiosonde data, and "sfc", surface data. All observed variables are used except pressure, which would be complicated by the slope of the model surfaces (when the shift is applied the shift is applied to the perturbation pressure to avoid affecting the mean vertical pressure distribution due to the slope of the model surfaces). Radar data used here consists of radar radial wind and reflectivity remapped to the 3-km resolution grid by averaging all data within each grid cell. The model hydrometeors are converted to reflectivity, Z, based on the following formula (Kessler, 1969 and Rogers and Yau, 1989):

$$Z = 1.73 \times 10^4 \left(10^3 \bar{\rho} q_r\right)^{7/4} + 3.8 \times 10^4 \left[10^3 \bar{\rho}\left(q_s + q_h\right)\right]^{2.2} \qquad (4.4)$$

where q_r , q_s, and q_r are the forecast rainwater, snow, and hail concentrations, respectively, and in this equation $\bar{\rho}$ refers to the model's horizontal mean atmospheric air density. The model Z is converted dBZ, the variable reported by the radar, making use of

$$dBZ = 10\log_{10}(Z).$$

The model Cartesian winds are projected on the radar view angle when compared to the radar wind data.

Table 4.1
Test volume dimensions and data use for phase error detection.

Pass	i,j vol width	i,j over lap	N_x vol	k vol hgt	k over lap	N_x vol	Use U/A	Use Sfc	Use Radar
1	61	31	3	10	2	3	yes	yes	no
2	35	18	6	10	2	6	yes	yes	no
3	16	5	15	12	2	15	no	yes	yes
4	10	5	25	12	2	25	no	yes	yes

This search method, which is somewhat "brute-force", is chosen over a more elegant minimization scheme with the anticipation that the presence of individual thunderstorm cells in the radar data and model grid would not, in general, yield a smoothly varying field of either the correlation or the RMS cost function, and may have multiple local minima and maxima. Sample square error topologies are presented in Fig. 4.2 for the real data experiment described in Chapter 8. In the figure each plotted number represents the square error statistic divided by 10 for each offset in i,j space. Topologies for two sample volumes are displayed; each contains some radar data, but the topologies are quite different. For volume "A", the field is well behaved with a well defined trough containing a single local minimum (at i,j offset=5,4). For another

A

i offset

	-15			-12			-9			-6			-3			0			3			6			9			12			15
15	.	.	.	.	.	10	10	10	9	9	9	9	9	8	8	8	8	8	8	8	8	8	8	8	8	8	8	8	8	8	8
14	.	.	.	.	.	10	10	10	9	9	9	9	9	8	8	8	8	8	8	7	7	7	7	7	7	8	8	8	8	8	8
13	.	.	.	.	.	10	10	10	9	9	9	9	9	8	8	8	8	8	8	7	7	7	7	7	7	7	7	7	8	8	8
12	.	.	.	.	.	10	10	10	9	9	9	9	9	8	8	8	8	8	8	7	7	7	7	7	7	7	7	7	7	8	8
11	.	.	.	.	.	10	10	10	9	9	9	9	9	8	8	8	8	8	8	7	7	7	7	7	7	7	7	7	7	7	8
10	.	.	.	.	.	10	10	10	9	9	9	9	9	8	8	8	8	8	7	7	7	7	7	7	7	7	7	7	7	7	8
9	.	.	.	.	.	10	10	9	9	9	9	9	9	8	8	8	8	8	7	7	7	7	7	7	7	7	7	7	7	7	7
8	.	.	.	.	.	10	10	9	9	9	9	9	9	8	8	8	8	7	7	7	7	7	7	7	7	7	7	7	7	7	7
7	.	.	.	.	.	10	10	9	9	9	9	9	8	8	8	8	8	7	7	7	7	7	7	7	7	7	7	7	7	7	7
6	.	.	.	.	.	10	10	9	9	9	8	8	8	8	8	8	7	7	7	7	7	7	7	7	7	7	7	7	7	7	7
5	.	.	.	.	.	10	10	9	9	8	8	8	8	8	8	7	7	7	7	6	6	6	6	7	7	7	7	7	7	7	7
4	.	.	.	.	.	10	10	9	9	8	8	8	8	8	7	7	7	7	6	6	6	6	6	7	7	7	7	7	7	7	7
3	.	.	.	.	.	10	9	9	8	8	8	8	8	7	7	7	7	7	6	6	6	6	7	7	7	7	7	7	7	7	8
2	.	.	.	.	.	9	9	9	8	8	8	8	8	7	7	7	7	7	7	7	7	7	7	7	7	7	7	8	8	8	8
1	.	.	.	.	.	9	9	9	8	8	8	8	8	7	7	7	7	7	7	7	7	7	7	8	8	8	8	8	8	8	8
0	.	.	.	.	.	9	9	9	8	8	8	8	8	8	7	7	7	7	7	8	8	8	8	8	8	8	8	8	8	8	8
-1	.	.	.	.	.	9	9	9	8	8	8	8	8	8	8	8	8	8	8	8	8	8	8	8	8	8	8	8	8	8	8
-2	.	.	.	.	.	10	9	9	9	8	8	8	8	8	8	8	8	8	9	9	9	9	9	9	9	9	8	8	8	8	8
-3	.	.	.	.	.	10	10	9	9	9	9	9	9	9	9	9	9	9	9	9	9	9	9	9	9	9	9	9	8	8	8
-4	.	.	.	.	.	10	10	9	9	9	9	9	9	9	9	9	9	9	9	9	9	9	9	9	9	9	9	9	9	9	9
-5	.	.	.	.	.	10	10	10	9	9	9	9	9	9	9	9	9	9	9	10	9	9	9	9	9	9	9	9	9	9	9
-6	.	.	.	.	.	10	10	10	9	10	10	10	10	10	10	10	10	10	10	10	10	10	10	10	9	9	9	9	9	9	9
-7	.	.	.	.	.	11	11	10	10	10	10	10	10	10	10	10	10	10	10	10	10	10	10	10	10	10	9	9	9	9	9
-8	.	.	.	.	.	11	11	11	10	10	10	10	10	10	10	10	10	10	10	10	10	10	10	10	10	10	10	10	9	9	9
-9	.	.	.	.	.	11	11	11	11	11	11	11	11	11	11	11	11	11	11	11	10	10	10	10	10	10	10	10	10	10	9
-10	.	.	.	.	.	12	12	11	11	11	11	11	11	11	11	11	11	11	11	11	11	11	11	10	10	10	10	10	10	10	10
-11	.	.	.	.	.	12	12	12	11	11	11	11	11	11	11	11	11	11	11	11	11	11	11	11	11	10	10	10	10	10	10
-12	.	.	.	.	.	13	13	12	12	12	12	12	12	12	12	12	12	12	12	11	11	11	11	11	11	11	11	10	10	10	10
-13	.	.	.	.	.	13	13	13	12	12	12	12	12	12	12	12	12	12	12	12	12	11	11	11	11	11	11	11	11	10	10
-14	.	.	.	.	.	.	.	.	13	13	13	13	13	13	13	12	12	12	12	12	12	12	12	11	11	11	11	11	11	11	11
-15	.	.	.	.	.	.	14	.	13	13	13	13	13	13	13	13	13	13	12	12	12	12	12	12	12	11	11	11	11	11	11

B

i offset

	-15			-12			-9			-6			-3			0			3			6			9			12			15
15	20	19	19	18	18	17	17	16	16	16	16	17	17	17	17	16	16	15	15	15	15	15	14	13	14	16	18	19	19	20	20
14	20	19	18	18	17	17	16	16	16	16	16	16	16	16	16	16	15	15	15	15	15	15	16	17	18	19	19	19	19	19	19
13	19	19	18	17	17	16	16	16	16	16	16	16	16	16	16	15	15	15	14	15	15	15	16	17	17	18	18	18	19	19	19
12	19	18	18	17	17	16	16	15	15	15	15	15	16	16	15	15	15	14	14	14	14	15	15	16	17	17	18	18	18	18	19
11	19	18	18	17	16	16	15	15	15	15	15	15	15	15	15	15	14	14	14	14	14	14	15	16	16	17	17	18	18	18	18
10	19	18	17	17	16	15	15	15	14	14	14	15	15	15	15	14	14	14	14	14	14	14	15	15	16	16	17	17	17	18	18
9	18	18	17	16	16	15	15	14	14	14	14	14	14	14	14	14	14	14	13	14	14	14	14	15	15	16	16	17	17	17	18
8	18	17	17	16	15	15	14	14	14	14	14	14	14	14	14	14	13	13	13	13	14	14	14	15	15	15	16	16	17	17	17
7	18	17	16	16	15	14	14	14	14	14	14	14	14	14	13	13	13	13	13	13	13	14	14	14	15	15	15	16	17	17	17
6	18	17	16	15	15	14	14	14	14	14	14	14	13	13	13	13	13	13	13	13	13	14	14	14	14	15	15	16	16	17	17
5	18	17	16	15	15	14	14	14	14	13	13	13	13	13	13	13	13	13	13	13	13	13	14	14	14	14	15	15	16	17	17
4	17	17	16	15	14	14	14	14	13	13	13	13	13	13	13	13	12	13	13	13	13	13	14	14	14	14	15	15	16	16	17
3	17	16	16	15	14	14	14	13	13	13	13	13	13	13	12	12	12	12	12	13	13	13	14	14	14	14	15	15	16	16	17
2	17	16	16	15	14	14	14	13	13	13	13	13	13	12	12	12	12	12	12	12	13	13	14	14	14	14	15	15	16	16	17
1	17	16	15	15	14	14	13	13	13	13	13	13	13	12	12	12	12	12	12	13	13	14	14	14	14	15	15	15	16	16	17
0	17	16	15	15	14	14	13	13	13	13	13	13	13	12	12	12	12	12	12	13	13	14	14	14	15	15	15	15	16	16	17
-1	17	16	15	15	14	14	14	13	13	13	13	13	13	12	12	12	12	12	12	13	13	13	14	14	15	15	15	15	16	16	17
-2	17	16	15	15	14	14	14	13	13	13	13	13	13	13	12	12	12	12	12	13	13	13	14	15	15	15	15	15	16	16	17
-3	17	16	15	14	14	14	14	13	13	13	13	13	13	13	13	12	12	12	12	13	13	14	14	15	15	15	15	16	16	16	17
-4	17	16	15	14	14	14	14	14	13	13	12	12	12	13	13	12	12	12	12	12	13	14	15	15	15	15	15	16	16	17	17
-5	17	16	15	15	16	15	14	14	13	10	9	10	11	12	12	13	12	12	12	13	13	14	15	15	15	15	16	16	16	17	17
-6	17	16	14	16	18	18	15	13	10	8	10	13	13	13	12	13	13	13	13	13	13	14	15	15	15	15	16	16	16	17	18
-7	17	16	14	16	17	16	14	12	9	10	18	22	20	15	13	13	13	13	13	13	14	14	15	15	15	16	16	16	17	17	18
-8	18	16	14	14	14	14	13	11	9	10	15	17	16	14	13	13	13	13	13	13	14	14	15	15	15	16	16	17	17	18	18
-9	18	17	15	14	13	14	14	13	10	8	8	9	10	12	13	14	14	14	13	14	14	15	15	15	15	16	16	17	17	18	18
-10	19	17	17	16	14	15	18	16	14	12	11	9	9	11	13	14	14	14	14	14	14	15	15	15	16	16	17	17	18	18	19
-11	19	18	17	16	15	17	19	17	15	14	10	9	15	18	17	15	14	14	14	14	15	15	15	16	16	17	17	18	18	19	19
-12	19	19	18	17	15	15	16	15	14	12	9	10	17	20	18	16	15	15	15	15	15	15	15	16	16	17	18	18	19	19	20
-13	20	19	18	17	16	15	15	15	15	12	9	8	10	12	14	15	16	15	15	15	15	16	16	16	17	17	18	19	19	20	20
-14	20	20	19	18	17	17	16	16	16	15	13	12	13	14	16	16	16	16	16	16	16	16	16	16	17	18	18	19	20	20	20
-15	21	20	20	19	18	18	18	17	16	16	16	16	17	17	17	17	17	17	16	16	16	16	17	17	17	18	19	19	20	20	21

Figure 4.2 Sample square error topology for RMS-based shift correction search. June 8, 1995 2010 UTC, including radar data. Plotted is the sum of square errors divided by 10 for each i,j offset. Offsets marked with a decimal point were not tested by the algorithm due to lack of positive results in that direction. A and B are two separate shift data volumes.

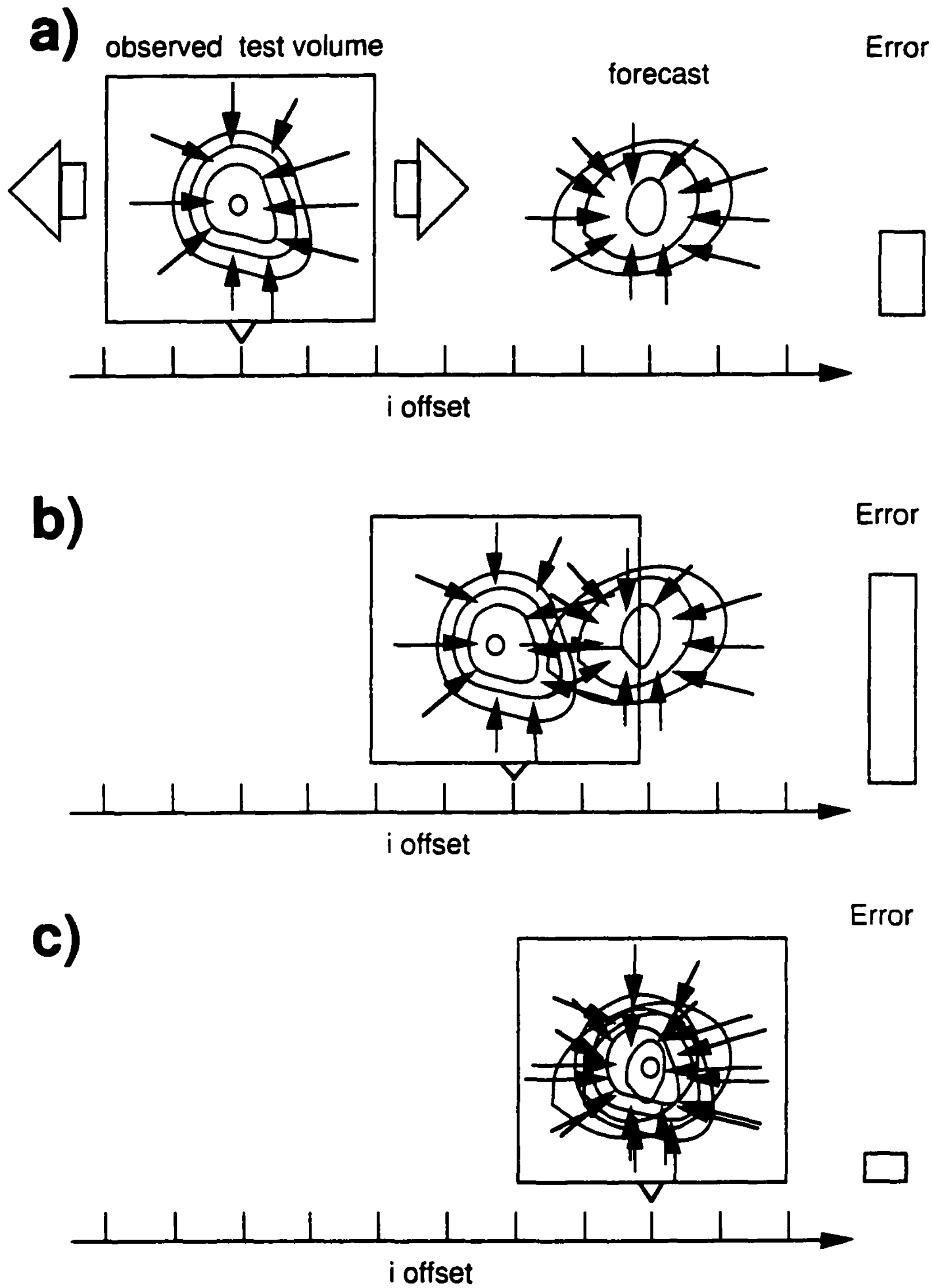

Figure 4.3 Schematic of the change in the error statistic for matching an observed and forecast thunderstorm.

volume, volume "B", the topology is more chaotic. There are a number of small values in a region also displaying a number of large values as "noisier" thunderstorm data finds its match. The minimum is found at i,j offset of -5,-9.

The cause of the irregular pattern is shown schematically in Fig. 4.3. The square error field is relatively flat and largely governed by the distance penalty where the data in the sample volume are being compared to regions of the forecast without thunderstorms (situation "a", Fig 4.3),. As the offset testing approaches a thunderstorm in the forecast grid (situation "b") there are places where the forecast thunderstorm perturbation winds may oppose those observed creating high scores, while a nearby position may be found where the reflectivities and winds line-up and produce the sought-after minimum (situation "c").

Despite the crudeness of the search scheme, the searching is computationally very efficient, and the program, with four iterations and using radar data, runs in much less time than the analysis program on the machines used for this work. It takes about 3 minutes on a desktop workstation.

The result of this process is a three-dimensional field of horizontal shift vectors. These are mapped to the model grid from the test volumes and smoothed to provide a smooth transition across the entire domain. Six passes of a 27-point 3-dimensional filter are used to ensure smoothness.

4.3 Applying the Phase Correction

Once a smoothly varying field of $\delta\bar{x}$ has been determined, it is necessary to correct the forecast model for this error. Three different phase correction schemes have been devised to accomplish this: a single-step shift, a phase correction assimilation (a multiple-step shift), and application of a phase-correcting pseudo-wind in the horizontal advection calculation.

The transformation can be applied to one or more of the variables; by applying the transformation to multiple variables, the structures and local balances among variables generated or maintained by the model are nearly preserved. In the work presented here the translation is applied directly to all the atmospheric variables, with the exception of pressure. For the idealized thunderstorm simulations presented, the pressure was not adjusted. For the real-data cases, the translation is applied to the pressure perturbation. Since the model coordinate surfaces are generally not horizontal, moving the total pressure can cause hydrostatic imbalances. Although the model can quickly adjust to such imbalances, they would be a source of noise in the model forward forecast.

In the single-step adjustment method, the field of shift vectors is used to distort the fields in one step, before execution of the forward forecast. Due to the averaging done in the overlap regions and the smoothing done in the last step, the final field of shift vectors will not be of unit grid lengths. The shift therefore involves an interpolation process to find the values of variables at locations not on model grid points. In the work presented here, a second-order interpolation scheme is employed for this task.

To further ease the transition, the phase correction can be applied in multiple small steps in a manner similar to nudging; we term this phase correction assimilation. The total shift vector is divided into N equal parts where N is the number of shift intervals during the "nudging" period. For the thunderstorm cases presented here, the nudging is done over a fairly short time frame -- 10 minutes, with the nudging done every minute, for a total of 10 equal steps. In general the nudging time window should be no more than the life cycle of the individual features being shifted, so for larger-scale applications, the window could be as long as an hour or two.

Finally, the translation can be achieved by adding an artificial wind to the advection terms in the model equations. The "pseudo-wind" then continuously advects the structures into their proper position during the assimilation time window. In the ARPS model the advection of a scalar is written (Xue et al., 1995):

$$\frac{\partial}{\partial t}(\rho * Q')_{hadv} = \overline{u * \delta_\xi Q'}^{\xi} + \overline{v * \delta_\eta Q'}^{\eta}$$

where

$$\rho^* = |J_3|\overline{\rho}, \qquad u^* = \rho * u, \qquad \text{and } v^* = \rho * v$$

δ_ξ is a finite difference operator in the east-west direction and δ_η is the finite difference operator in the north-south direction, $\overline{\rho}$ is the horizontally averaged air density and J_3 is the Jacobian representing the stretching of the vertical coordinate in the vertical direction. In the application of the pseudo wind scheme, the u and v wind components are replaced by

$$\hat{u} = u + \frac{\delta x}{\delta T_n}, \qquad \text{and } \hat{v} = v + \frac{\delta y}{\delta T_n}$$

where δx and δy are the x and y displacement components, respectively, and δT_n is the time period of the pseudo-wind application. In general, a time-window is sought that will be large enough that the pseudo-wind does not dominate the physical wind in the advection process.

Employing this technique in a model with an explicit finite-difference representation of advection carries the risk of violating the Courant-Friedrichs-Levy (CFL) condition, that is, the stability limitation on the time-step size must now include the effect of the pseudo-wind which could increase the maximum wind in the advection. Limitations could be applied to the maximum pseudo-wind or automatic expansion of the nudging time window. In the experiments performed for this work, no such adjustments were required, as the time-step limit for the model was largely determined by the small grid spacing in the vertical combined with vertical mixing processes which are not affected by the addition of the pseudo-wind.

Phase-Correction and Analysis Correction Cycle

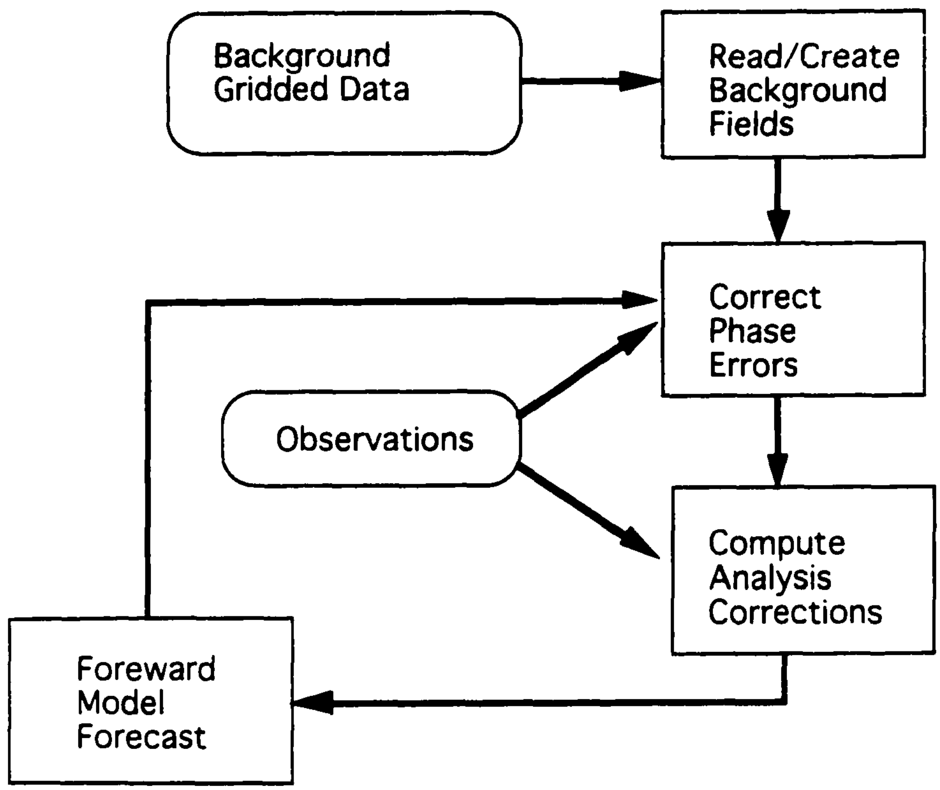

Figure 4.4 Forecast update cycle combining phase correction and analysis steps.

Although the addition of the pseudo-wind in the advection step can be viewed as adding momentum to the system, because this energy is not available to be converted to other forms (as it does not appear in the momentum, pressure, or mixing equations) and is removed after the assimilation window, it should not affect the energy balance of the system.

It is anticipated that the phase shifting technique could serve as a preconditioning of a background field before the application of other analysis schemes, and because changes in amplitude are not applied in this scheme, other methods will be necessary to complete the update. Figure 4.2 is a flow chart showing how the phase correction is applied in concert with the analysis system used in the ARPS forecast model (see Chapter 3), which is similar to the experiments in the Chapters 5 and 8 where phase corrections are combined with analyses or analysis increment updating.

Chapter 5 Tests in One- and Two-Dimensions

In this chapter, the phase correction technique is tested in numerical modeling experiments in one- and two-dimensions. Using simple systems, a number of experiments are conducted to test the ability of the scheme to properly identify and correct the phase errors in the observed variable, and to positively impact the forecast of the observed and unobserved variables. Sensitivity to data error is also examined.

5.1 Experiments in One Dimension

To test phase correction assimilation on a simple system, the one-dimensional shallow water equations are employed. The system is initialized in such a way to produce a hydraulic jump which serves as a proxy for a front in the atmosphere. Tests are performed to see if the phase correction is feasible, if data from a single variable can affect the model forecasts for other variables, and if the phase correction scheme is robust when presented with imprecise data. These 1-D tests are described in this section. Some of these results are also presented in Brewster (1991).

The one dimensional shallow-water equations over a flat surface with constant Coriolis parameter, f, are

$$\frac{\partial u}{\partial t} = -u\frac{\partial u}{\partial x} - \frac{\partial \phi}{\partial x} + fv$$

$$\frac{\partial v}{\partial t} = -u\frac{\partial v}{\partial x} - fu$$

$$\frac{\partial \phi}{\partial t} = -u\frac{\partial \phi}{\partial x} - \phi\frac{\partial u}{\partial x}$$

where $\phi = gh$, h is the depth of the fluid, u and v are the x and y components of fluid motions, and g is gravity. All variables are independent of y.

The equations are modeled by the following finite difference scheme (from Parrett and Cullen, 1984). In terms of "momentum" variables, $m = \phi u$, and $n = \phi v$, where $\phi = gh$, and h is the depth of the fluid, they are:

$$m_i^{n+1} = m_i^{n-1} - 2\Delta t\left\{\begin{bmatrix}\left(u_{i+1}^n + u_i^n\right)\left(m_{i+1}^n + m_i^n\right) \\ -\left(u_i^n + u_{i-1}^n\right)\left(m_i^n + m_{i-1}^n\right) \\ +\left(\phi_{i+1}^n\right)^2 - \left(\phi_{i-1}^n\right)^2\end{bmatrix} / 4\Delta x - fn_i^n - K\left(m_{i+1}^{n-1} - 2m_i^{n-1} + m_{i-1}^{n-1}\right) / \Delta x^2\right\}$$

(5.1)

$$n_i^{n+1} = n_i^{n-1} - 2\Delta t\left\{\begin{bmatrix}\left(u_{i+1}^n + u_i^n\right)\left(n_{i+1}^n + n_i^n\right) \\ -\left(u_i^n + u_{i-1}^n\right)\left(n_i^n + n_{i-1}^n\right) \\ +\left(\phi_{i+1}^n\right)^2 - \left(\phi_{i-1}^n\right)^2\end{bmatrix} / 4\Delta x + fm_i^n - K\left(n_{i+1}^{n-1} - 2n_i^{n-1} + n_{i-1}^{n-1}\right) / \Delta x^2\right\}$$

(5.2)

$$\phi_i^{n+1} = \phi_i^{n-1} - 2\Delta t\left[\left(m_{i+1}^n - m_{i-1}^n\right) / 2\Delta x - K\left(\phi_{i+1}^{n-1} - 2\phi_i^{n-1} + \phi_{i-1}^{n-1}\right) / \Delta x^2\right] \qquad (5.3)$$

The domain is of length $2\pi L$, where L is 200 km and is represented by 128 points. Cyclic boundary conditions are used. The initial conditions are specified by:

$$u(x,0) = U\cos(x / L)$$

$$v(x,0) = 0$$

$$\phi(x,0) = \phi_m + U\left[\frac{U}{8}\cos\left(\frac{2x}{L}\right) + \left(\phi_m - \frac{U^2}{8}\right)^{1/2}\cos\left(\frac{x}{L}\right)\right]$$

where $\phi_m = gh_m$, h_m is the mean height of the fluid, and U is a constant mean velocity. The initial conditions are plotted in Fig. 5.1

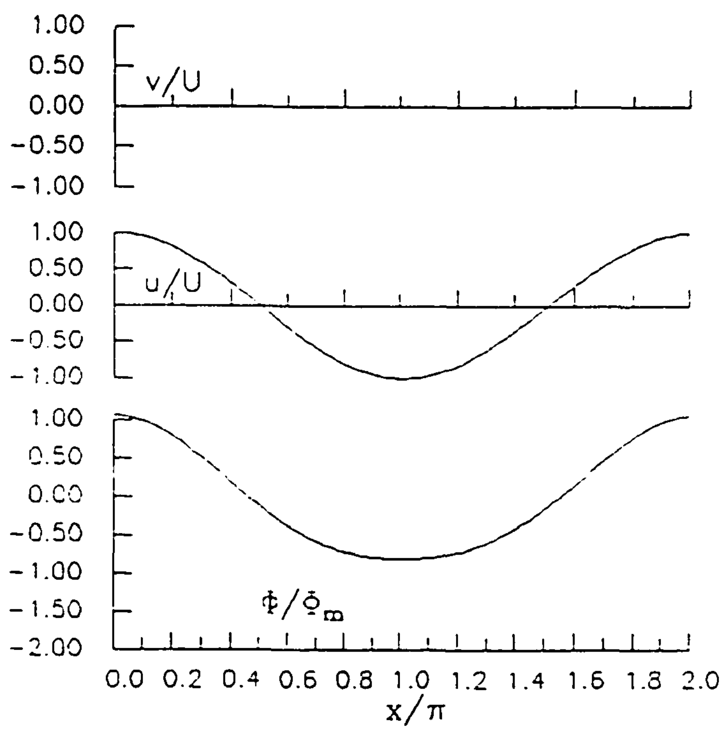

Figure 5.1 Initial conditions for the parallel model runs test.

Values of the parameters in the system are: U = 20 ms^{-1}, f = 10^{-4} s^{-1}, K = 3 X 10^{4} m^2s^{-1}, and ϕ_m = 400 m^2s^{-2}. The parameter values were chosen so that the system produces a hydraulic jump from the smooth initial conditions at a reasonable period of time into the simulation. The hydraulic jump serves as a proxy for one of the targeted applications in three-dimensions -- observing and correcting fronts and outflow boundaries. The relevant non-dimensional parameters for the system are the Rossby number, $R_o = U / fL$, and the Froude number, $F = U / \sqrt{\phi_m}$ (Williams and Hori, 1970). Here, R_o =1 and F=1. The eddy diffusivity constant, K, makes the diffusion term about one order of magnitude less than the most significant other term(s) of the equations.

To produce a forecast different from that of the control run, a parallel run is made using different, non-conservative, discretization of the shallow water equations:

$$u_i^{n+1} = u_i^{n-1} - 2\Delta t \left\{ \begin{bmatrix} u_i^n\left(u_{i+1}^n - u_{i-1}^n\right) \\ -\left(\phi_{i+1}^n - \phi_{i-1}^n\right) \end{bmatrix} / 2\Delta x - fv_i^n - K\left(u_{i+1}^{n-1} - 2u_i^{n-1} + u_{i-1}^{n-1}\right) / \Delta x^2 \right\}$$

(5.4)

$$v_i^{n+1} = v_i^{n-1} - 2\Delta t\left\{\left[u_i^n\left(v_{i+1}^n - v_{i-1}^n\right)\right] / 2\Delta x + fu_i^n - K\left(v_{i+1}^{n-1} - 2v_i^{n-1} + v_{i-1}^{n-1}\right) / \Delta x^2\right\}$$

(5.5)

$$\phi_i^{n+1} = \phi_i^{n-1} - 2\Delta t\left\{\left[u_i^n\left(\phi_{i+1}^n - \phi_{i-1}^n\right) + \phi_{i-1}^n\left(u_{i+1}^n - u_{i-1}^n\right)\right] / 2\Delta x - K\left(\phi_{i+1}^{n-1} - 2\phi_i^{n-1} + \phi_{i-1}^{n-1}\right) / \Delta x^2\right\}$$

(5.6)

Note, this is written in advective form while the "verification" system is written in flux form.

The control run is sampled at every other grid point to produce pseudo observations. Even though the data are provided at grid points they are analyzed as if they were at random locations. For this case the data are provided at time = 1.4 in non-dimensional units, where non-dimensional time is defined by dividing the time by the advective time scale U/L (time = 1.4 is approximately 4 hours for this scaling). The simulations are continued until time = 2.8 where a final comparison of the model with the control run is performed.

In separate runs, the data are brought into the parallel run using several different assimilation methods including a modified Bratseth scheme (Bratseth, 1986, see also Chapter 3) known as analysis correction (Lorenc et al., 1991), phase shifting (in one step), phase correction assimilation (a gradual introduction of the phase error correction over time), and a combination of the analysis and phase correction method where the analysis correction is applied to the phase corrected field.

In separate experiments the phase correction is determined by either the RMS minimization or the correlation maximization technique (see Chapter 4). The shift is determined independently on four equal length segments of the domain overlapping their neighbors by 20%, and the resulting combined shift fields are smoothed 5 times using a 1-2-1 3-point filter to ensure a smooth transition of the shift field between segments.

For the schemes that involve a gradual introduction of analysis or phase corrections, the assimilation is begun at 10 time steps (1000 sec, 0.097 non-dimensional units) before the data time. This allows a comparison of all methods at the observation time for "fit to data", as well as a later forecast time.

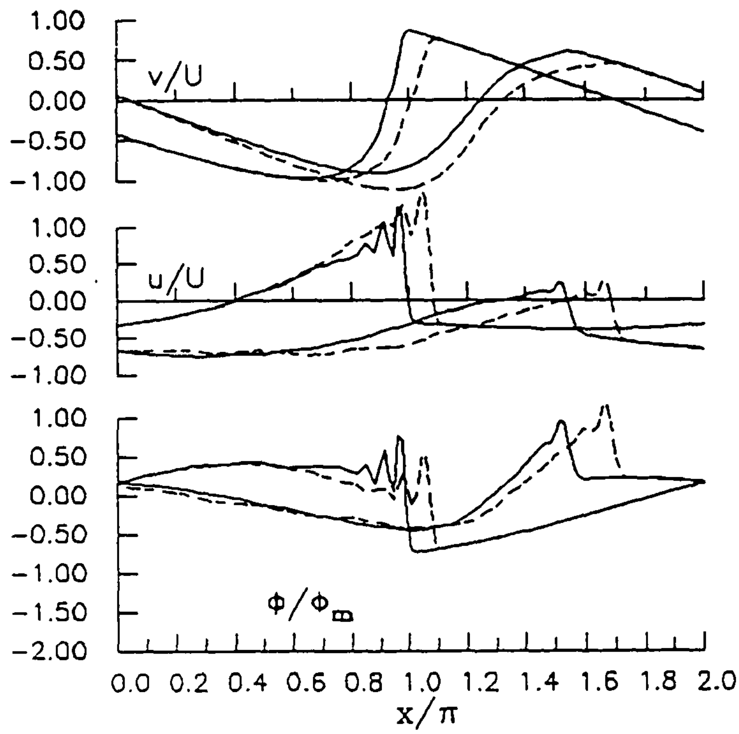

Figure 5.2 Forecasts (advective form, solid line) and verification (flux form, dashed line) fields at non-dimensional times 1.4 (jump on the left) and 2.8 (right). From "No Data" experiment.

Figure 5.2 shows the verification run versus the parallel system with no data provided. Note the phase error which has developed by time 1.4 and is amplified by time = 2.8. It seems to be due to the difference in amplitude of the u wind component just behind the jump; the u component is larger in the flux-form solution. Differences are also found in the amplitudes of the height and v wind component. There is rapid error growth in all variables during the formation of the jump (time = 0.7-1.0). There is a slight decrease in the error level toward the end of the simulation as the amplitude of the disturbance decreases.

A comparison of results of the different analysis and assimilation schemes is shown in Fig 5.3. The total root-mean-square error used in the plots is a measure of the total

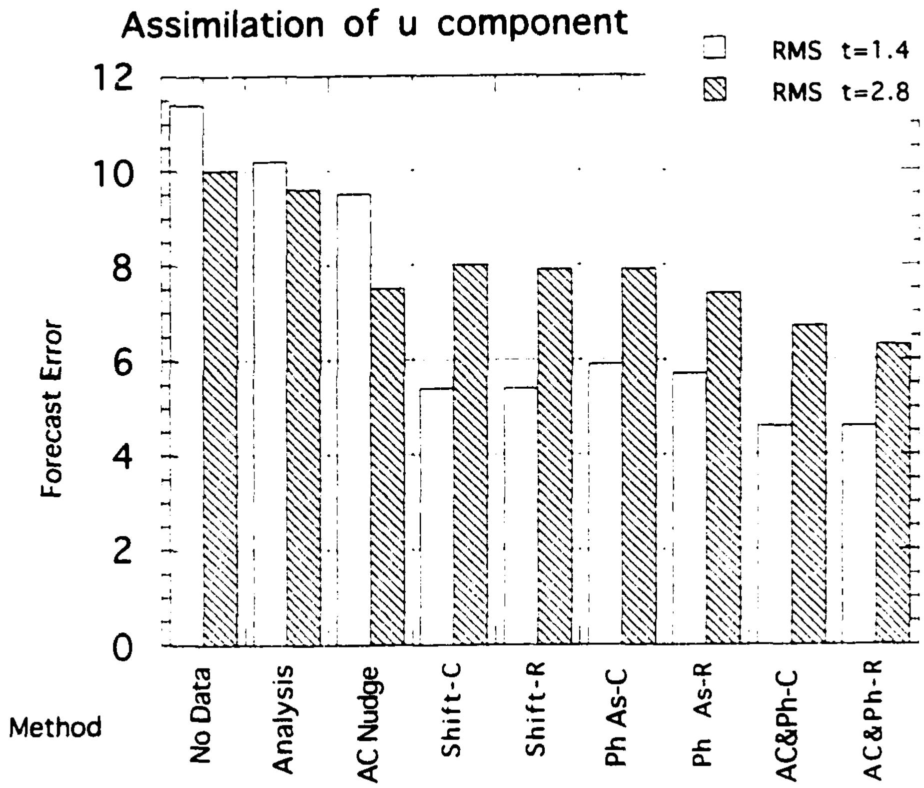

Figure 5.3 Forecast errors (weighted sums of squared errors for 3 variables) for assimilation by each method (different shaded bars) for the 1-D case. The methods are No Data, Analysis at a single time, AC Nudging, a single shift based on correlation (Shift-C)) or RMS (Shift-R), Phase Assimilation based on correlation (Ph As-C) or RMS (Ph As-R), and combined AC and Phase Assimilation based on correlation (AC&Ph-C) or RMS (AC&Ph-R).

fit. It is defined by

$$\sum RMS = \sqrt{\frac{MS(\phi)}{100} + MS(u) + MS(v)} \qquad (5.7)$$

where MS is the mean square error for that particular variable.

Examining a bar chart of the forecast errors for the various techniques (Fig 5.3), one can see the phase correction assimilation combined with analysis correction nudging (labeled AC&Ph-R) produces the best results, both at time=1.4 and 2.8. The advantage (relative to the nudging alone, for example) is smaller at the later time due to the decrease in amplitude of the wave mentioned before.

The gradual introduction of the u wind data using both the AC and Phase correcting appears to be properly propagating the hydraulic jump and allowing the other fields to adjust to the changes in u applied over time (not shown). The analysis alone suffers from having only information about the u component, and the shifting of the fields alone does not account for the loss of amplitude in the u field that needs to be corrected. These results do not suggest a clear advantage of either of the methods of shift determination (RMS minimization vs. correlation maximization)

It is of interest to see which fields are most effective in improving the forecast for this system. In Fig. 5.4 we see the results for assimilation of observations of u, v and ϕ observations. Observing the u-wind component is most useful, and the schemes involving a correction for the phase error are the most effective, perhaps because the wind error is the cause of the differences in the propagation speed of the jump. It is worth noting that the techniques that involved correcting for phase error are the least sensitive to the data variable that is provided. For example, the shift-only result is nearly identical for the three variables, while the AC Nudge scheme only is useful when the u wind component is the observed variable.

In a test of sensitivity to data error, errors are introduced to the u-wind component observations using a random error generator with three different magnitudes: 1, 2, and 5 ms^{-1}. The mean error for each assimilation is plotted in Fig. 5.5. Shown as error bars are the standard deviation of the errors from the mean for each group. The single step shift using the RMS seems to have the least sensitivity to the magnitude of the data errors, though the combination techniques still show the lowest mean error in all cases. As mentioned for the result with no data error, the combination technique uses the power of the phase shifting to communicate information from a single variable to all variables, while allowing for adjustment of the amplitude of the observed variable.

Also from this figure we see an advantage of the RMS versus the correlation technique, in that it is less sensitive to random data errors. This result holds for all variables and is true whether a single step shift is applied or a phase assimilation is used.

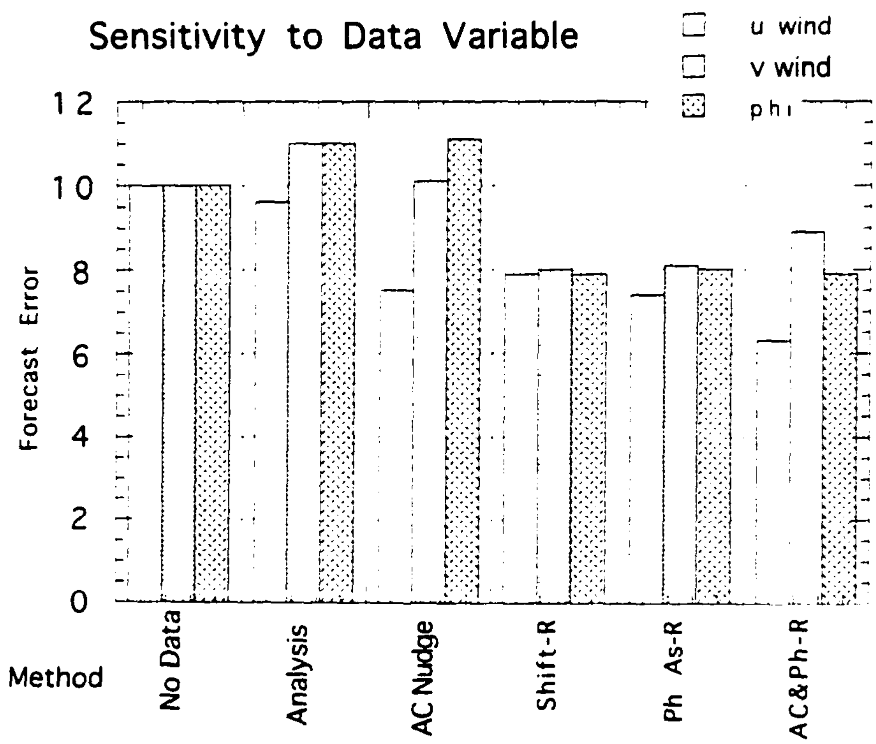

Figure 5.4 Forecast errors (weighted sums of squared errors for 3 variables) showing sensitivity to the data variable that is assimilated.

The most significant improvement of the phase correction compared to analysis was found in variables other than the data-provided variable. In this system, the nudging to one variable is not enough to bring the other variables along correctly without accounting for the phase error. However, the lack of degrees of freedom for a one-dimensional system and the smoothing necessary to control instability near the jump cast some doubt on applicability of these one-dimensional results to more complicated situations, so another experiment was set up in two dimensions.

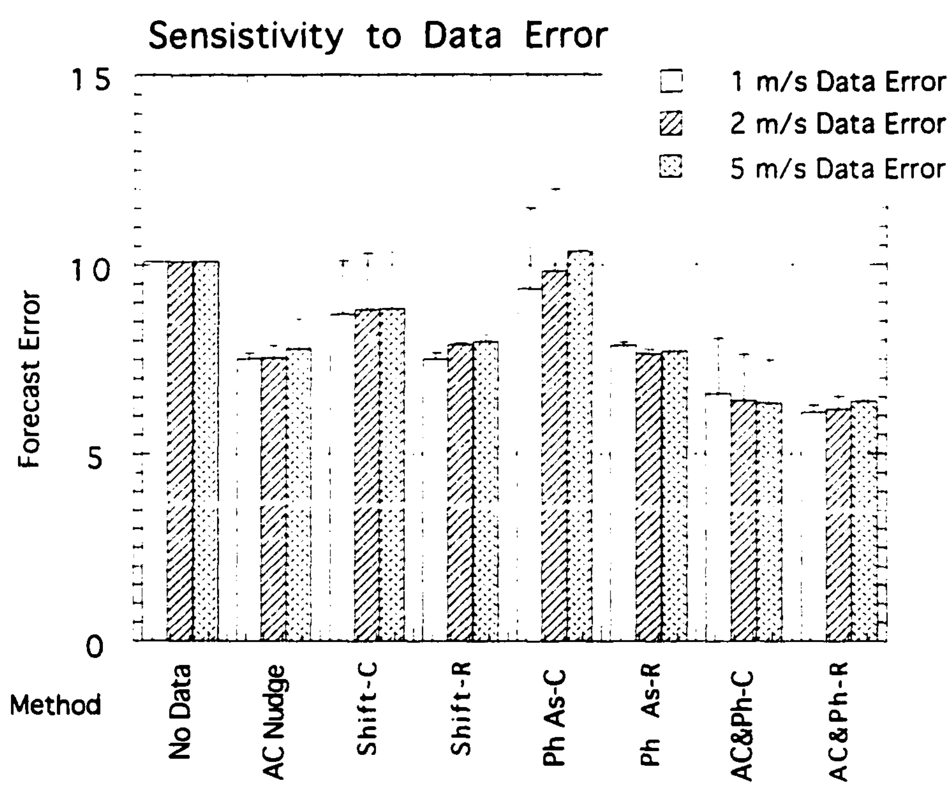

Figure 5.5 Sensitivity to data error for each of the methods in the 1-D test. Assimilation methods labeled as in Fig. 5.3. Note that the "-C" in several of the labels designates correlation-based shifting, in contrast to "-R", RMS based shifting.

5.2 Experiments in Two Dimensions

Consider a two dimensional non-linear shallow water system, written in flux form (e.g., from Grammelvedt, 1968):

$$\frac{\partial \phi u}{\partial t} + \frac{\partial}{\partial x}(\phi uu) + \frac{\partial}{\partial y}(\phi uv) - f\phi v + \phi\frac{\partial \phi}{\partial x} = 0 \tag{5.8}$$

$$\frac{\partial \phi v}{\partial t} + \frac{\partial}{\partial x}(\phi uv) + \frac{\partial}{\partial y}(\phi vv) + f\phi u + \phi\frac{\partial \phi}{\partial y} = 0 \tag{5.9}$$

$$\frac{\partial \phi}{\partial t} + \frac{\partial(\phi u)}{\partial x} + \frac{\partial(\phi v)}{\partial y} = 0 \tag{5.10}$$

where $\phi = gh$, g is gravity, h is the height of the fluid, and f is the Coriolis force with a beta-plane approximation, $f = f_0 + \beta y$. Boundary conditions are periodic east-west and rigid wall north-south.

For the test simulation we initialize the height field with a long wave westerly flow with some perturbations:

$$\begin{aligned} h(x,y) &= H_0 + H_1 \tanh\frac{9(y-y_0)}{2D} \\ &+ H_2 \operatorname{sec}h^2 \frac{9(y-y_0)}{D}\left[0.7\sin\left(\frac{2\pi x}{L}\right) + 0.6\sin\left(\frac{6\pi x}{L}\right)\right] \end{aligned} \tag{5.11}$$

where: $H_0 = 2$ km, $H_1 = -220$ m, $H_2 = 133$ m, L=6000 km, D =440 km, f_0=10^{-4} s^{-1}, g=10 ms^{-2}, and β=1.5 x 10^{-11} s^{-1} m^{-1}. The initial winds are geostrophic.

The equations are integrated using a generalized Arakawa scheme on a C grid (Scheme I, Grammelvedt, 1968) as the control run. In a parallel run the Janjic' scheme on an E grid (Janjic', 1984) is used to integrate the equations. The models are run for 5

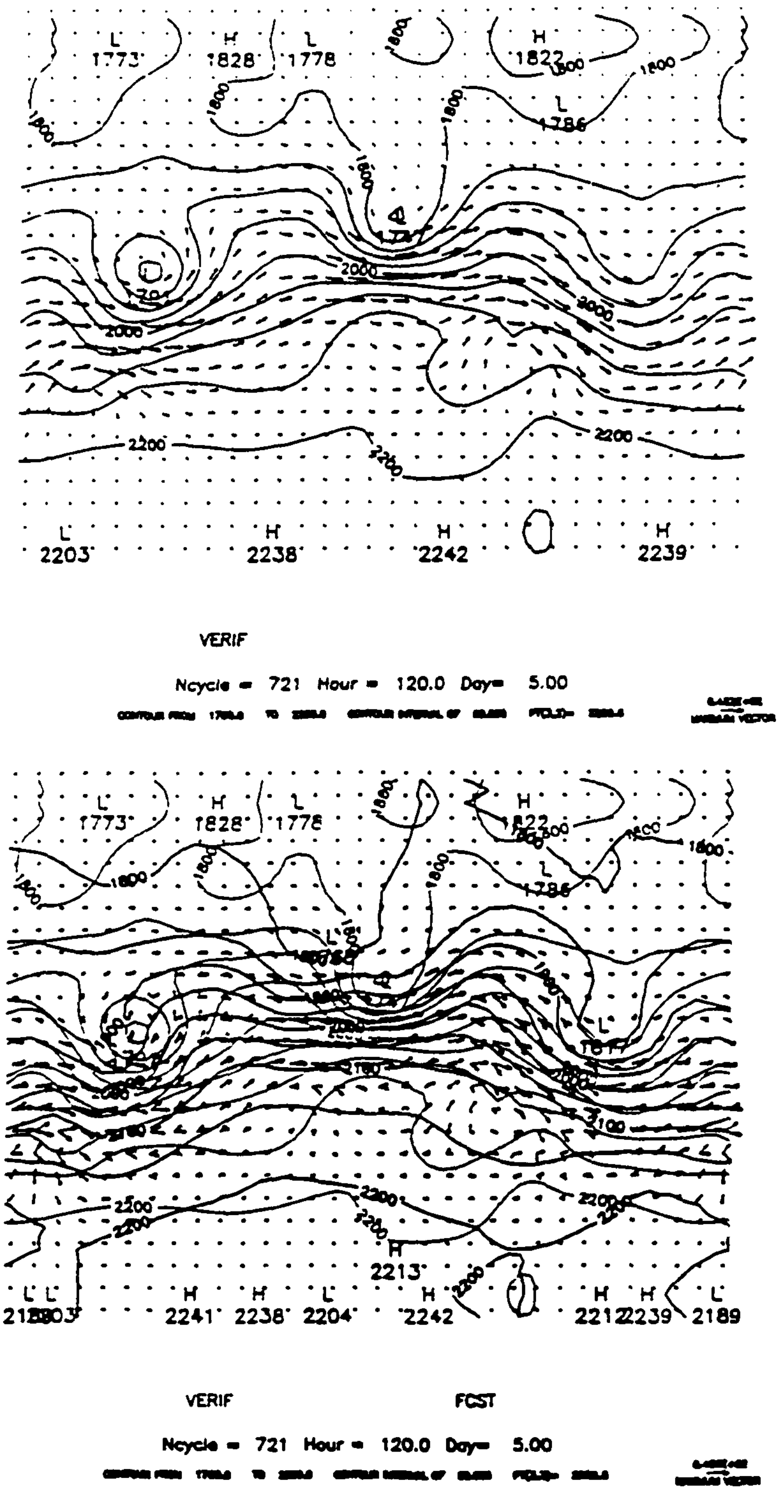

Figure 5.6 Five day forecast of height (m) and wind (ms-1), see scale in lower right. a) verification, the Arakawa numerical method, b) Janjic' numerical method overlaid on the verification run.

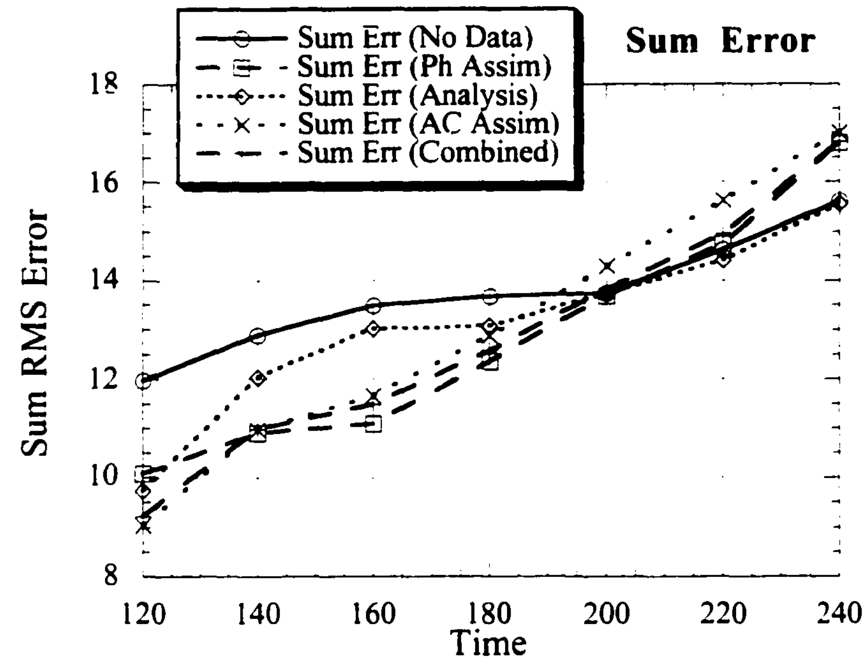

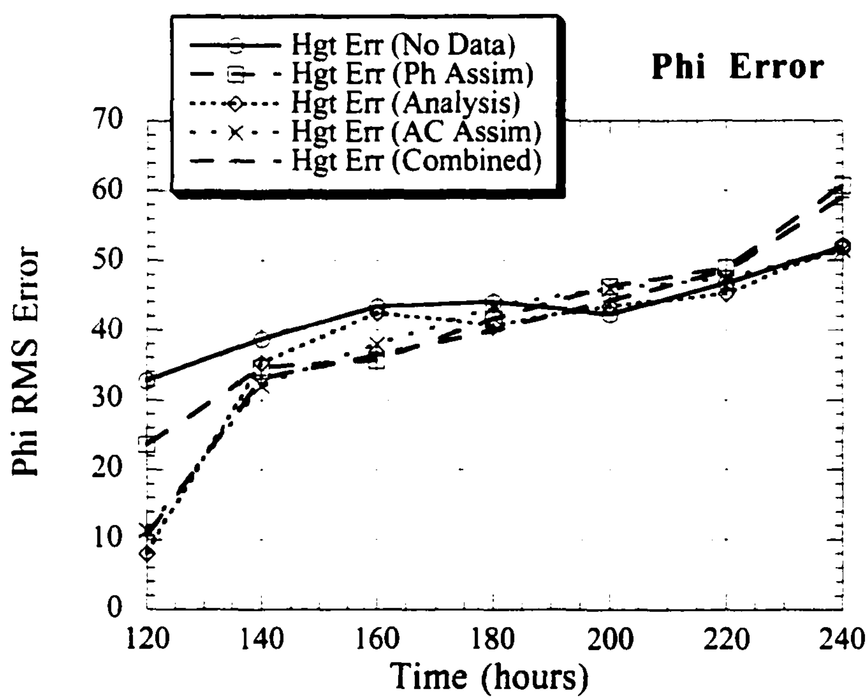

Figure 5.7 Forecast errors for the 2-D case, for 5 assimilation methods. Combined analysis and phase assimilation (Combined), Phase assimilation only (Ph assim), AC Analysis (Analysis), analysis correction assimilation (AC assim), and No Data. a) Sum of RMS errors, b) Errors in ϕ only.

days, by which time the solutions have diverged. Figure 5.6a shows the Arakawa solution, which is arbitrarily considered the verification solution, and Fig. 5.6b the second solution overlaid on the verification run. Note that both phase and amplitude differences are present.

The assimilation system is then asked to bring the Janjic' system into agreement with the Arakawa "verification" solution. From the assimilated state, the model is run forward for another 5 days, and the forward forecasts are compared to the control along the way. The forecasts were scored using the total RMS statistic defined in the previous section.

As in the one-dimensional system experiments, several schemes for assimilation were tested, a Bratseth analysis (Analysis), the AC assimilation (AC Assim), a phase shift gradually introduced over time, phase assimilation (Ph Assim), and a combination of AC assimilation and phase assimilation (Comb). RMS minimization is used for the determination of the phase error from the data.

Figure 5.7 shows the forecast errors for the two-dimensional case during the forward forecast period after assimilation of height data at 120 hours. The combined scheme (Comb) produces the best forecasts out to 200 hours. The advantage doesn't hold up after that time, but the differences between the assimilation systems are relatively small compared to the differences within 30 hours of the data. This could be a reflection of the predictability limits of this system.

As in the results for the one-dimensional system, the combined scheme is able correct other than the observed field at the time of the data, by advancing or retarding the balanced waves, and is also able to correct for any amplitude errors in the height field, unlike the phase assimilation alone or a single step shift (not shown).

Chapter 6 OSSE Experiment in Three Dimensions

6.1 Experiment Set-up

In order to test the phase-error detection scheme and to determine which of the proposed correction methods might work best on a problem in three-dimensions, a demonstration involving a thunderstorm simulation is devised. The model is run using a horizontally homogeneous environment, which is specified by a sounding launched at Ft. Sill, Oklahoma on the afternoon of May 20, 1977. This case has been studied from both an observational (Ray et al., 1981) and numerical modeling standpoint (Klemp et al., 1981 and Klemp and Rotunno, 1983). The ARPS model is known to produce a supercell thunderstorm when initialized with a single warm temperature perturbation (Xue et al., 1995). In reality, a supercell thunderstorm developed on this day, produced a damaging tornado in central Oklahoma, in Del City. The case is colloquially known as, "The Del City Storm."

The model is run in a coordinate system moving with the mean wind. This allows the simulations to be run in a reasonably small domain as the storms won't move too far from their initial position in the model grid. For this work convection is initiated by two distinct 4° C temperature perturbations ("bubbles"). Two 2-hour simulations are run. The two simulations differ in the location of the initial warm bubbles. The goal of the test is to correct the control simulation for its position error with respect to the verification run.

After the model is allowed a half-hour to develop thunderstorms, remapped-radar observations are simulated by "observing" the control run with a radar located 30 km south of the model domain's southern boundary. The radar observations are simulated assuming the WSR-88D storm-mode radar scanning pattern (14 distinct elevation angles) and observations are created only where the modeled reflectivity (determined from the model hydrometeor fields) exceeds 10 dBZ. Although the storms are well sampled, there are still gaps in the coverage due to the finite number of elevation angles in the scan pattern.

6.2 Results

Figures 6.1a and b show a horizontal slice at 30 min. at a height of 4 km through a sub-domain of the control and verification simulations, respectively. The boxes on Fig. 6.1 indicate the approximate center of the maximum updraft in the verification run. Due to the differences in the locations of the initial temperature perturbations, we see that the storms in the control simulation are mispositioned relative to the verification, with the southern storm showing a larger error. There are also some differences in storm structure, particularly in the northern storm, due to differences in storm interactions.

The phase error algorithm was run using the simulated radar data; the RMS minimizing scheme was used with 3 iterations. Figure 6.2 shows vectors indicating the position errors identified by the algorithm. Generally, the algorithm correctly diagnosed the position error, though the fact that two close storms require differing corrections combined with the application of the smoother so that the corrections vary smoothly in space) leads to some compromises in the region between the storms. Figure 6.3a shows the effect of the single-step phase-correction procedure. The locations of the updraft centers are handled fairly well, and the vertical velocity extrema are preserved well.

The phase-assimilation (nudging-type) correction was applied in 10 steps over a 10-minute window from t=20-30 min. In that case (Fig 6.3b) the positions of the storms were adjusted fairly well, but the southern storm is not as well positioned as in the single-step case (about 4 km off). Of greater significance is the loss in amplitude in the vertical circulations of the storms, the range in vertical velocity was reduced to

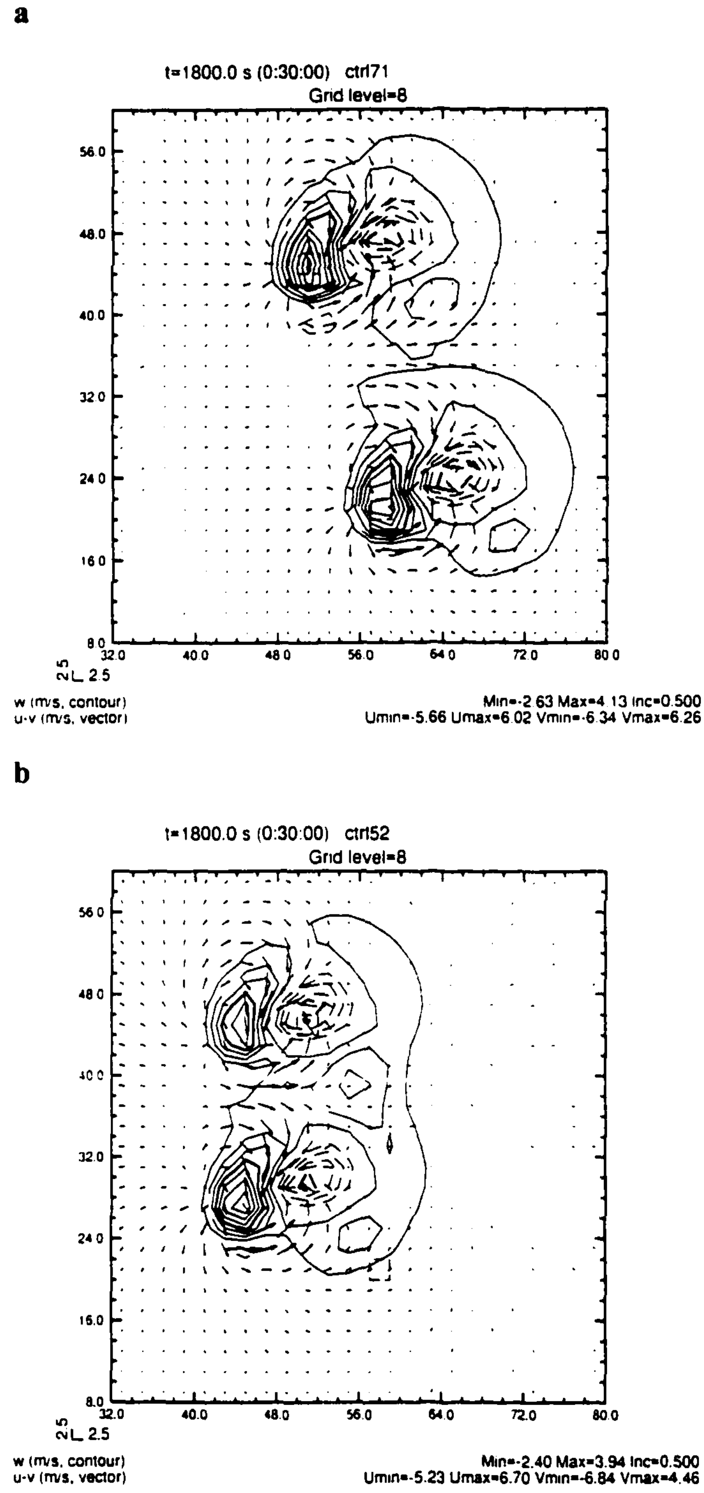

Figure 6.1 30 min. thunderstorm forecast. Horizontal winds and vertical velocities (0.5 ms-1) intervals) at 4-km AGL. Distance scale is in km. a) Verification b) Control. Dashed boxes in figures indicate the location of the maximum updraft in the verification run.

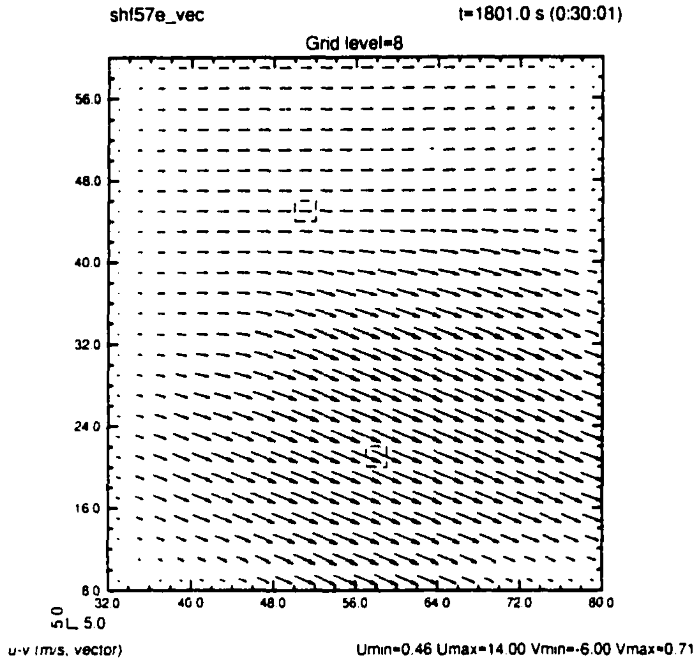

Figure 6.2 Phase correction vectors necessary to correct the control run to match the verification run. Vector units are km.

-1.1 to +1.8 ms^{-1}. This is because each adjustment step has an implicit smoothing due to the interpolation involved. Second-order interpolation was used, but apparently higher order interpolation or fewer correction steps are needed to preserve the magnitude of the storm updrafts in this case.

Figure 6.4 shows the storms after the pseudo-velocity adjustment has been applied in a window from 20-30 min. The convergence and updraft of the southern storm is enhanced, and it has not been shifted to the south quite enough.

It is likely that the single-step shift is most accurate because it is most consistent with the method used to identify the phase error at t=30 min. Correcting the error using a pseudo-wind over time might best be done knowing the error in the trajectory of the storms over that time period rather than a snapshot at the end.

a

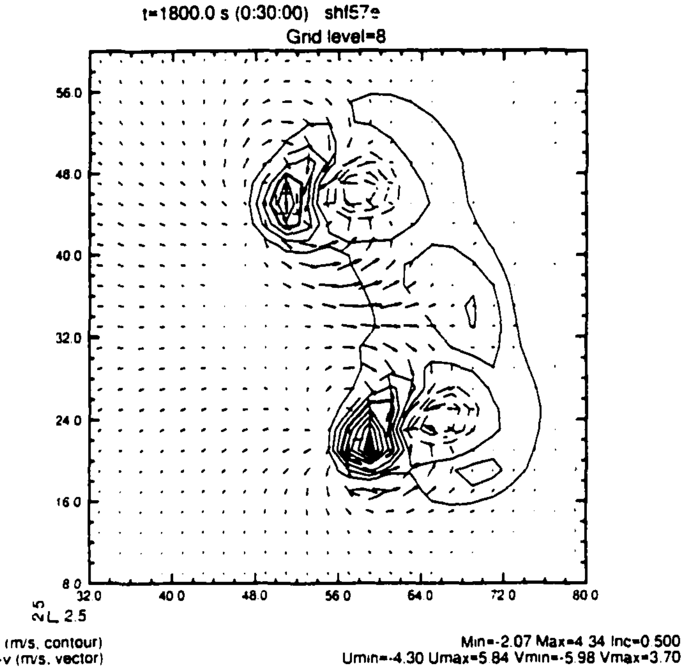

b

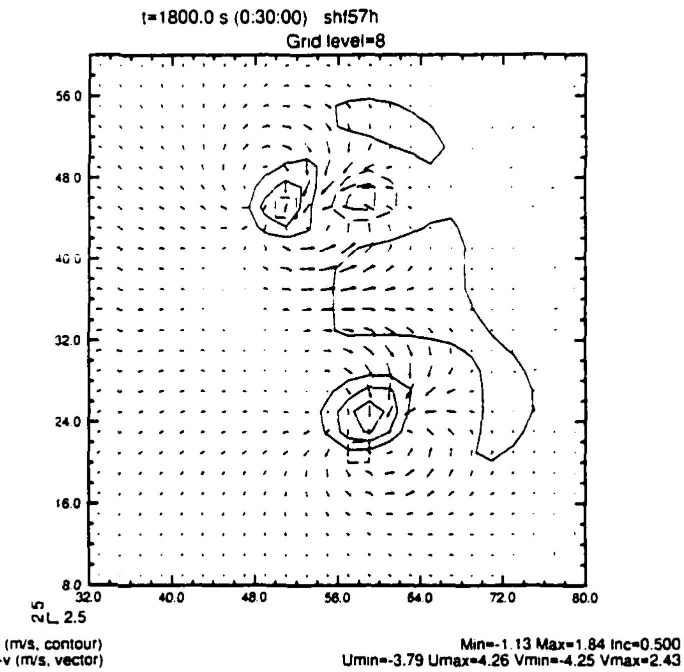

Figure 6.3 Phase adjusted forecast at 30 min. (data time). a) single-step phase correction, b) phase correction in multiple steps. Compare to verification in Fig. 6.1a.

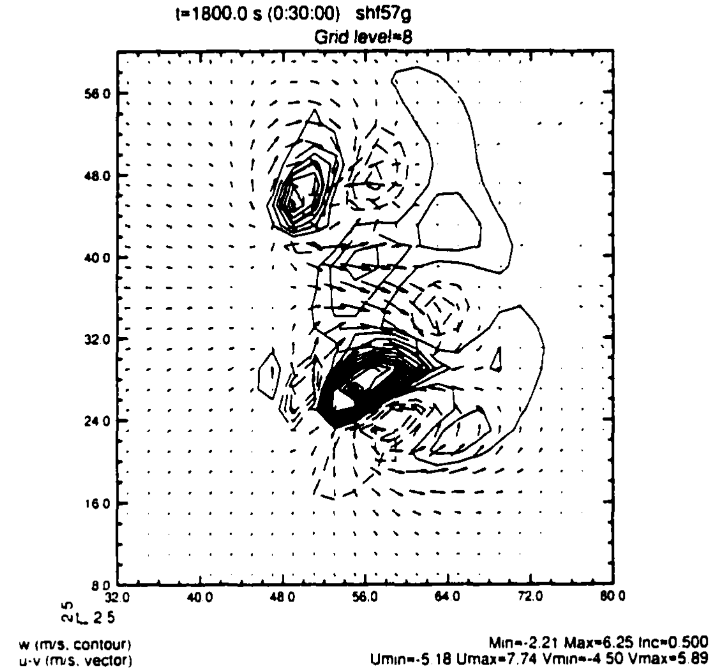

Figure 6.4 Adjusted thunderstorm forecast at 30 min. (data time) for pseudo-wind phase correction.

Besides examining the effect of the corrections at the time of observations it is important to examine how the corrections affect the forecasts beyond that time. Figure 6.4 shows the prediction at 90 min. for the verification run. During the period the storms have gone through a declining phase and then redeveloped, but the displacement differences between the verification and control are maintained

Also, differences in storm interaction left the southern storm much weaker in the control run (w=2 ms^{-1}) than the verification. The result of the forecast after the single-step correction is shown in Fig. 6.6a. The phase correction has been successfully applied, and it has correctly depicted the strength of the updraft in the southern storm. There is a bit of spurious development between the cells, however. Given that it started out to be weaker, it is not surprising that the phase-nudged forecast continued to predict much weaker vertical velocities, and there is no redevelopment of the northern storm due to the weakened circulations. From Fig. 6.7, we see that the advection

a

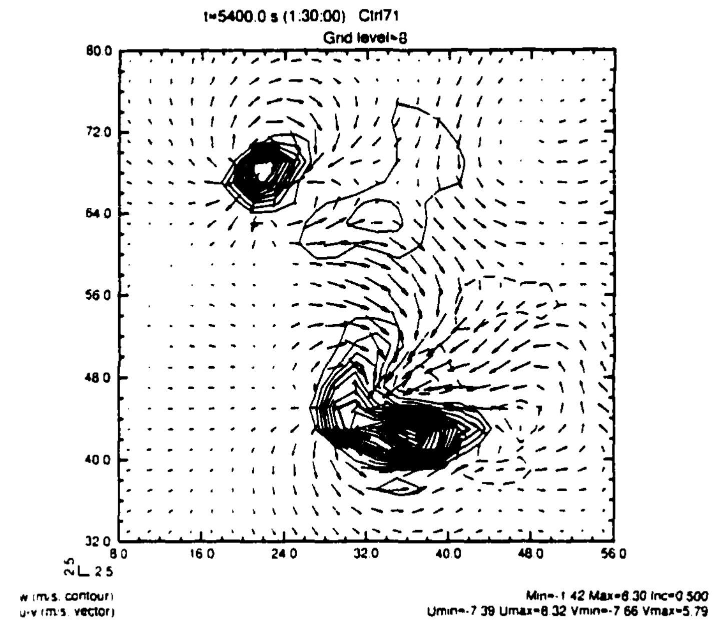

b

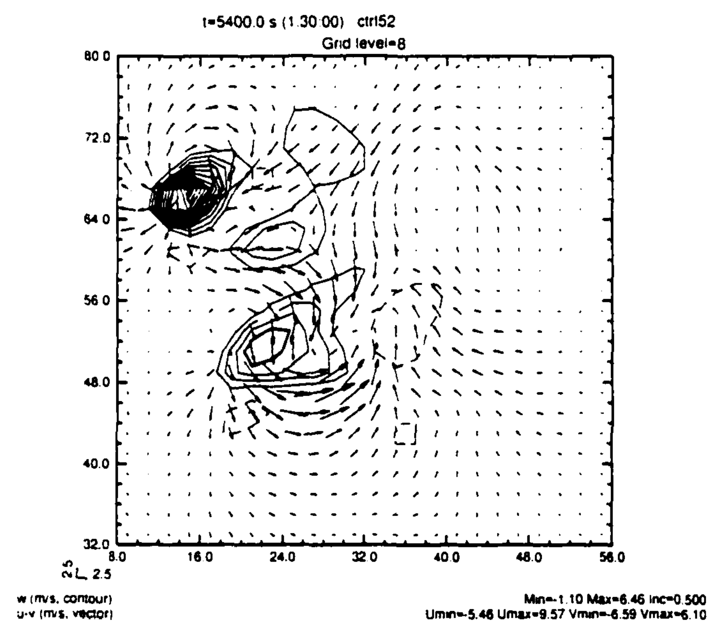

Figure 6.5 Thunderstorm simulation at 90 min., a) verification, b) control.

a

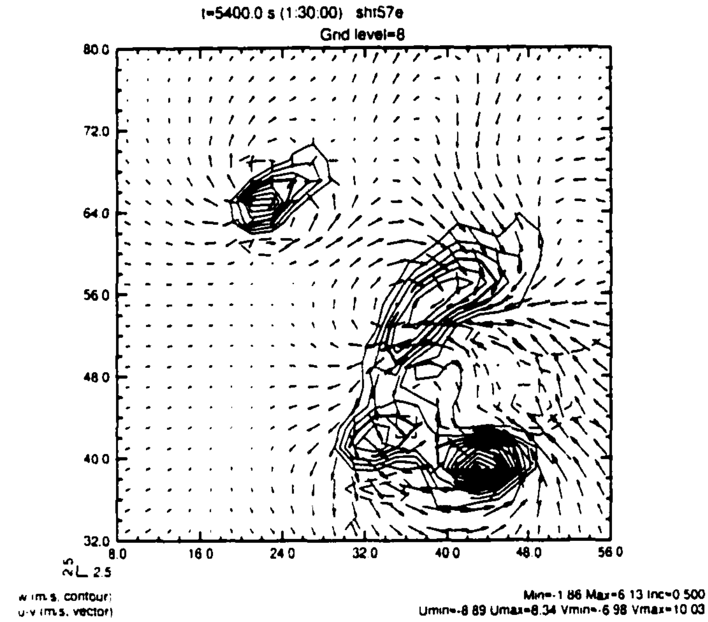

b

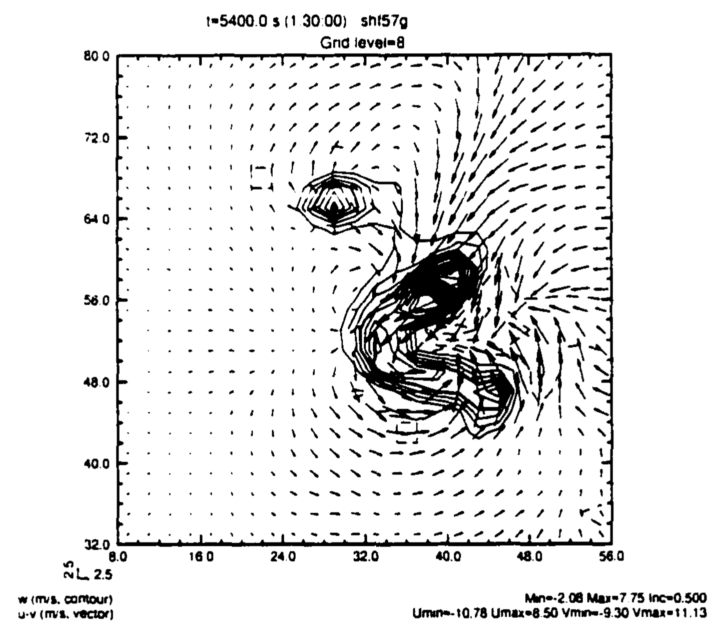

Figure 6.6 Thunderstorm forecast at 90 min. a) single-step shift, b) multiple small steps.

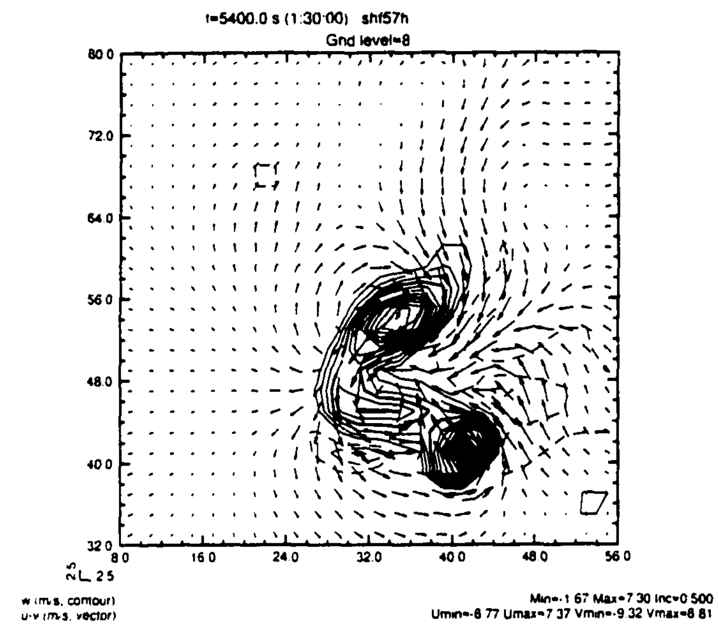

Figure 6.7 Adjusted thunderstorm forecast at 90 min. for the pseudo wind phase correction.

correction scheme has successfully predicted the stronger southern storm, but some spurious development between the storms is even stronger than the single-step correction run.

6.3 Discussion

The three-dimensional OSSE demonstration shows that position errors in thunderstorm initiation can be corrected by a phase-correction scheme, even in a case involving storm interactions and secondary development. For this case, it seems that the correction is best applied as a single step, though it is recognized that cases involving larger corrections may favor one of the other methods. The success of the single-step correction bodes well for its use as a preconditioning step for other analysis and assimilation techniques.

It is found that the smoothing implicit in the interpolations required for the phase-nudging technique can diminish the storm updrafts, which are marginally resolved in these 2-km grid-spacing simulations. The advection correction method has some success but shows some artifacts whose cause needs to be determined, but may be due to the inherent differences between the method used to determine the phase error and that being used to correct it.

The simulations presented here represent a fairly basic challenge for many aspects of the scheme. Sensitivity to data error and cases involving real-data and larger spatial errors will be tested next. Also, the scheme will be expanded to include data from other sources. Mesonet data are expected to be useful in positioning gust fronts and dry-lines, for example. It may be worthwhile to pursue modifications to the advection correction scheme to try to resolve the difficulties noted here. Perhaps an adjustment period centered in time, or more continuous in time (but computationally expensive) determination of the phase error may produce a better advective correction.

Chapter 7 Frontal Boundary Analysis

7.1 April 9, 1995 Synoptic Setting

The case of April 9, 1995 will be used to test the phase shifting algorithm in a real data situation involving a front in central Oklahoma. This day featured a slow-moving front in central Oklahoma which was observed by the Twin Lakes (Oklahoma City area) WSR-88D radar, KTLX, which scanned in clear-air mode for part of the afternoon. Data from the radar and Oklahoma Mesonet, as well as standard surface observations give a good depiction of the front and its characteristics, making it a good case to test the schemes for analyzing a front. This section describes the synoptic conditions on this day.

At 1800 UTC the surface map (Fig 7.1) showed a surface front across central Oklahoma. Winds were northerly to northwesterly at 5-8 ms^{-1} behind the front, and southerly to southwesterly 5-20 ms^{-1} ahead of the front. There was a fairly strong temperature contrast with temperatures of 26-30 C in the warm sector, and temperatures dropping from the low 20s (C) near the front to the low teens in far northwest Oklahoma, behind the front. The front had progressed almost 100 km toward the southeast (16 kmh^{-1}) since 1200 UTC (not shown).

Aloft, at 500 hPa (Fig. 7.2b), the flow was southwesterly, with a broad trough centered over southern Utah. The 250 hPa wind field (Fig. 7.2a) featured a jet of 55 ms^{-1} rounding the bottom of the trough in northern Arizona. Jet-level winds over Central Oklahoma were about 25 ms^{-1} and quite distant from the circulation expected with the jet streak. At 700 hPa (Fig 7.3a) the flow was also southwesterly, nearly parallel to the frontal boundary. Conditions at 850 hPa (Fig. 7.3b) reflected those of the surface front, with an area of high relative humidity behind the front associated with cloudiness there. Cloudiness behind the front reduced solar insolation there during the morning, helping to maintain the thermal contrast.

With the 500 hPa trough being far to the west, there apparently was not a significant synoptic scale lifting mechanism on the front and, in fact, convection did not initiate until nearly 00z, and only small cells were produced at that time (see Fig. 7.4). A significant wave did arrive overnight, evidence that the primary synoptic forcing was still off to the west during the afternoon.

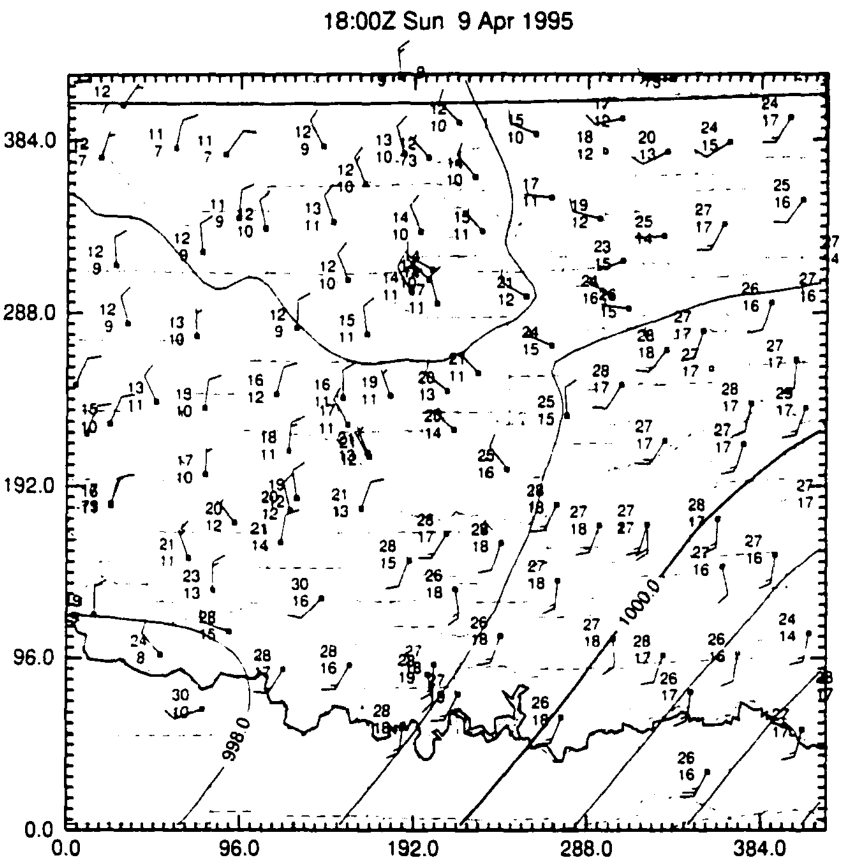

Figure 7.1 Surface weather map for 1800 UTC 9 April 1995. Station model and sea level pressure analysis (contour interval 2 hPa) from the 1800 UTC RUC analysis. Station model includes temperature (upper, degrees C) and dew-point (lower, degrees C), wind barbs are in ms^{-1} with a full barb representing 5 ms^{-1} and half barb 2.5 ms^{-1}.

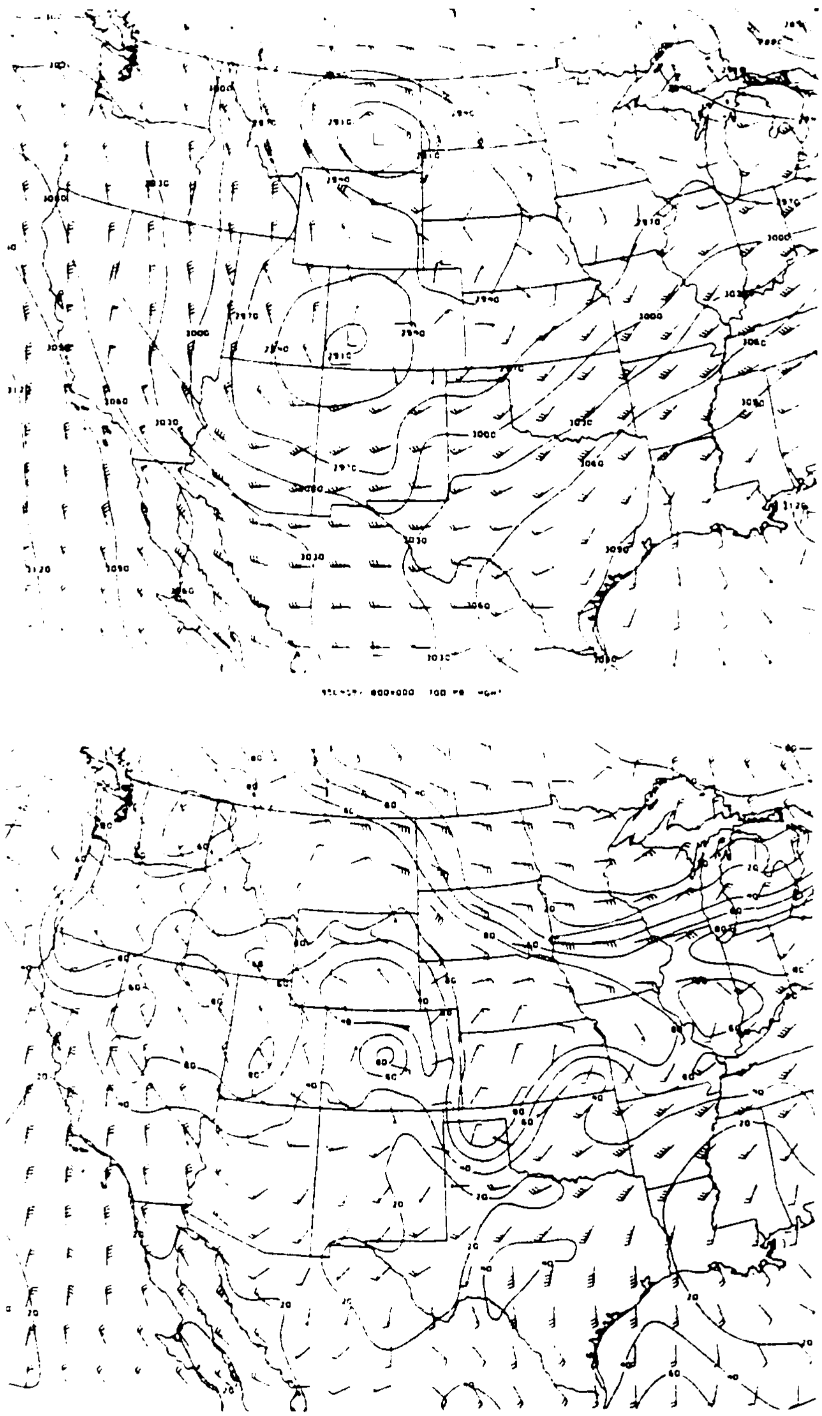

Figure 7.3 Upper level RUC analyses for 1800 UTC 9 April 1995. a) 700 hPa heights (m) and wind barbs in knots, b) 850 hPa relative humidity and wind barbs in knots.

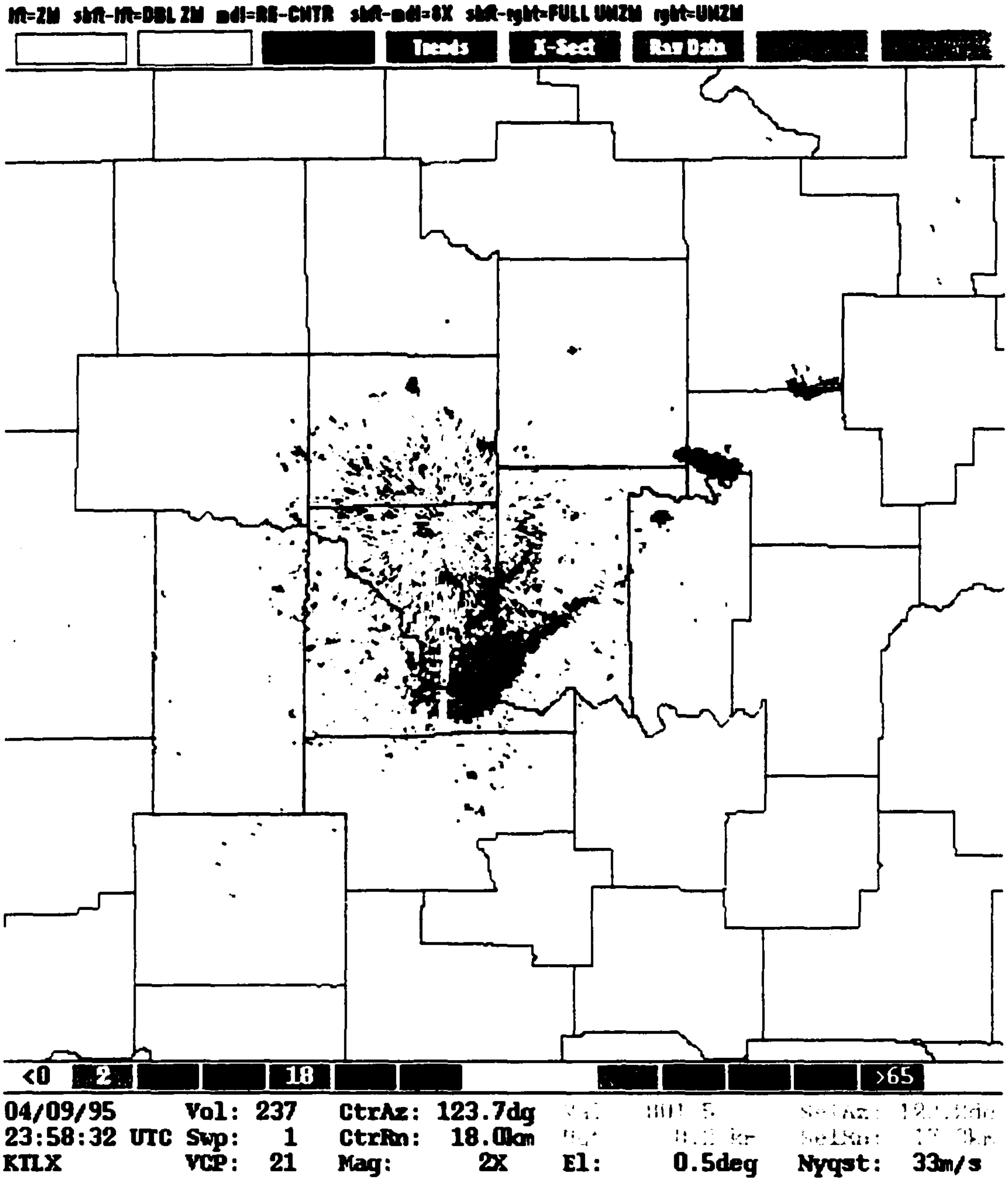

Figure 7.4 Twin Lakes (KTLX), Oklahoma, radar reflectivity (dBZ) 2358 UTC 9 April 1995.

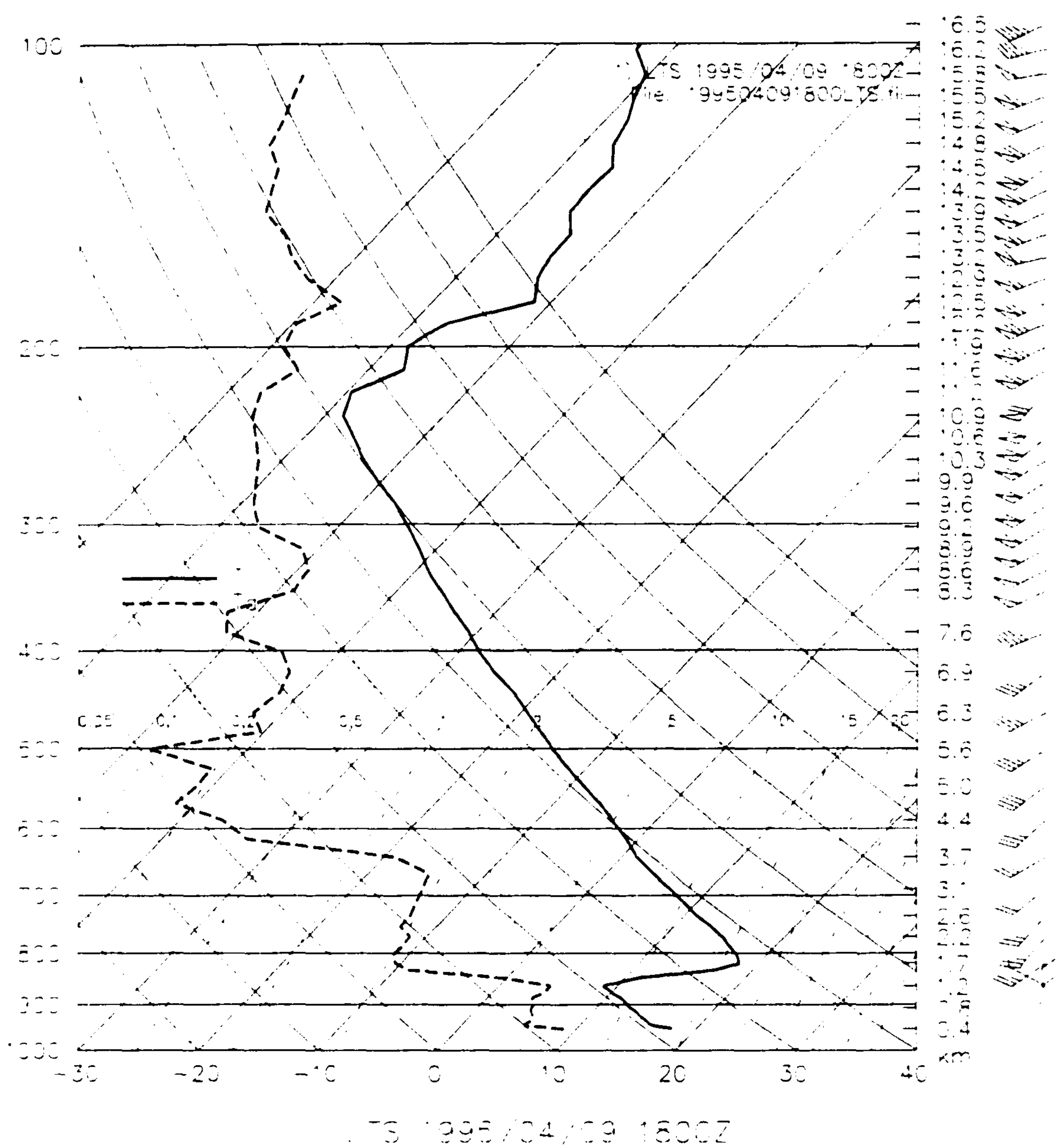

Figure 7.5 Skew-T plot of sounding taken at Altus, Oklahoma at 1800 UTC 9 April 1995. Temperature and dewpoint (C), winds in knots.

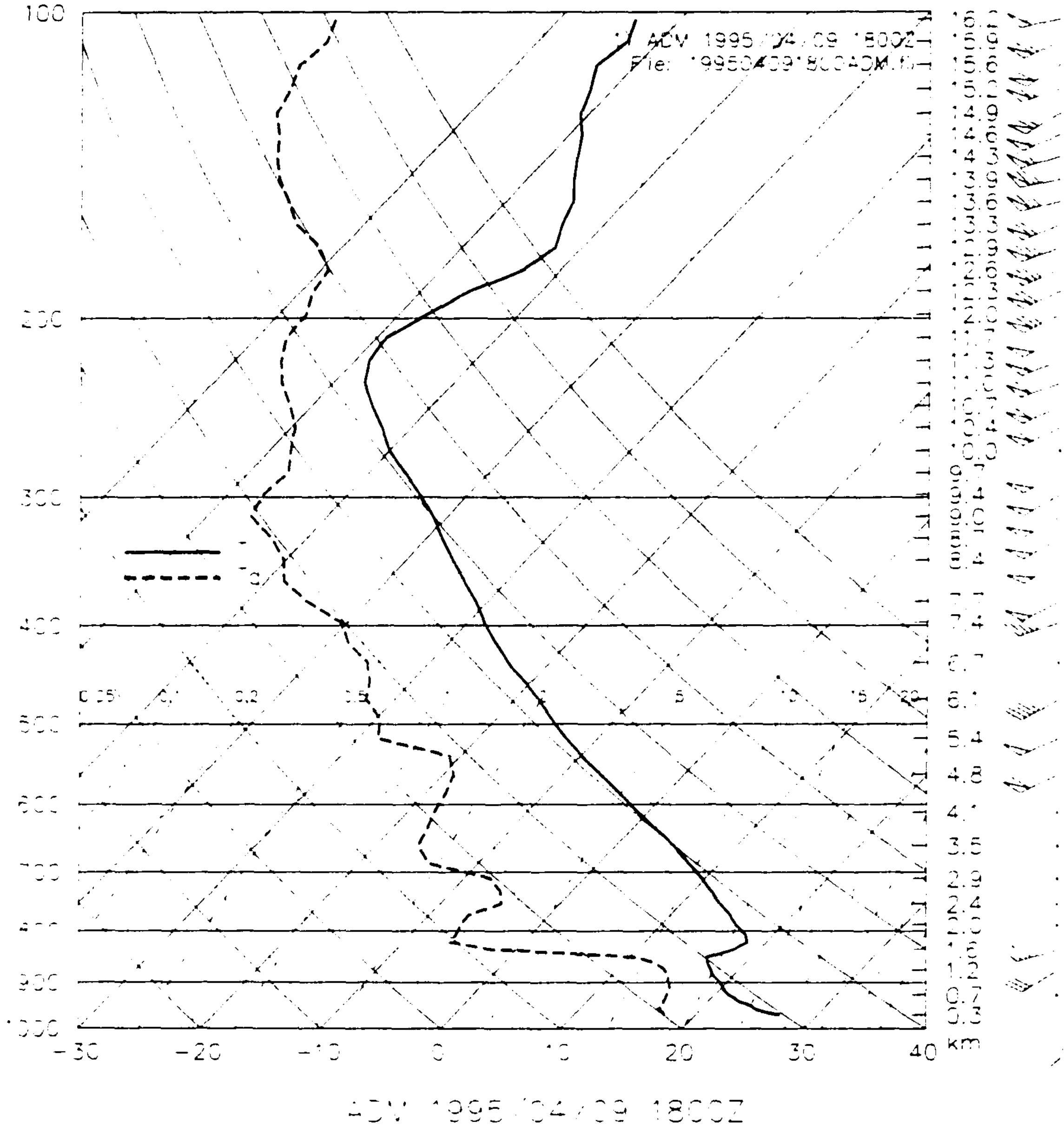

Figure 7.6 Skew-T diagram of sounding taken at Ardmore, Oklahoma at 1800 UTC. As in Fig. 7.5.

The thermodynamic stability and contrast between the two sides of the front are illustrated by two soundings taken on either side of the front at 1800 UTC, one at Altus, Oklahoma (Fig. 7.5) in the cold air and one at Ardmore, Oklahoma (Fig. 7.6) in the warm air. The air in the warm sector was obviously unstable, with afternoon convective available potential energy (CAPE) expected to be around 3000 Jkg^{-1}.

The forecasting questions of the day concerned the progression of the front during the day, where it might be when convection is triggered, and whether there was enough convergence with the front to lift air enough to overcome the capping inversion and, if so, whether significant convection would be produced.

Between 1800 and 0000 UTC on April 10, the front moved very little and actually retrograded in some areas of eastern Oklahoma, as seen by the 0000 UTC surface map (Fig. 7.7). There was only enough lift to produce a few small cells, including one near Shawnee, Oklahoma, that produced limited precipitation. Thus, it appears the lifting was not strong enough nor widespread enough to produce a significant outbreak of severe weather despite the instability present. Therefore, it will be a challenge for the numerical forecast to not overforecast the convection and the lack of overwhelming synoptic dynamics will allow the opportunity to study how well the model and analysis can perform on the small-scale features of the boundary.

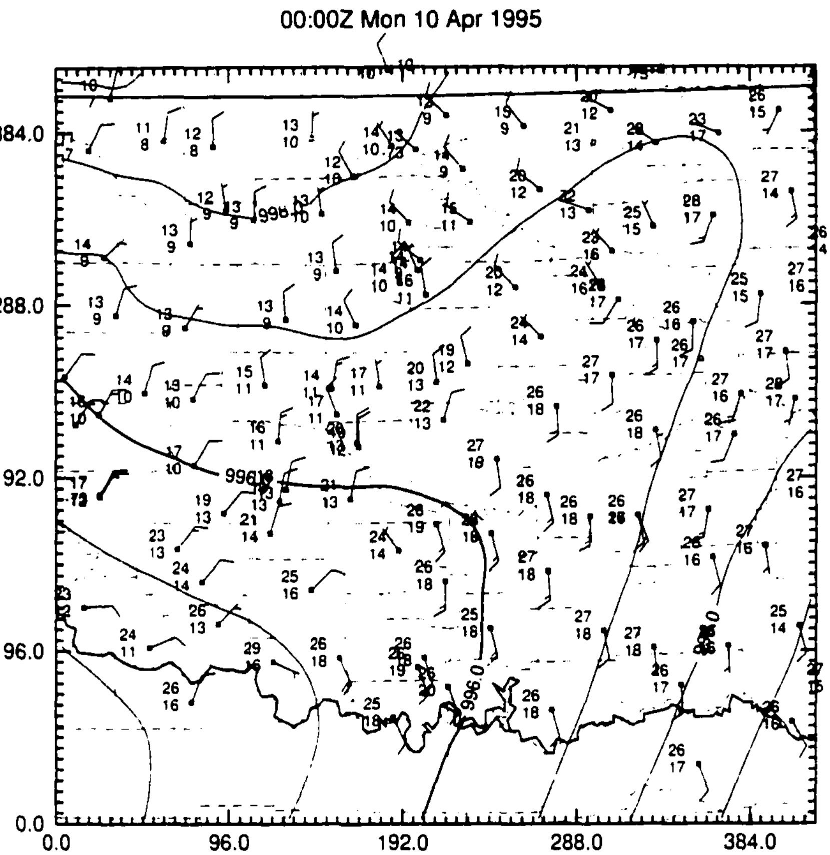

Figure 7.7 Surface weather plot for 0000 UTC, 10 April 1995. As in Fig. 7.1.

7.2 Forecast Experiment

Analysis and forecast domains are set up for this case as shown in Fig 7.8. The forecast analysis process is diagrammed in Fig 7.9; a 12-km forecast is started at 1800 UTC using the 1800 UTC RUC analysis as a background and ADAS analysis of the surface data at that time. A 3-hour forecast is made to 2100 UTC when the analysis and phase shift testing will take place. Subsequently, a 3-km forecast will be made to 00z using the 12-km output at 30-min intervals for lateral boundary conditions (one-way nesting).

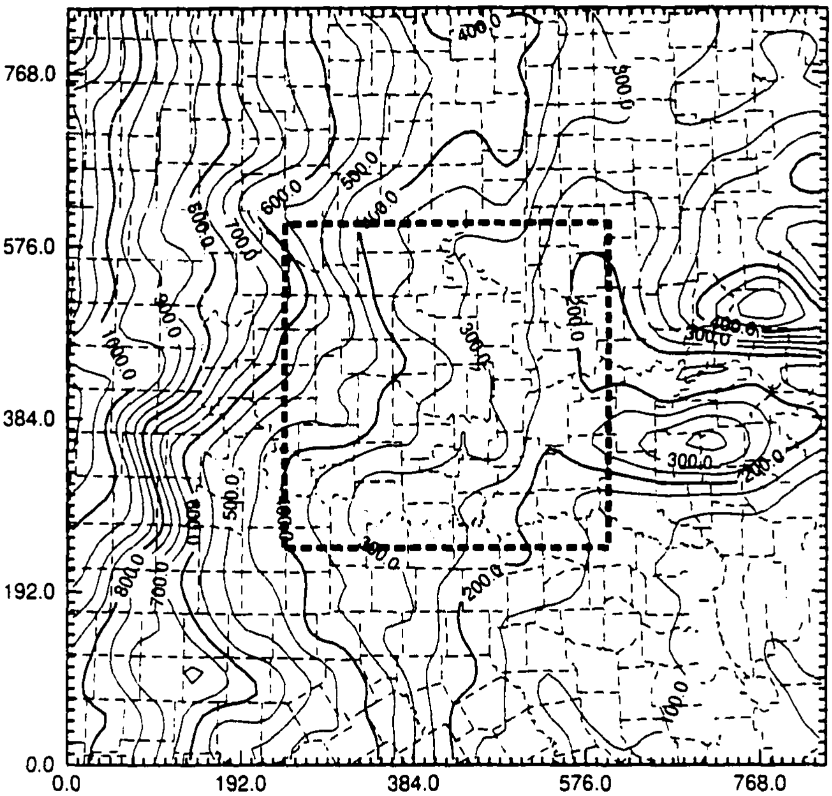

Figure 7.8 Model domains for the 9 April 1995 case. Terrain (m) over the 12-km domain. Box indicates the location of the 3-km grid.

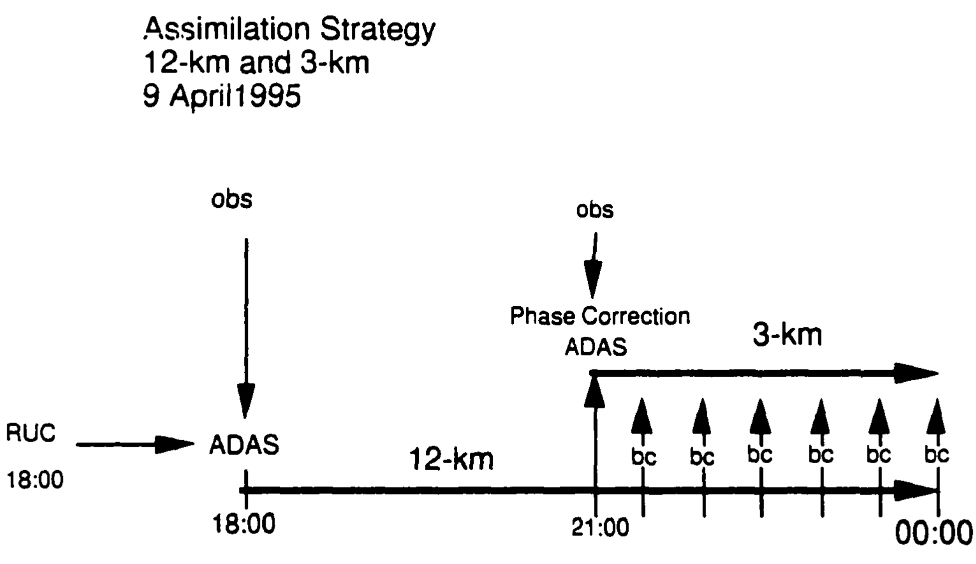

Figure 7.9 Forecast and assimilation flow chart for the 9 April 1995 frontal analysis demonstration.

As depicted in Fig. 7.10, at 2100 KTLX is operating in clear air mode. That is, operating parameters are set for maximum sensitivity to weak echoes -- echoes in the display are of insects and turbulent eddies in the boundary layer and not noise or ground clutter (except within 10-km of the radar). The boundary is quite close to the radar so both the reflectivity and velocity (not shown) data give an accurate and detailed depiction of the front. Some interesting variations are evident along the front, most notably the wave in southern Pottowatomie County (near the center of the figure).

Figure 7.11 shows the results of a 3-hour 12-km scale forecast valid at 2100 UTC, interpolated to the 3-km domain. Comparing the forecast winds (evenly spaced barbs) to the mesonet-observed winds (barbs with station circles), and focusing on those along the central southwest-to-northeast diagonal of the figure, one can see the forecast placed the front slightly to the west of the observed position. The position error is perhaps easier to discern looking at the location of the shift in the v-wind component from south to north (negative to positive), as seen in Figure 7.12.

Radar data, including radial velocity data, and Oklahoma Mesonet observations are used to correct for the phase error. The RMS-minimizing technique, using all the observed variables except pressure, is employed. The resultant phase error vectors are shown in Figure 7.13. Note the translations to the east and south diagnosed in the western part of the domain which act to reposition the front. These vectors are part of a three dimensional field and decrease aloft. For example, the phase errors indicated at the 14th grid level (about 800 m AGL) show less translation (Figure 7.14). These translations are dominated by the radar data as the surface data has a small impact at this height (through the 3-dimensional smoothing).

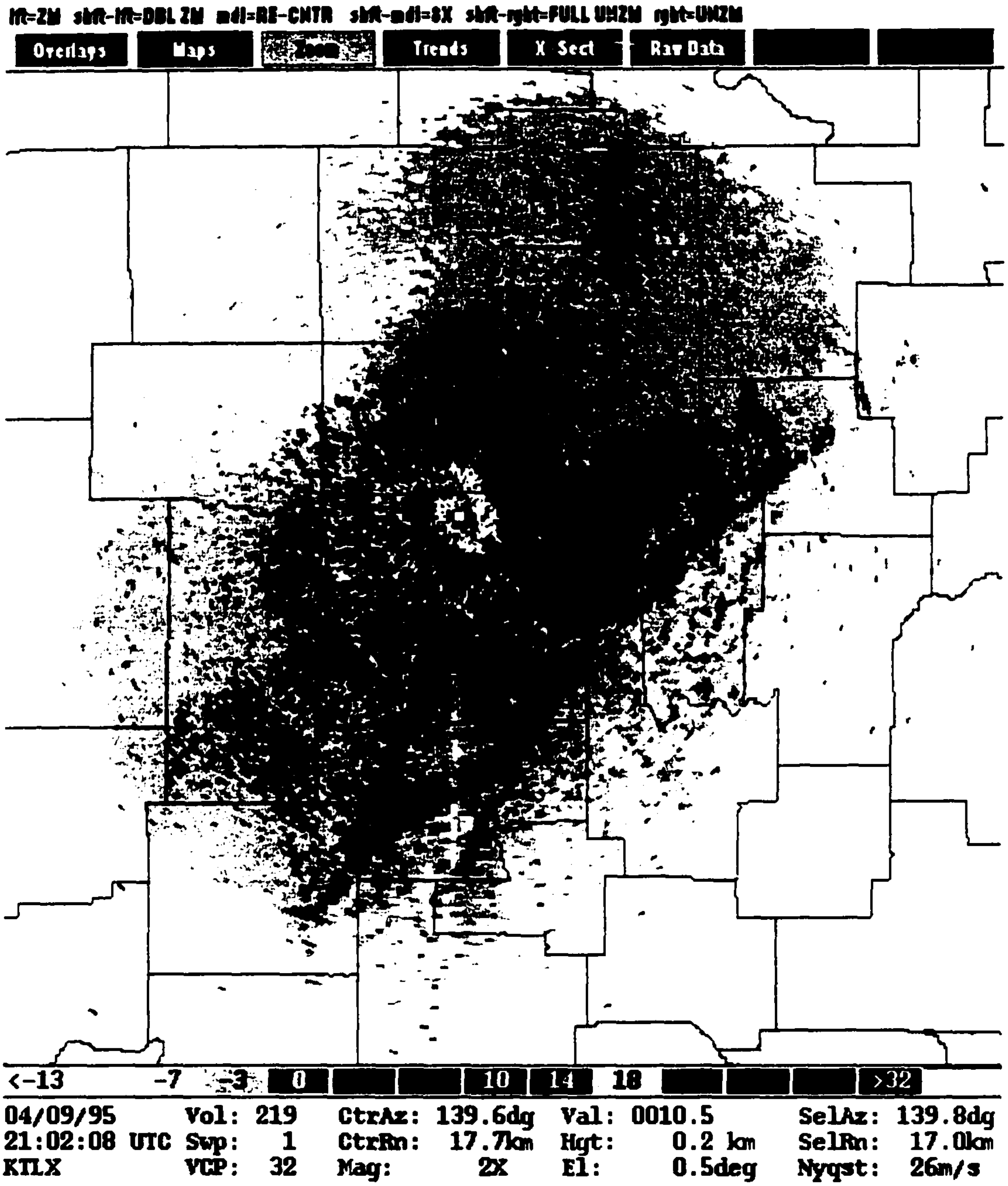

Figure 7.10 Twin Lakes, Oklahoma, radar reflectivity (dBZ). 2102 UTC 9 April 1995.

Figures 7.15 and 7.16 show the surface wind barbs and the v-wind components, respectively after the phase shift has been applied. Although the winds are not in complete agreement with the observed wind directions, the analyzed zero line in the v-wind component more closely matches the observed v-wind component.

Because the phase errors vary in space they can act to change the derivative fields in the vicinity of the front. In this case it appears this is beneficial. In Figure 7.17 the vorticity field, which one might use as a indicator of the frontal boundary location, shows much greater structure than in the original forecast field (Fig. 7.18). Note that the region of maximum vorticity in the phase-corrected case has a very similar position and shape as the non-precipitating radar echoes in the radar display. The divergence field, not shown, has a similar structure, though not quite as conforming. With the addition of an ADAS analysis using the phase-corrected field as a background (Fig 7.20), the vorticity pattern is changed little from the phase-corrected vorticity, suggesting the phase correction performed well in diagnosing this feature.

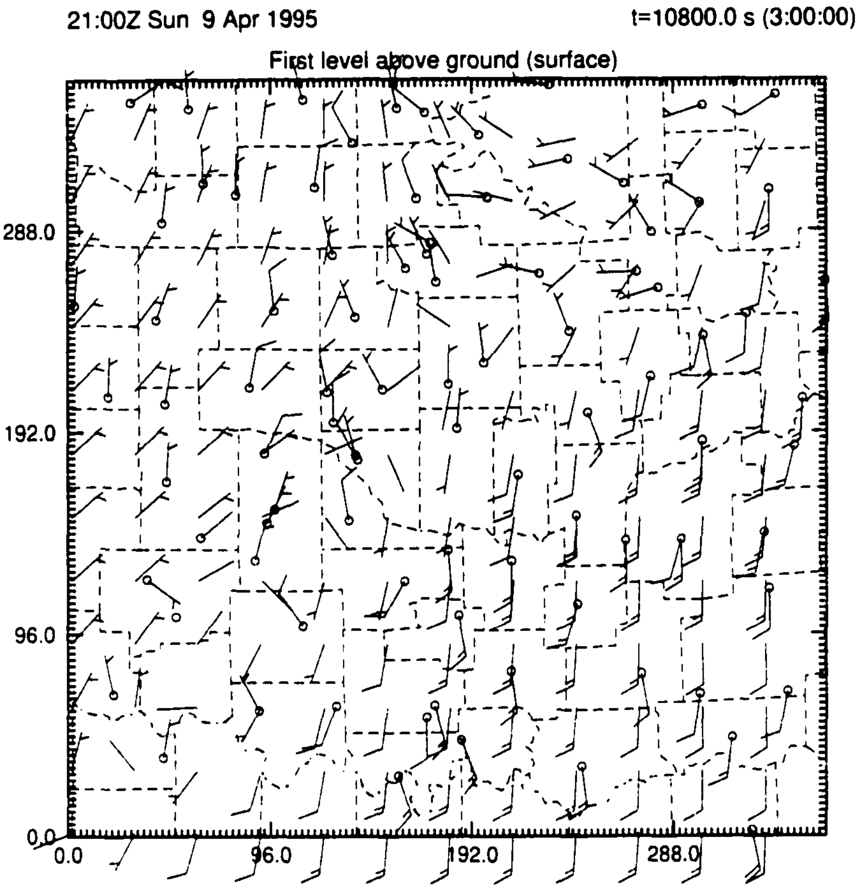

Figure 7.11 Surface winds, 3-hour forecast for 2100 UTC.

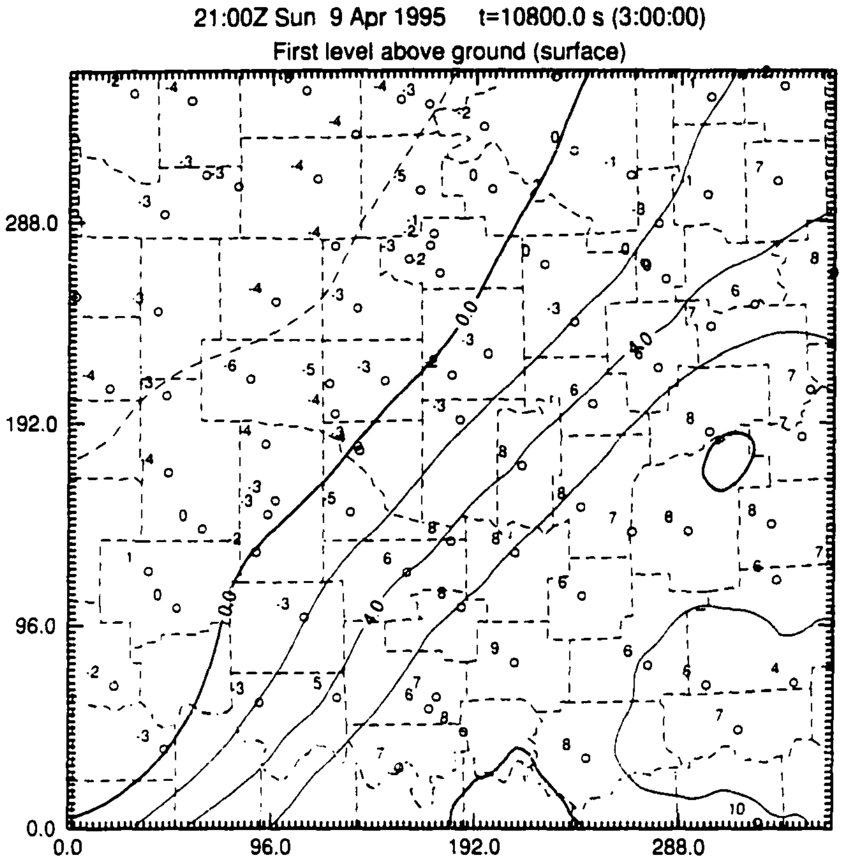

Figure 7.12 Surface v-wind component, 3-hour forecast at 2100 UTC. Contours are of forecast with 2 ms^{-1} increment, circles are observation locations with the observed v-wind component printed (ms^{-1}).

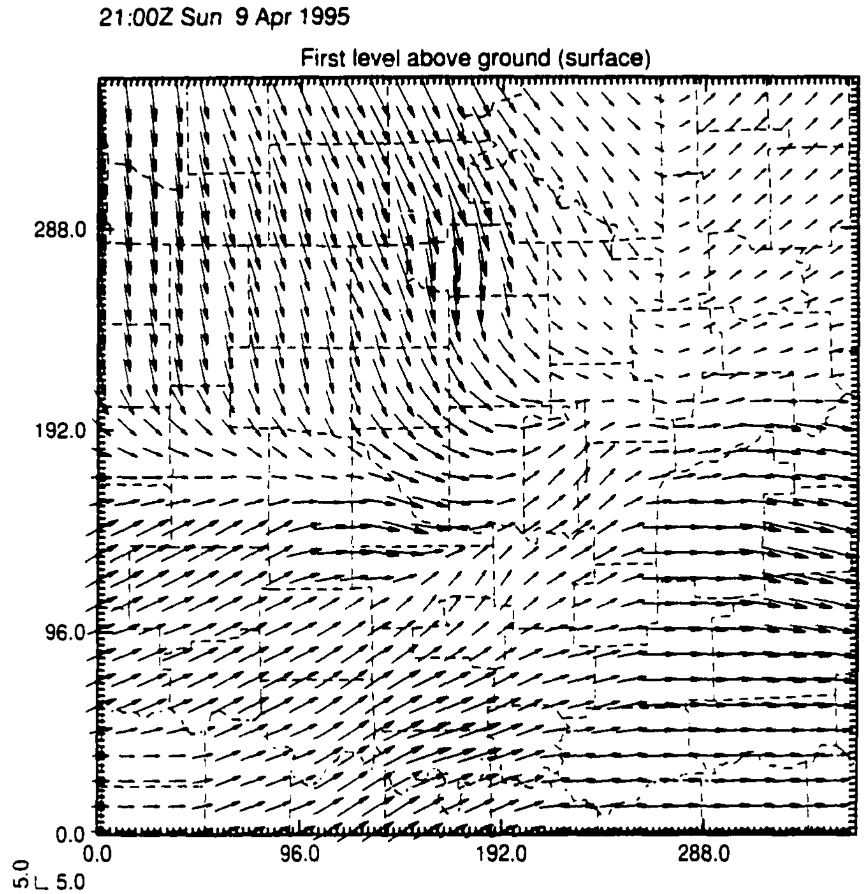

Figure 7.13 Shift vectors at the surface. Vector scale in the left corner is in unit grid lengths (3-km).

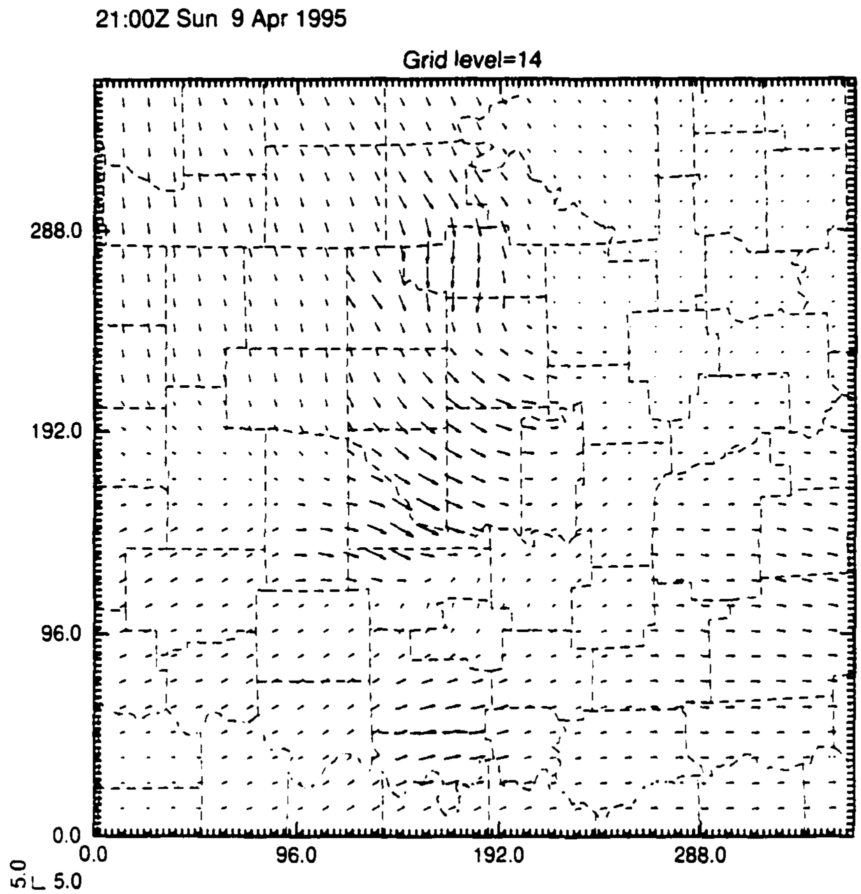

Figure 7.14 Shift vectors at the 14th grid level.

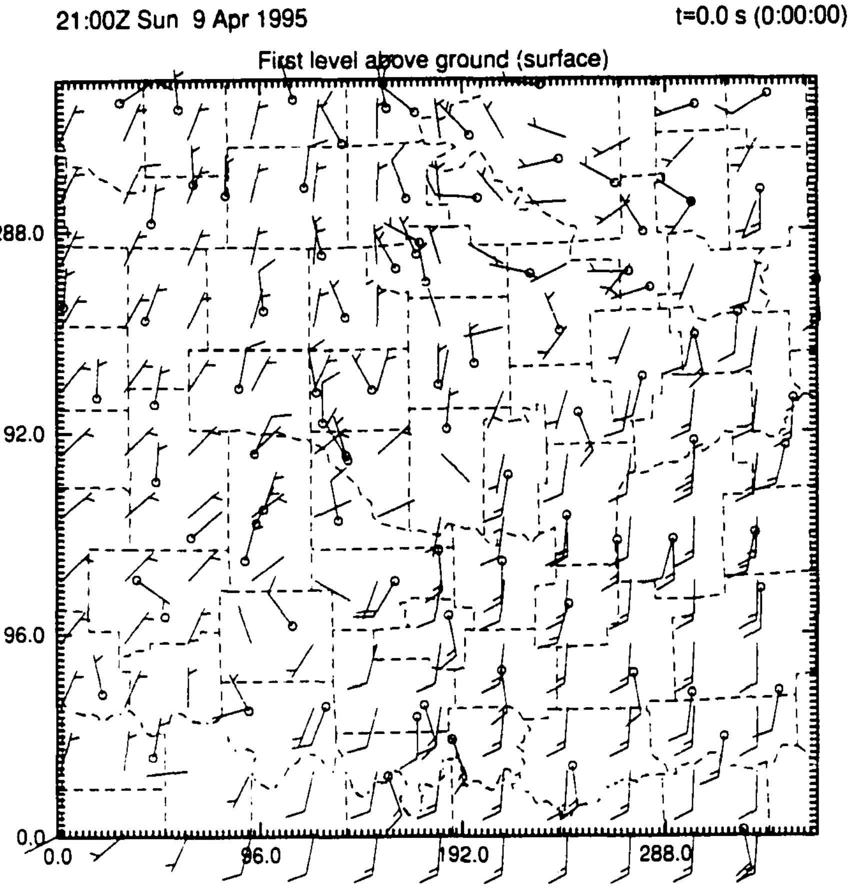

Figure 7.15 Analyzed surface wind (barbs) and observations (barbs with station circles) after phase shift.

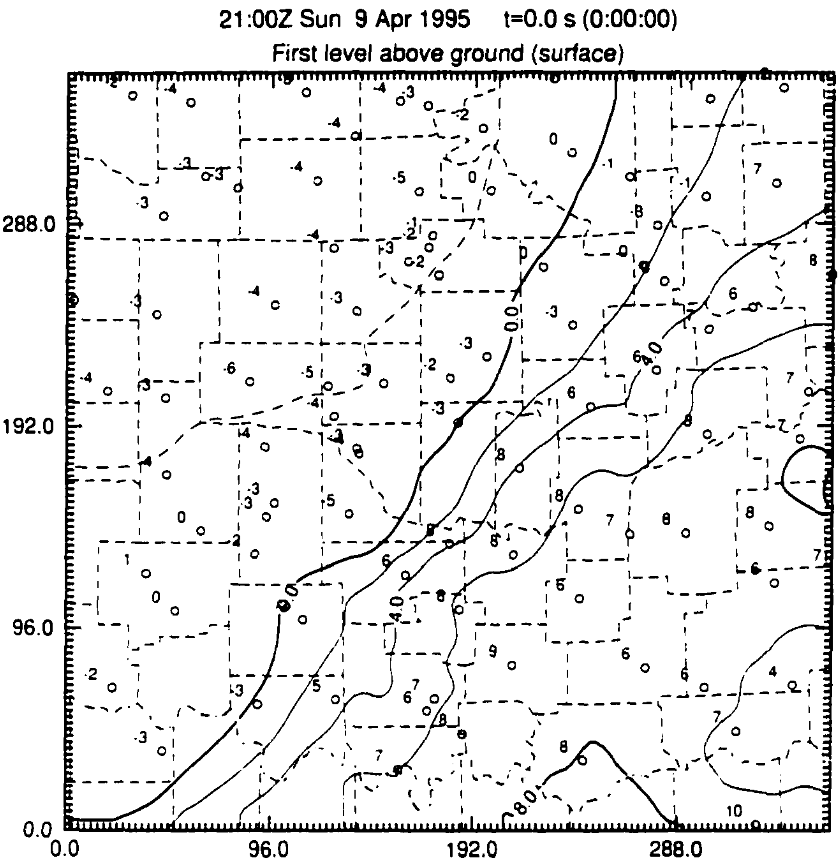

Figure 7.16 Surface v-wind component after phase shift.

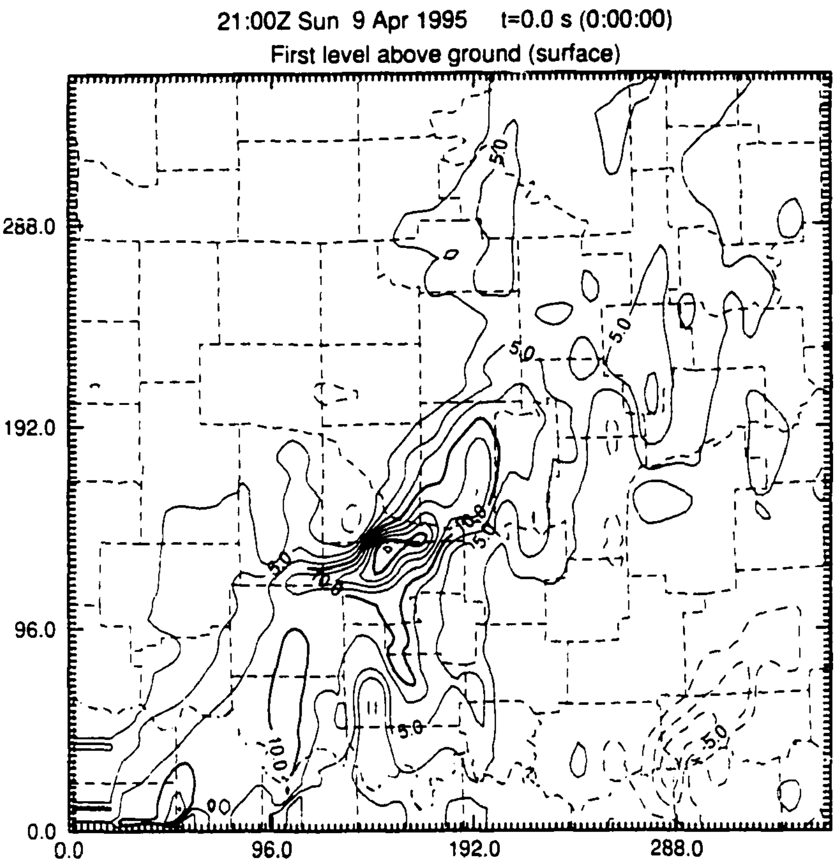

Figure 7.17 Surface vorticity at 2100 UTC after phase shift.

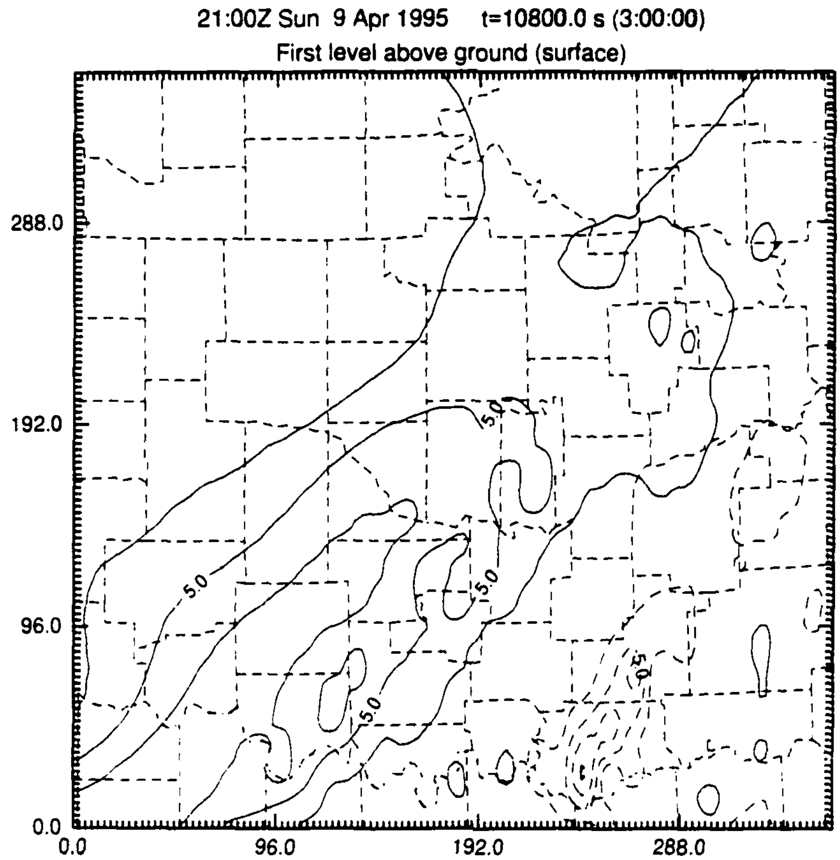

Figure 7.18 Surface vorticity at 2100 UTC before phase correction.

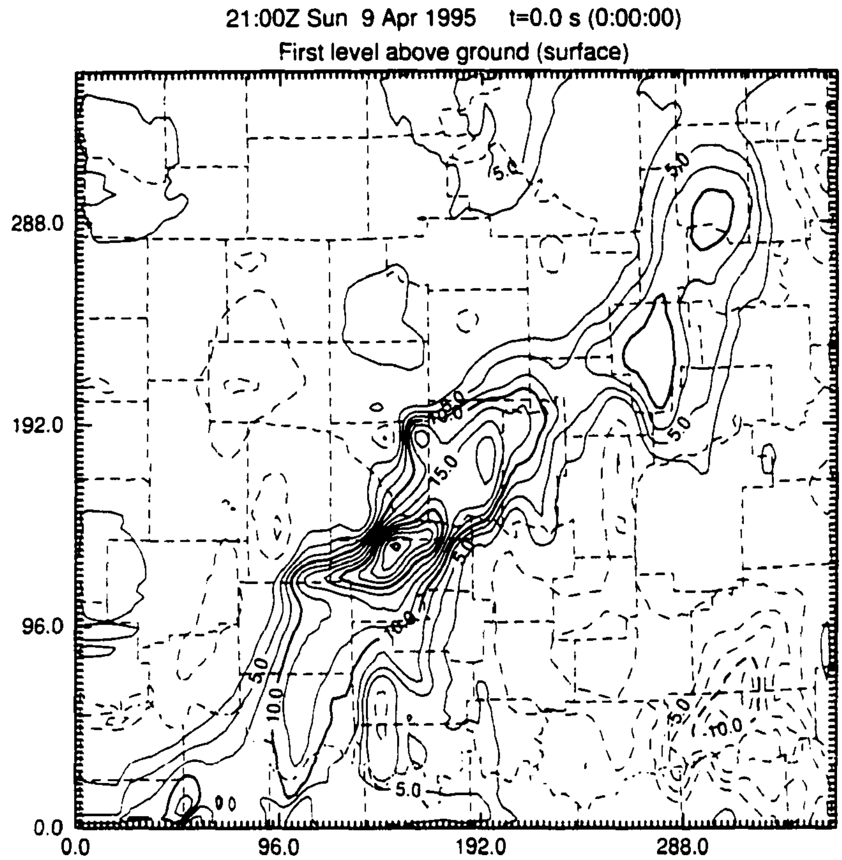

Figure 7.19 Surface vorticity after phase correction and ADAS.

7.3 Analysis Evaluation

Some objective evaluation of the methods can be made by comparing the fit to observations, with the caveat that it can be dangerous to fit observations too closely since they are not perfect and erroneous small scale noise could be introduced.

A score is devised that combines the root-mean-square difference from the observations (RMS errors) for each of the analysis variables plus the Doppler radial velocity. (It is similar to the RMS penalty used in the determination of the phase error, though it does not include reflectivity):

$$S = 10\left(u_{rms}^2 + v_{rms}^2 + 0.01 p_{rms}^2 + \theta_{rms}^2 + vr_{rms}^2\right)^{1/2} \tag{7.1}$$

The purpose of the leading term is to create a score that might have an order of magnitude such that it can be conveniently expressed as an integer. Other constants serve to normalize the magnitudes of the errors among the variables. Since the wind field is important for defining the location of convective initiation, we consider separately the total vector RMS and Doppler radial velocity RMS in forming the scoring table, Table 7.1.

Table 7.1 Difference from observations

	Difference Score	Vector RMS	V_r RMS
12-km fcst only	65	2.8	5.0
Phase Shift	59	2.5	4.6
ADAS	34	1.3	1.2
Shift & ADAS	30	1.2	1.2

Despite the improvement seen in repositioning the wind shift line near the front, the statistics over the entire domain do not show a great improvement for the phase shift. Upon examining the source of the error in the wind field more closely it was found that ADAS is very effective at removing any biases over the domain; there is nearly a 0.5 ms^{-1} bias in each of the wind components in the ARPS forecast field which ADAS removes to less than 0.01 ms^{-1}. Similar reductions in bias due to ADAS are found in other fields, as well. As might be expected, the phase correction is not effective at removing biases, though we have seen a clear improvement in the local structure of the wind. It is apparent that the combination of ADAS and the phase correction does provide the best fit to the data as was anticipated.

7.4 Forecast Results

The ARPS model was run for 3 hours beginning with the analyses created at 2100 UTC. Options for the 3-km ARPS model run are detailed in Appendix B. Examination of the output will focus on comparing the forecast initialized with ADAS versus that initialized with ADAS after phase-correction.

Figure 7.20 shows the forecast v-wind component at the surface and vertically integrated cloud water after one hour, at 2200 UTC. In the upper panel is the forecast initialized with phase correction and ADAS, and the lower panel has the forecast initialized with ADAS only. For ease of noticing differences between the forecasts, a sub-domain of the model is shown.

The forecast including phase correction has a tighter gradient to the wind and cloud fields than the ADAS-only run. Also, the ADAS run has a position error in the zero contour of the v-wind field, most apparent in Pottowatomie County (center of figure) and to its southwest, where the observations show a north wind (negative v) while the ADAS forecast has a south wind.

By 2300 UTC (Figure 7.21), the ADAS-only run shows some increase in the gradient of v-wind component along the front, but the position of the zero contour remains too far to the west.

An hour later, at 0000 UTC (Figure 7.22) the ADAS-only run has developed a stronger gradient in the v-wind, and has a frontal structure, closer to the run including phase correction. The cloud pattern similarly has a reduction in horizontal extent. Neither run produced rainfall in the area which experienced the brief thunderstorm. Although there was a little rainwater produced aloft in a few spots along the front in the run with phase correction, apparently small-scale features that triggered the convection were not detected or developed in the model. It was apparent from the radar display loops (not shown) that there were some weak microscale (1-10 km) waves transverse to the front. Also cumulus clouds developed in the warm sector in the afternoon. The ARPS model was not able to retain clouds in the warm sector, only on the frontal boundary itself. This could be a deficiency of the cloud analysis and or its implementation in the ARPS model -- it is common for clouds to dissipate quickly even when initialized with ADAS. On a positive note, the field translation used for the phase correction did not falsely trigger storms that potentially could have become severe, and would have been contrary to the verification

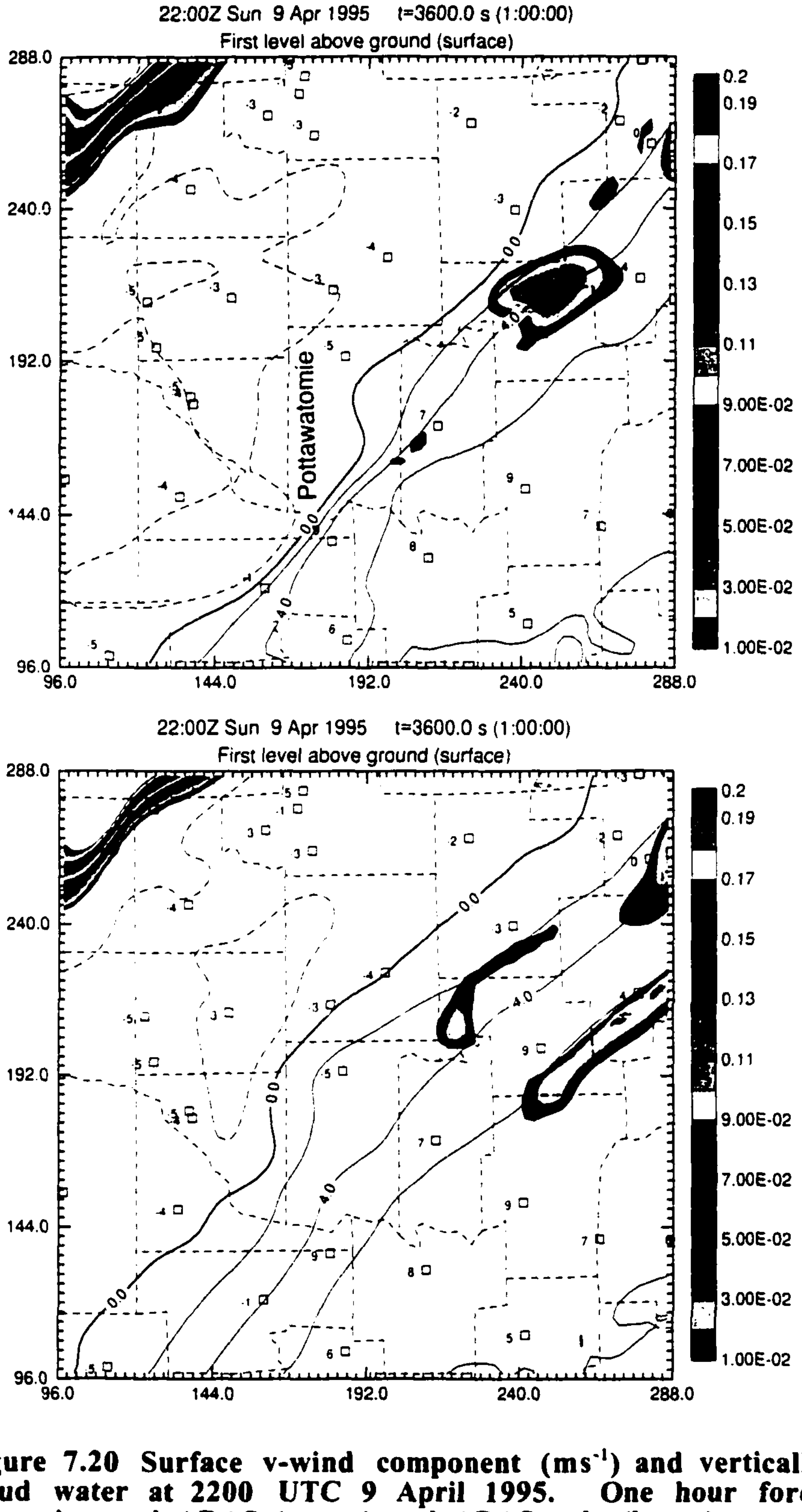

Figure 7.20 Surface v-wind component (ms^{-1}) and vertically integrated cloud water at 2200 UTC 9 April 1995. One hour forecast. Phase correction and ADAS (upper) and ADAS only (lower).

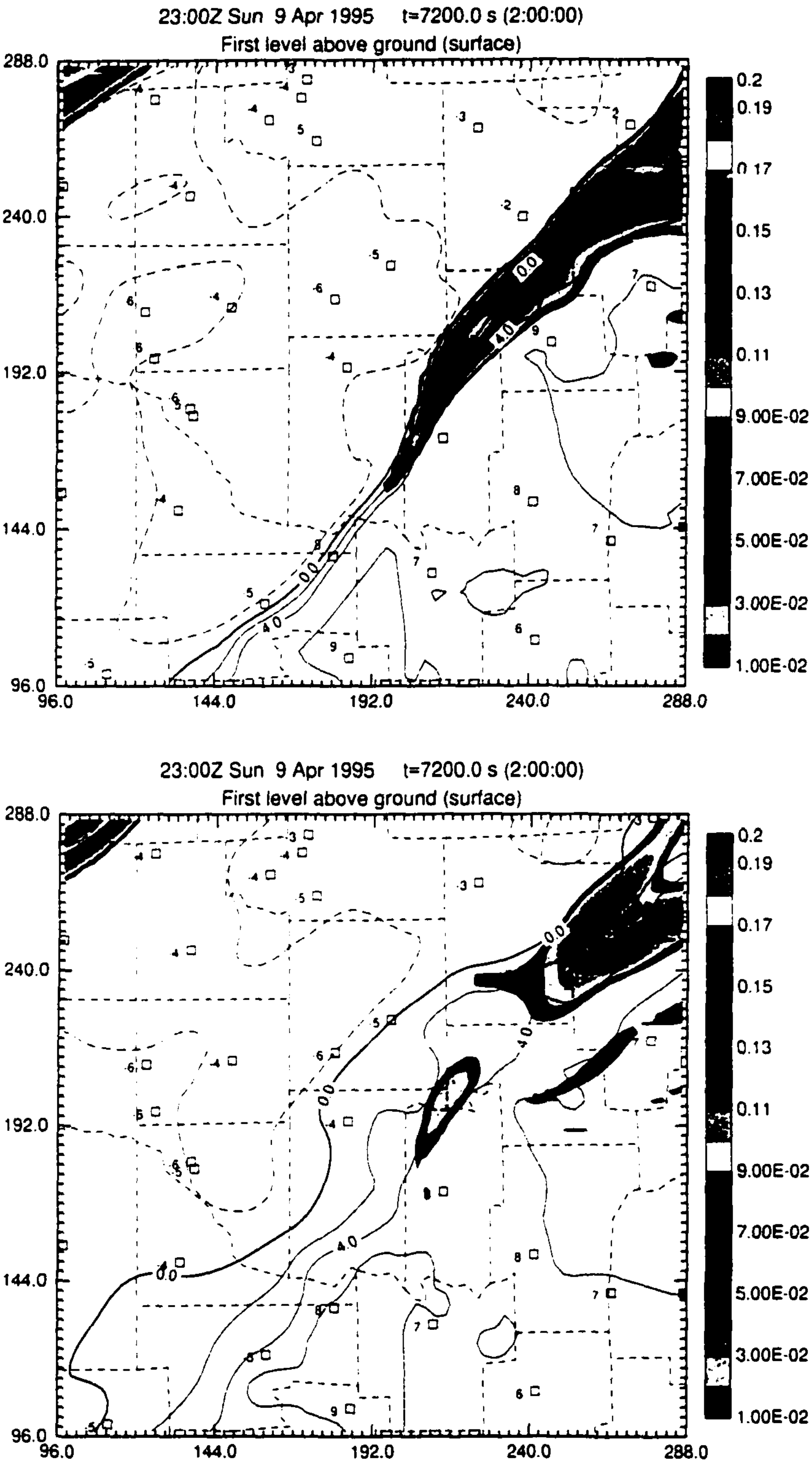

Figure 7.21 Surface v-wind component (ms^{-1}) and vertically integrated cloud water at 2300 UTC 9 April 1995. Two hour forecast. Phase correction and ADAS (upper) and ADAS only (lower).

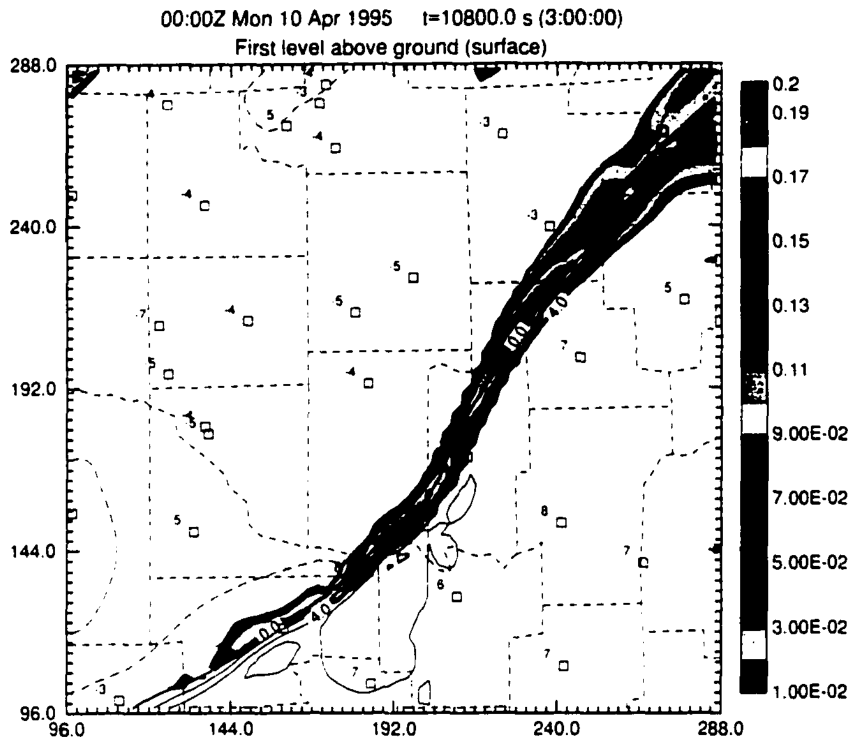

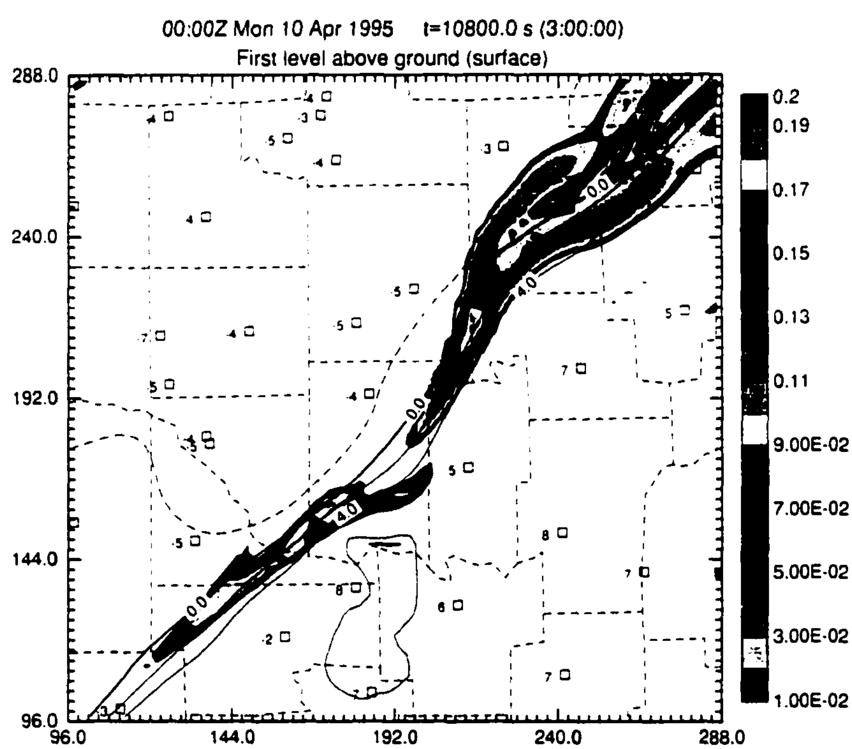

Figure 7.22 Surface v-wind component (ms^{-1}) and vertically integrated cloud water at 0000 UTC 10 April 1995. Three hour forecast. Phase correction and ADAS (upper) and ADAS only (lower).

Chapter 8 Front-Dryline Case

8.1 June 8, 1995 Synoptic Setting

The case of June 8, 1995, will used to examine the ability of the assimilation techniques to correct errors in forecasts of storms during the time of first convective development on a day of severe weather. This day was a major case for the Verification of Onset of Rotation in Tornadoes Experiment (VORTEX) as several damaging tornadoes were produced by storms in the eastern Texas Panhandle. Significant tornadoes occurred at Pampa (rated F4 on Fujita damage scale) (NOAA, 1995), south of McLean (F2), Kellerville (F4) and near Allison (F4), Texas, that afternoon. This section details the synoptic and mesoscale setting for this severe weather outbreak and assimilation study case.

At 1200 UTC on June 8, the surface map in the Southern Plains region (Figure 8.1) featured a very slow-moving cold front from east of Wichita, Kansas. extending into the northern Texas Panhandle and continuing into the foothills of the Rockies in northeastern New Mexico. There was convection (not shown) in southwestern Kansas, south and east of Dodge City, Kansas, along the front. This activity was continuing from the night before and propagating eastward along the boundary. Rain-cooled outflow from the convection served to reinforce the frontal boundary and aid in its southward propagation.

There was a dryline in the western Texas Panhandle, with the dewpoint temperature at Amarillo (AMA) of 18 (C) contrasting with a dewpoint of 3 (C) at Clovis, New Mexico (CVS). As is typical for this early in the day, winds behind the dryline were weak. Some dry air had also intruded into the northern Texas Panhandle, just south of

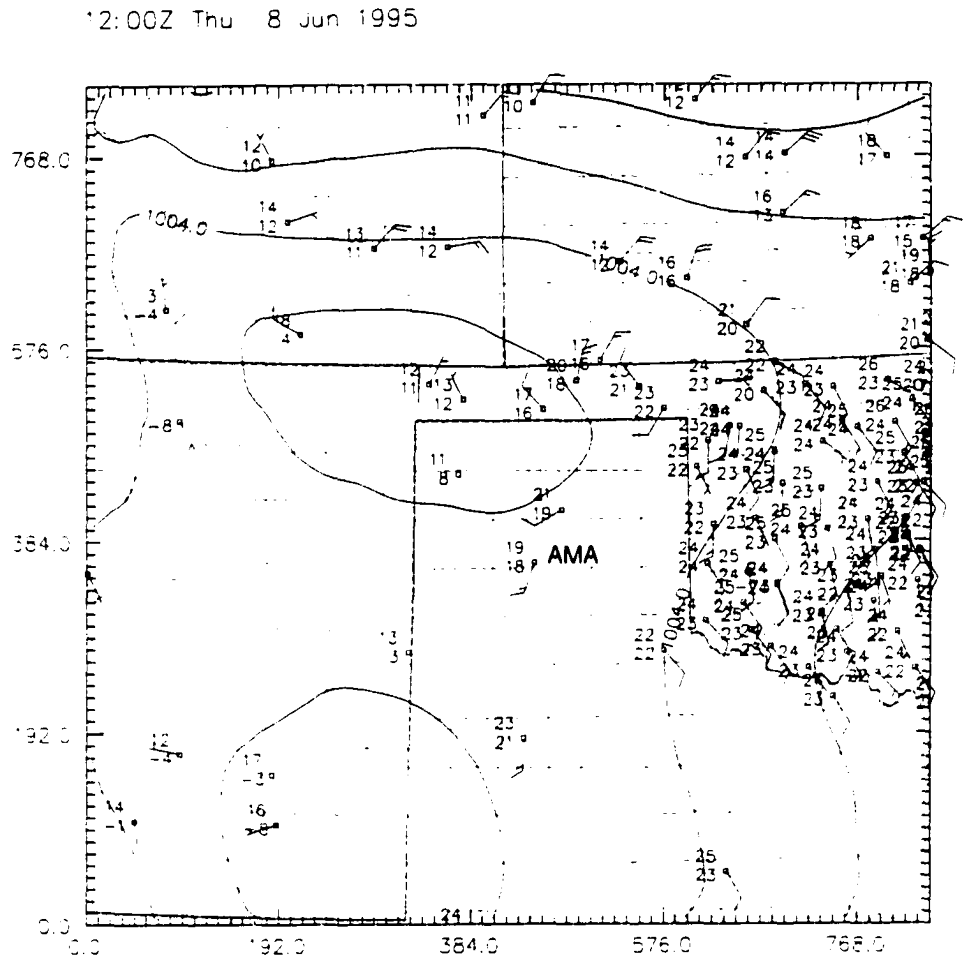

Figure 8.1 Surface weather for 1200 UTC, 8 June 1995. Station model and sea level pressure analysis (contour interval 2 hPa) from the RUC model. Station model includes temperature (upper, degrees C) and dew-point (lower, degrees C), wind barbs are in ms^{-1} with a full barb representing 5 ms^{-1} and half barb 2.5 ms^{-1}.

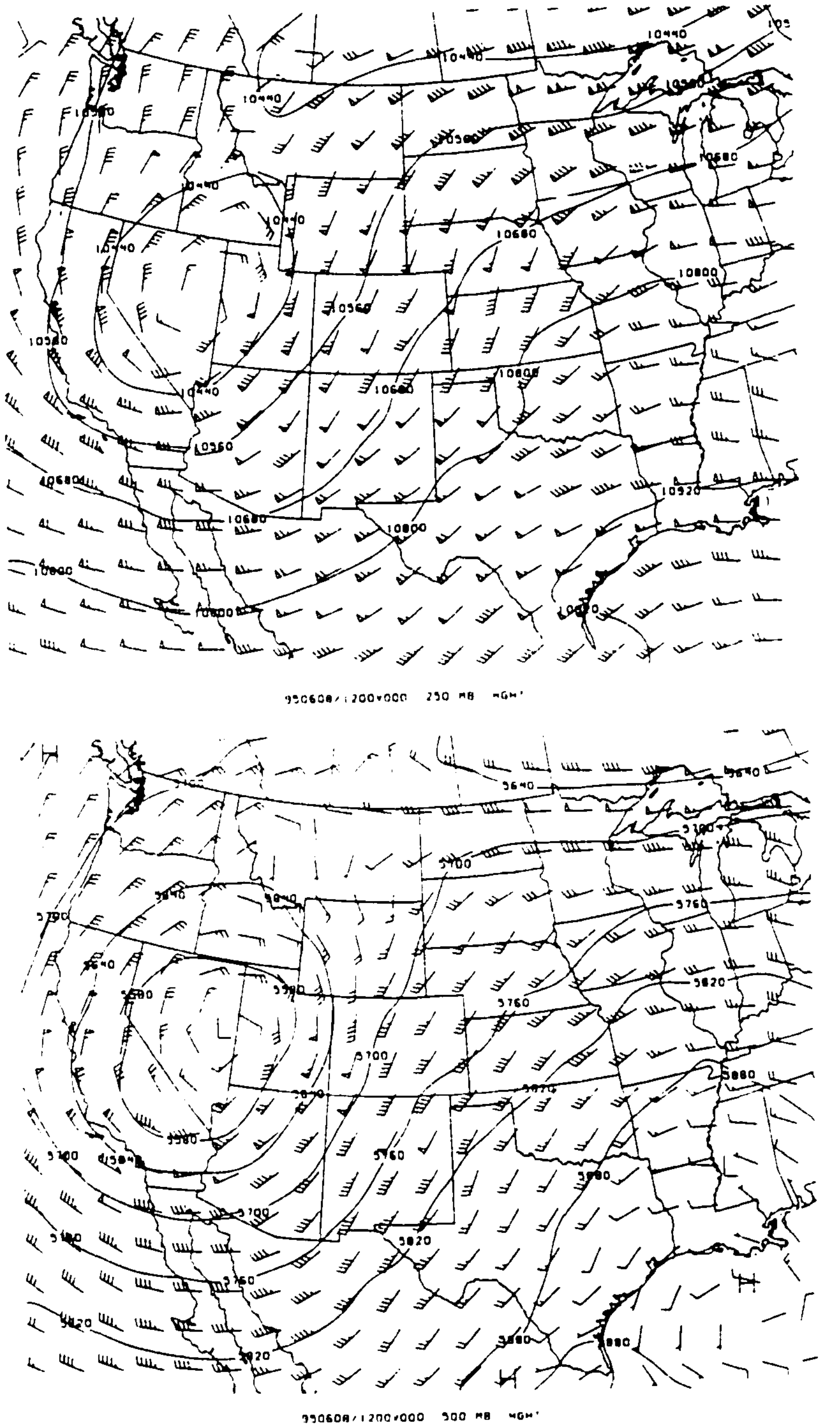

Figure 8.2 Upper level RUC analyses for 1200 UTC, 8 June 1995. Heights in meters, wind barbs in knots. a) 250 hPa, b) 500 hPa.

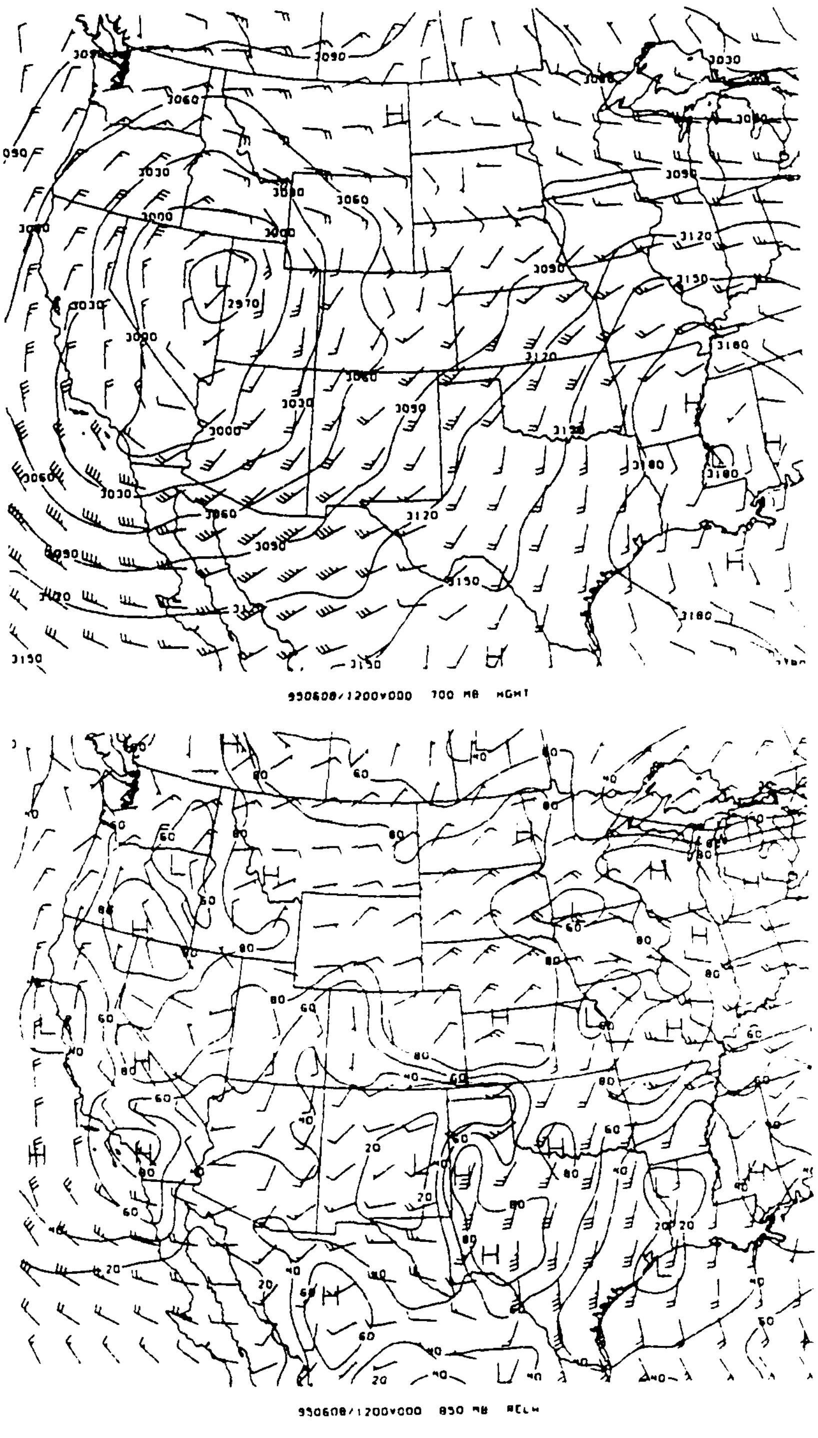

Figure 8.8.3 Analyses for 1200 UTC, 8 June 1995. a) 700 hPa, geopotential heights in meters and wind barbs in knots. b) 850 hPa, relative humidity and wind barbs in knots.

the front, where dewpoints in the upper teens were not quite as high as those to the east and south, which were in the lower 20s. A trough of low pressure was coincident with the stationary front, but there was little indication of the dryline in the sea-level pressure field.

Aloft, winds at 500 hPa (Figure 8.2b) were from the southwest on the southeastern periphery of a closed low centered in the Great Basin. Winds at 500 hPa were about 20 ms^{-1} from the southwest over the region of interest. There were no significant shortwaves evident in the 500 hPa height analysis east of the main low. Around the tropopause level (250 hPa, Fig 8.2a), winds were also from the southwest at 25 ms^{-1}, with slightly stronger winds coming around the base of the trough to the west of the Texas Panhandle. At 700 hPa (Fig 8.3a), winds were southwest at 15 ms^{-1}, though the winds upstream, in southeastern New Mexico, were somewhat weaker, less than 10 ms^{-1}. Wind speeds increased again further west, in northern Mexico, where they were 20 ms^{-1}, and more westerly rather than southwesterly.

With southeasterly surface winds in the moist air of western Texas and Oklahoma, the wind shear was expected to be sufficient to support supercell thunderstorms. Forecasters with the VORTEX project expected the "triple-point", marking the intersection of the dryline and frontal boundary, to provide sufficient low-level convergence to initiate convection and realize significant CAPE. Storms were expected to form in the northeastern Texas Panhandle and become severe in northwestern or northern Oklahoma as the storms progressed eastward along the frontal boundary during the afternoon. Research data-collection teams were dispatched to northwestern Oklahoma.

At 1800 UTC, the surface weather map (Fig. 8.4) showed little change in the position of the important features compared to 1200 UTC. There was some progression of the front southward in northern Oklahoma in response to the convective cells continuing eastward in southern Kansas. In the Oklahoma panhandle, north of the front, winds at some locations become more easterly than northerly and the westerly component of the winds behind the dryline at both Borger and Amarillo, Texas were actually weaker than at 1200 UTC.

Special soundings were taken at this time to assess the extent of the convective instability and strength of the capping inversion. The sounding at Amarillo (Fig 8.4) shows a profile typical of that behind a weak dryline. Despite the relatively dry air it still showed CAPE of 2015 Jkg^{-1}, though there was a capping inversion at 750 hPa for a surface parcel. Note that the winds at 800-700 hPa, though strong (15 ms-1), did not have much of a westerly component. Vertical mixing of this air to the surface would not increase the westerly momentum to create a significant advancement of the dryline to the east.

A sounding taken by a mobile research crew in northwestern Oklahoma, at Seiling (marked SLG on Fig 8.5), is shown in Figure 8.6. Due to the very moist air in this region (dewpoint of 23 C, water vapor mixing ratio of 14 gkg^{-1}), this sounding has an extremely high CAPE of nearly 4000 Jkg^{-1} and the capping inversion at 750 hPa is not an impediment for an unmixed parcel lifted from the surface. However, due to the slight superadiabatic lapse rate just above the surface, actual buoyant plumes in that area would likely be better mixed and thus the cap would prevent convection from occurring. Nonetheless, only slight forcing would be needed to trigger the convective instability.

At 1908 UTC the first convective echoes appeared on the Amarillo radar. The first cell was along the front in the northern Texas Panhandle, near Perryton, Texas. This cell quickly increased in intensity, and moved northward with time, into the Oklahoma panhandle. The cell developed a low-level circulation and produced hail and a brief tornado, but as it moved further into the cool air north of the frontal boundary, its intensity eventually decreased.

At 2008 UTC new cells formed further south; one was near the triple point, near Stinnett, Texas but two others developed in the warm air east of Amarillo, near Pampa. This was to be the area of the most severe storms of the day, the ones that produced the large hail and damaging tornadoes. More details of the initiation and progression of cells in this area will be discussed with the model results.

By 0000 UTC on June 9, a cluster of intense thunderstorms covered the eastern Texas panhandle north of Interstate-40 and gradually moved eastward into western Oklahoma, continuing to produce severe weather into the evening hours. The surface map for this time is shown in Fig. 8.7.

Figures 8.8 and 8.9 show the upper-level analyses for 0000 UTC. Although a short-wave appears at 500 hPa in southwest Kansas, this could be due to latent heating from the cluster of thunderstorms, rather than a cause of lifting for their initiation. The zone of maximum winds at 250 hPa lies well to the northwest of the Texas Panhandle. Although difluent flow in the Panhandle was favorable for supporting storms, it does not appear that a significant jet streak affected the region. The flow at 700 hPa remained southwesterly, backing slightly with time, thus there was not a significant eastward push on the dryline.

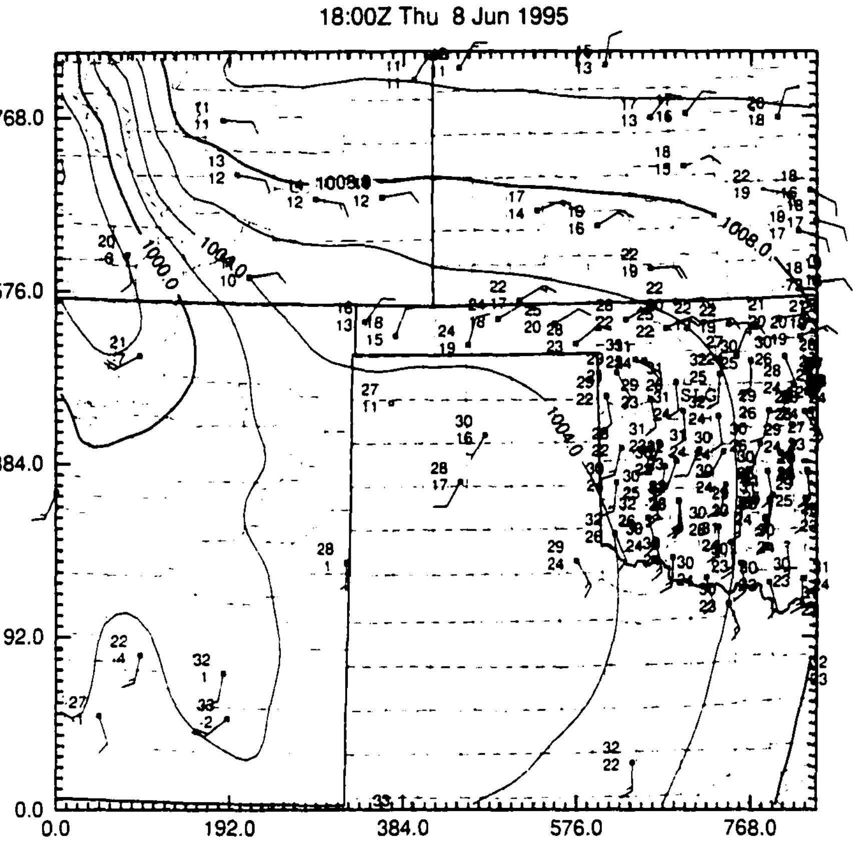

Figure 8.4 Station model and sea-level pressure for 1800 UTC 8 June 1995. Variables as in Fig. 8.1.

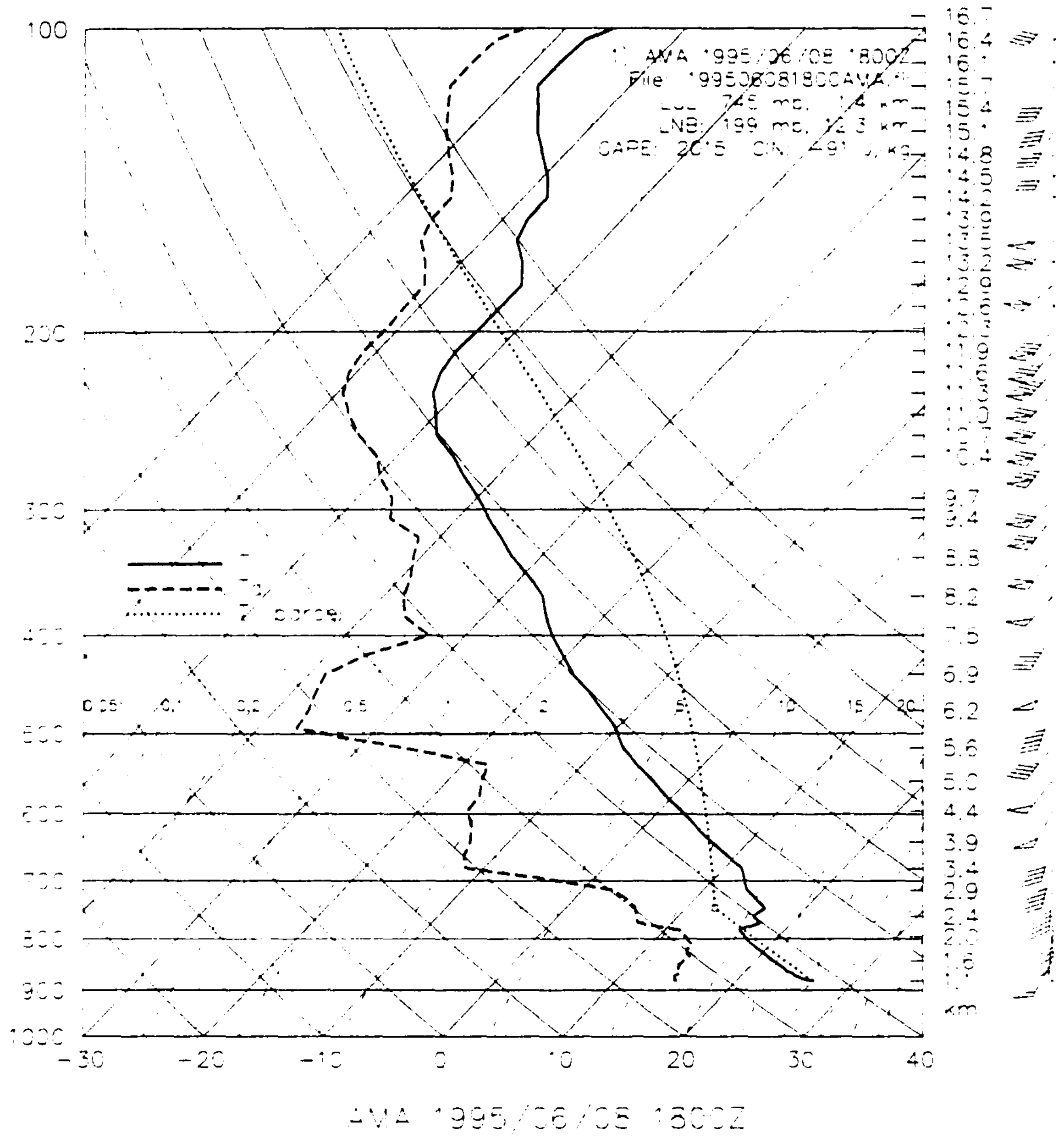

Figure 8.5 Skew-T plot of sounding taken at Amarillo, Texas at 1800 UTC, 8 June 1995. Temperature (C) and dew-point (C) with parcel trajectory for unmixed surface parcel.

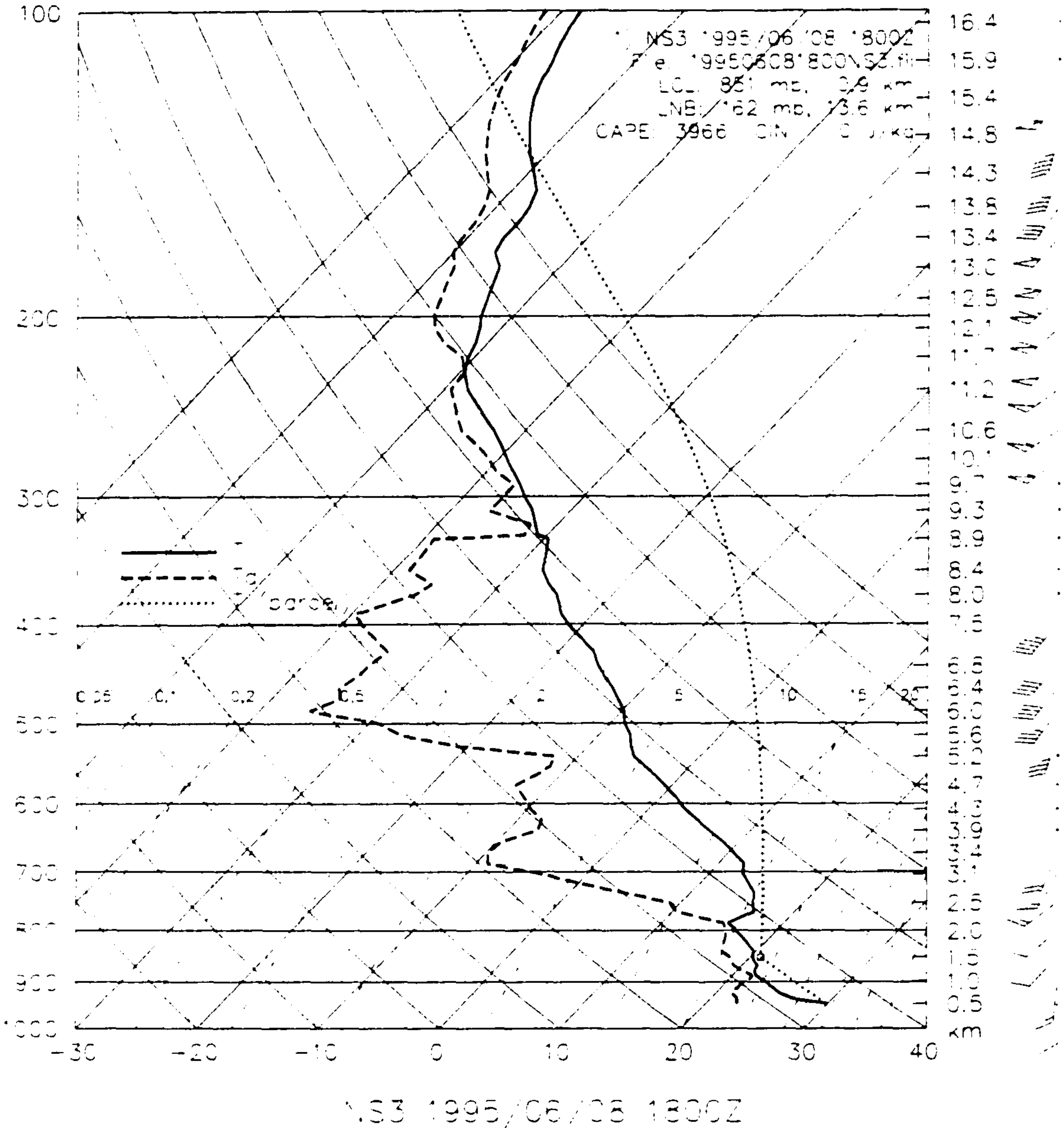

Figure 8.6 Skew-T plot of sounding taken by NSSL mobile crew near Seiling, Oklahoma at 1800 UTC 8 June 1995. Temperature (C) and dew-point (C) with parcel trajectory for unmixed surface parcel.

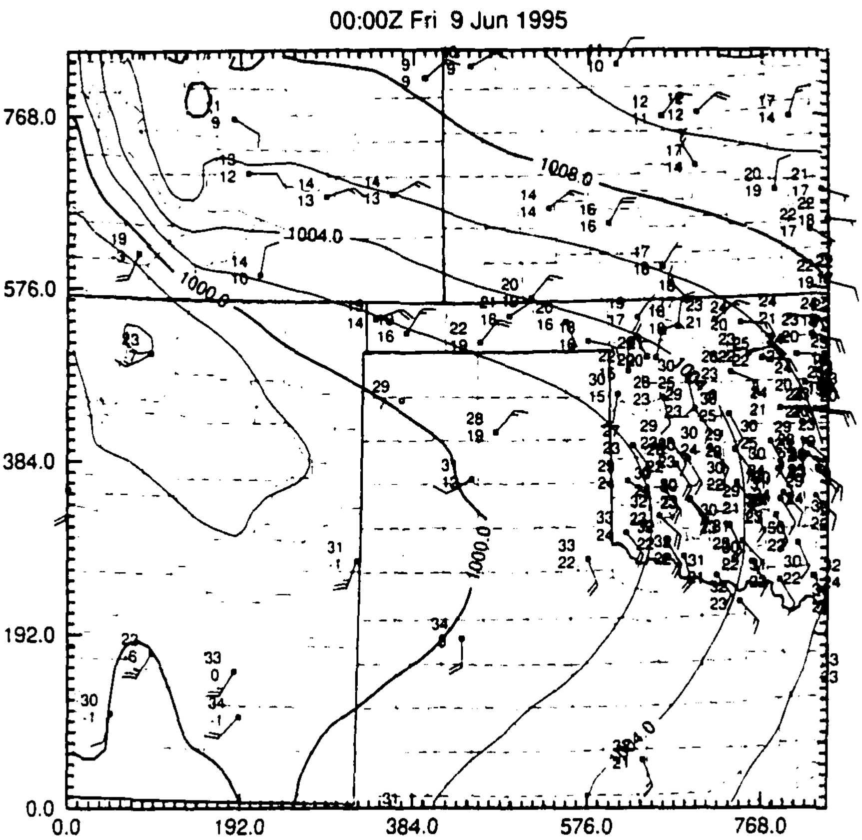

Figure 8.7 Station model and sea level pressure, 0000 UTC 8 June 1995. Variables as in Figure 6.2.

In summary, the synoptic background was favorable for storms in terms of providing significant vertical wind shear and low-level winds favorable for transporting the unstable air into the region. The quasi-stationary frontal boundary and the dryline provided convergent low-level flow to initiate convection, but the capping inversion was weak enough that cells also formed just ahead of those boundaries. With the apparent lack of a significant shortwave aloft, the motion of cells and initiation of cells was then mostly affected by dryline dynamics (mixing), interaction between cells and their own propagation rather than following the progression of some synoptic scale forcing feature. Thus, the location of the first few cells and the proper spacing of the

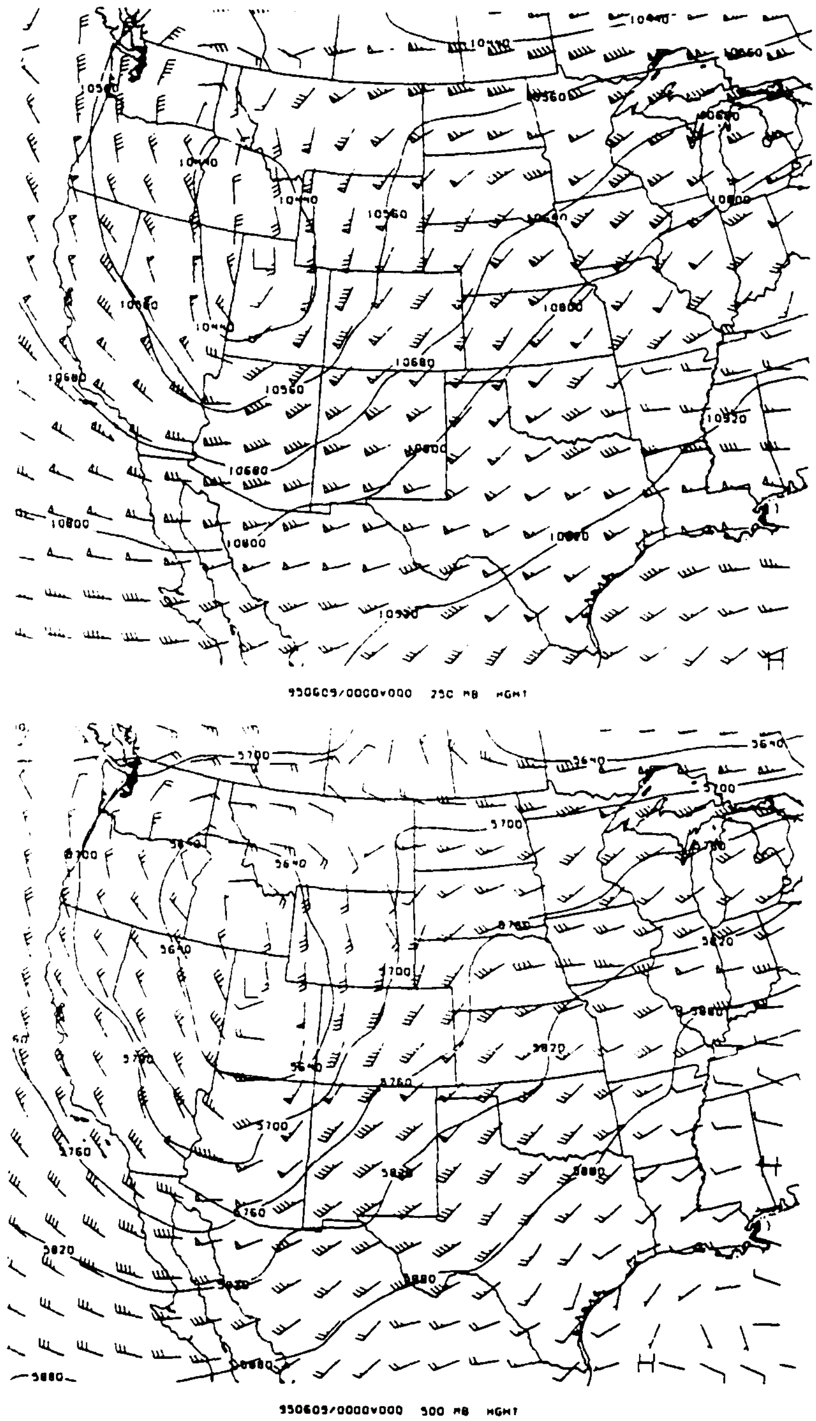

Figure 8.8 Upper level RUC analyses for 0000 UTC, 9 June 1995. Heights in meters, wind barbs in knots. a) 250 hPa, b) 500 hPa.

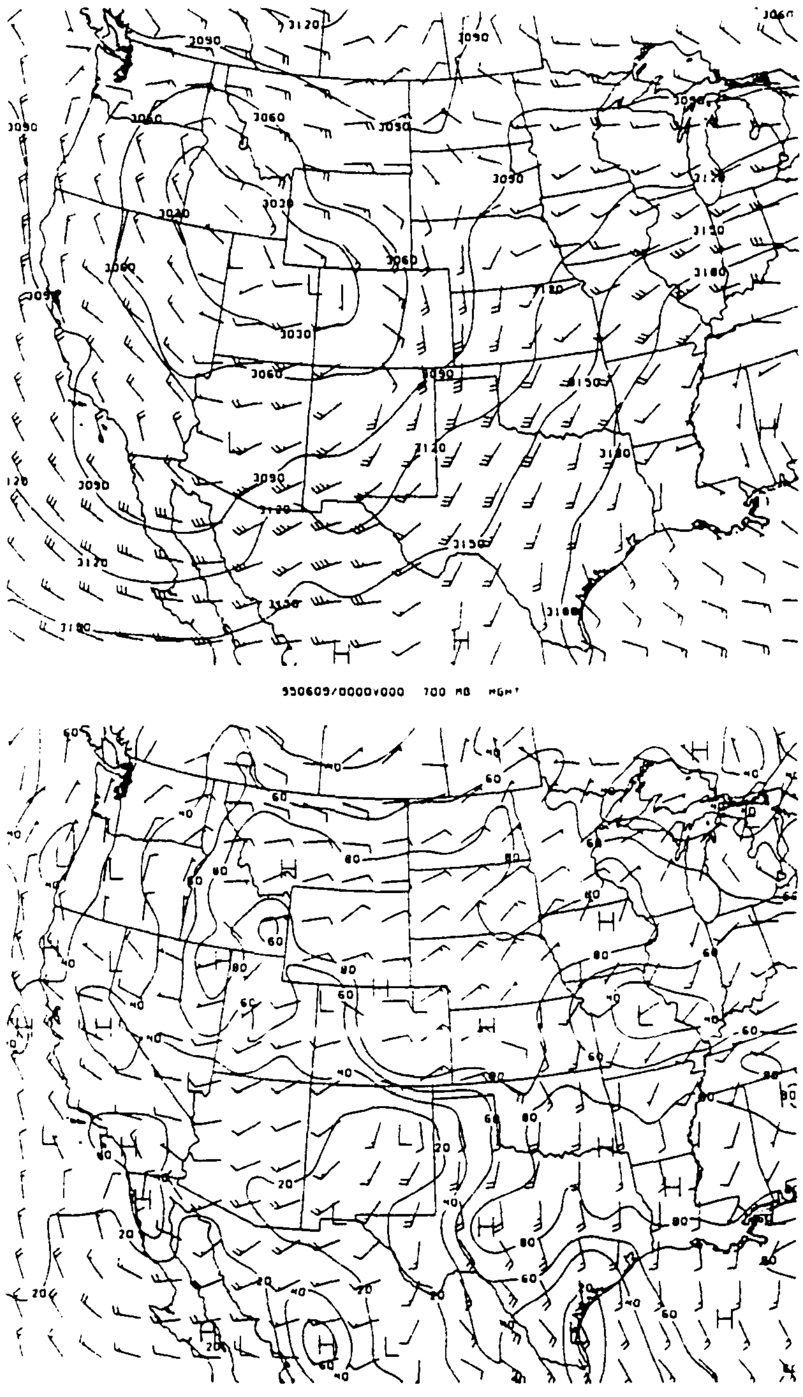

Figure 8.9 RUC analyses for 0000 UTC, 9 June 1995. a) 700 hPa, geopotential heights in meters and wind barbs in knots. b) 850 hPa, relative humidity and wind barbs in knots.

early cells is thought to be important for dictating the convective development during the afternoon, and phase correction would be useful and its effect more likely to persist.

8.2 12-km Mesoscale Spin-up Simulation

Although we seek to make a storm-scale simulation, the storm-scale model run will require time-dependent lateral boundary conditions and it is desirable to have an initial field that contains a representation of the mesoscale. It must be higher resolution than the 60-km RUC external model. Therefore, a 12-km mesoscale spin-up simulation is made using ARPS. Figure 8.10 shows the domain of the 12-km run with the 3-km domain imbedded. A schematic of the assimilation procedure is shown in Figure 8.11, and is detailed in this section.

Since convection began in the early afternoon, a mid-morning initialization is chosen for the spin-up. A 9-hour 12-km forecast run in the region of interest beginning at 1500 UTC is made using ARPS. The 1200 UTC run of the RUC is used to begin the process and for boundary conditions (The RUC forecast initialized at 1500 UTC was not available in the archived data for this day, and the 1200 UTC run has the advantage of having 3 hours of spin up time by 1500). The RUC forecast fields are interpolated to the ARPS model grid and increments are calculated using ADAS. Surface data used include the surface airways observations, the Oklahoma Mesonet, the Colorado Agricultural Meteorological Network and the ARM (Department of Energy Atmospheric Radiation Measurement) surface network. Aloft, data from the vertical wind profilers are used. Radar data are used in the ADAS cloud algorithm, but the raw velocity data were not used at this scale. Satellite infrared (IR) and visible data from the geostationary satellite GOES-8 are used in the cloud analysis processing.

The analysis increments are introduced (see Chapter 3, Section 3.7) to the model using a constant time weighting over a ten minute window. The data analysis and analysis increment updating are repeated every hour for 1600, 1700 and 1800 UTC, with the increments calculated at 10 minutes before the hour (roughly corresponding to

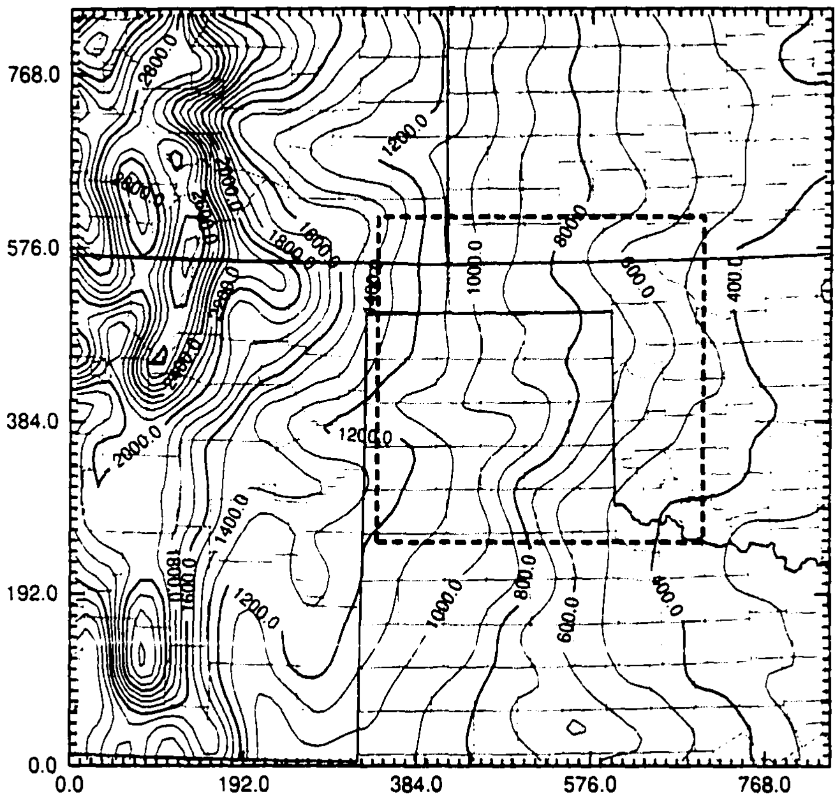

Figure 8.10 Domains for the 8 June 1995 simulations. Entire region shown is the domain for the 12-km runs. Dashed box is the 3-km nested domain. Model terrain in meters above sea level.

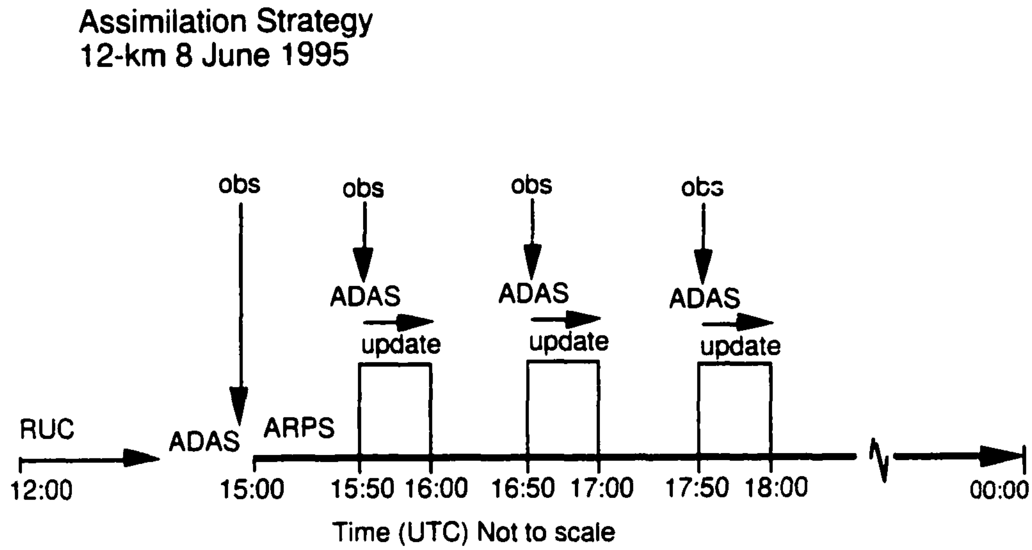

Figure 8.11 Schematic of data assimilation process used for 8 June 1995 demonstration.

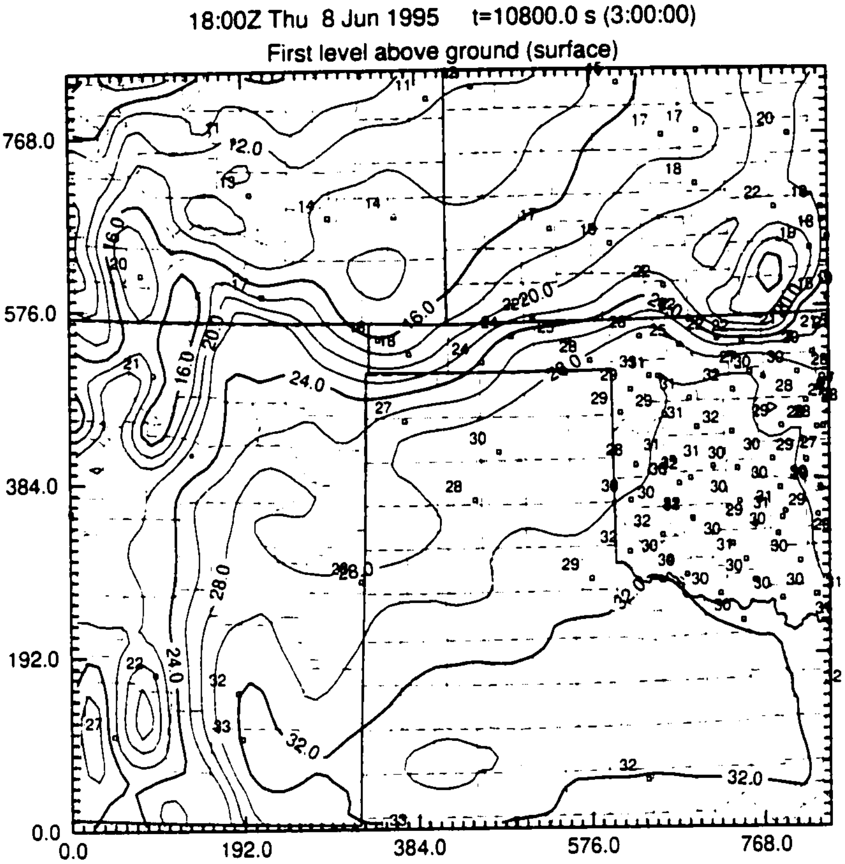

Figure 8.12 12-km assimilated state at 1800 UTC, 8 June 1995. Surface temperature (C).

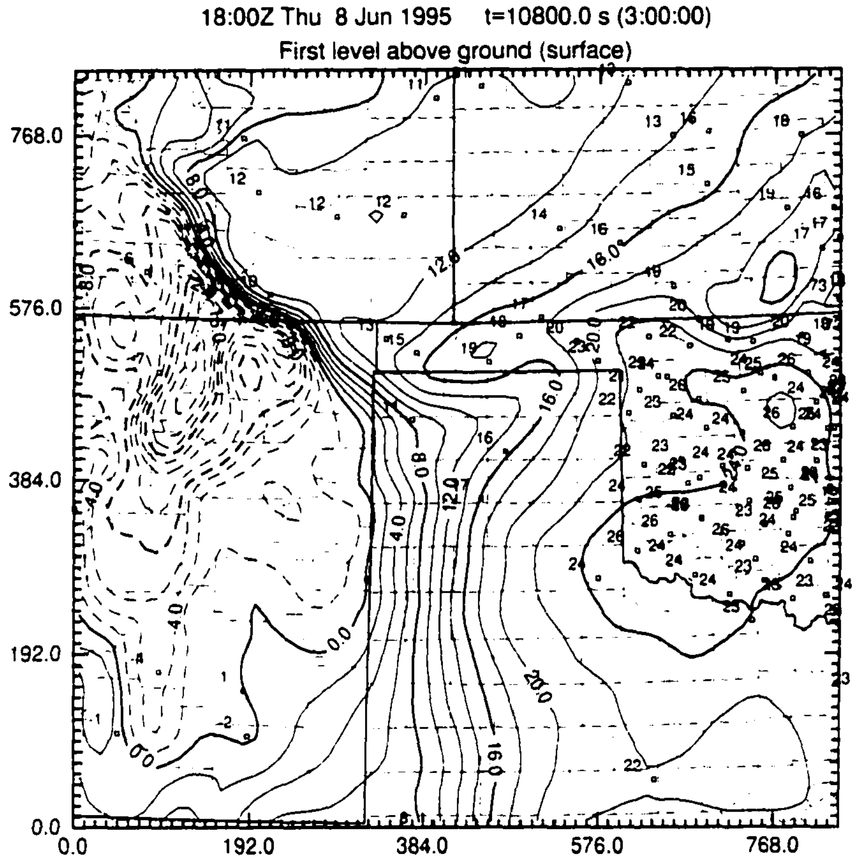

Figure 8.13 12-km assimilated state at 1800 UTC, 8 June 1995. Dew-point temperature (C).

the time of the surface observations) and applied during the 10 minutes preceding the top of each hour. There were some special soundings taken at 1800 UTC for the VORTEX project that were included in the analysis for that hour.

The forward model used full ice microphysics and did not use a parameterization for cumulus convection. A complete listing of the ARPS input parameters for the 12-km model is included in Appendix A, Tables A.1, A.2 and A.3.

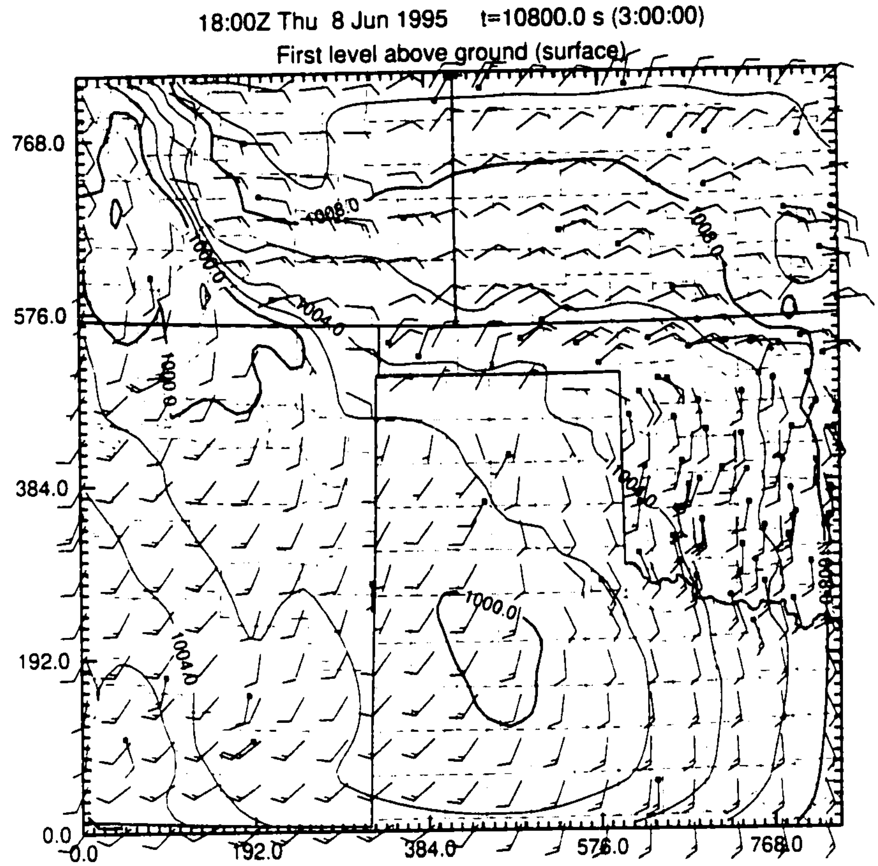

Figure 8.14 12-km assimilated state at 1800 UTC, 8 June 1995. Mean sea level pressure (hPa) and wind barbs (ms^{-1}). Full barb is 5 ms^{-1}.

Figures 8.12, 8.13 and 8.14 show the ARPS model assimilated state at 1800 UTC, plotted with observations at the same time, for surface temperature, dew-point temperature and winds and pressure, respectively. Note that the assimilation system has developed tight gradients along the front in the Oklahoma panhandle and in the dew point fields in West Texas and southern Colorado. Although this model run did not use a convection parameterization nor have the grid spacing to fully resolve a thunderstorm, it was able to capture the cold air pocket, divergent winds and pressure anomaly (not shown) of the thunderstorm outflow in northwestern Oklahoma.

A 3-km initial condition is interpolated from the 3-hr 12-km forecast valid at 1800 UTC. Also the 12-km run is continued until 0000 UTC 9 June in order to generate boundary conditions for the 3-km run. The boundary conditions are thus used in a one-way nesting arrangement. No additional data are provided to the 12-km run. The 3-km model is run from 1800 to 0000 UTC. Tables B.1, B.2 and B.3 in Appendix B detail the ARPS option settings for the 3-km ARPS runs.

8.3 3-km Storm-scale Simulations

Experiments are performed on the 3-km run to test the effect of introducing additional data at the early growth stage of the primary area of convection for the test case. Specifically, the phase correction and ADAS are used with radar and surface data applied to the 3-km forecast initialized at 1800 UTC.

The storms in the area of interest were triggered at about 2000 UTC, with the exception of a storm that formed in the Oklahoma panhandle about an hour earlier. The storms grew quite rapidly, and by 2010 UTC there was sufficient radar reflectivity observed to define the principal initial cells in the northeast Texas panhandle. Figure 8.15 is the Amarillo radar reflectivity for 2008 UTC. At this time there are also thunderstorms developing in the model forecast; Fig. 8.16 is the reflectivity deduced from the model hydrometeors (Eq. 4.4) at the first model level above the ground for 2010 UTC. Note that although similar storms are forming in the model there are differences in the location of individual cells. The 3-km run did not make on accurate forecast of the cell that had formed early in the afternoon in the Oklahoma panhandle -- it formed late, and is displaced to the northeast, but moving out of the domain. Nevertheless, it may be important for later storm interactions, due to its outflow, for example. The model forecast of the wind shift associated with the dryline was a little too far west (approximately 30 km near Borger, see Fig. 8.17). The largest errors, however, were in the Oklahoma panhandle, where temperatures behind the stationary front were too warm -- up to 5 C (excluding a larger error at a thunderstorm- influenced observation). In some places the wind behind the front was more easterly than the northeast observed winds.

Phase correction was first applied at this time. The field of phase correction vectors at the surface (k=2) is shown in Fig. 8.18. We see a general shift to the south, likely in response to the temperature and wind errors behind the front, and the phase-corrected surface temperature field (Fig. 8.19) shows improvement due to that adjustment. The phase correction aloft (Fig. 8.20) identifies the northeast displacement of the cell in the Oklahoma panhandle as well as the displacement of two areas of convection in the northeast Texas panhandle, one toward the north (southward correction indicated), the other toward the southwest. Figure 8.21 shows the reflectivity from the model after the phase correction has been applied. Due to the extent of the error in the development of the storm in the northeast corner of the domain, it has a distorted appearance, but the other cells seem to have been repositioned well with some broadening.

At one-half hour and on to one hour after the phase correction the phase corrected forecast maintains an advantage over the control run. Figures 8.22 and 8.23 are the radar reflectivity displays for 2038 UTC and 2110 UTC, respectively (Note: due to a hardware problem on the data recorder at Amarillo, the 2110 UTC and subsequent radar images are produced from NIDS data). Figures 8.24 and 8.25 are the control and phase-corrected runs, respectively, at 2040 and 2110 UTC. At 2040 the phase-corrected run has a better position for the cells just south of the center of the figure, and the storm in the Oklahoma panhandle is larger. At 2110 UTC, one hour after correction some storm development and interaction has occurred so that the original cells are not as distinguishable, but the net effect on the forecast is still positive, the main difference being a break in the north-south line convection down the middle of the figure in the control forecast and not in the radar image or the phase-corrected run.

Figures 8.26 and 8.27 are the radar reflectivity displays for 2159 and 2259 UTC, respectively. These verify the forecast about 2 and 3 hours after the data time shown in Figures 8.28 and 8.29 for the control and phase-correct forecasts, respectively. The advantage for the phase corrected forecast at 2200 UTC is now only slight, and is evidenced by a more solid appearance of the north-south line and a lack of spurious convection in northwest Oklahoma. By 2300 UTC, enough storm interactions and other errors have accumulated so there are no significant differences to point out between the two runs. It is of interest to note, however, that both of these forecasts are fairly accurate, containing the most significant cells (the southern end of the line in the eastern Texas panhandle produced the damaging tornadoes), and correctly had some details about the structure of the cells. There is evidence of the strong rotation (suggestive of the tornadic potential of these cells) in both of those storms, including the strong reflectivity gradients on the south side, surface vorticity, and apparent developing hook. Those cells are about only one-half county (about 20 km) too far north in the model forecasts compared to the radar. Diagnostic studies of the tornadic cells might benefit from a position-corrected model state from either of these forecasts.

Additionally, forecast runs were made with ADAS initialization at 2010 UTC with the control model as a background (ADAS_Only) and with ADAS using the phase corrected forecast as a background, also at 2010 UTC (Shift+ADAS). The phase corrected forecasts shown previously did not include the ADAS step. Figure 8.31 is the ADAS analysis at 2010 on the control model. No reflectivity appears at level 2 because the cloud analysis zeroes out the hydrometeor fields and the cells do not appear on radar that low, partly due to the beam height. The cell in the Oklahoma panhandle is rather distant from the Amarillo and Dodge City radars, so reflectivity first appears in the analysis at level 20 (about 2100 m AGL). It does seem to be well positioned, however. The ADAS analysis applied on the phase corrected field is shown in Fig. 8.32. It is not much different than Fig. 8.31; the reflectivity fields are the same as expected due to the hydrometeor zeroing removing differences in the first guess fields between ADAS_Only and Shift+ADAS. There are differences in the wind field, primarily at low-levels in the Oklahoma panhandle, where a slightly stronger northerly component is found in the ADAS analysis on the phase corrected field due to the shift of the front toward the south.

The results for some sample times (2040 and 2110) are shown in Figs. 8.33 and 8.34, for ADAS with phase shift and ADAS alone, respectively. There is only a small difference between the control run and its counterpart including ADAS. That is despite the initialization of the cloud fields in the proper location. The ADAS run did have a couple of spurious (but fairly insignificant) additional cells at the 1-hour mark. The Shift+ADAS run also has just a slight change from the run with phase shift alone, so the hydrometeor fields seem to be adjusting to the fields provided by the phase correction, despite beginning identical to the ADAS run. The lack of impact of ADAS in this case may be due to the lack of surface observations in this region, as the data over most of the domain are much more sparse than within the Oklahoma mesonet.

At later times, the same effect is observed: the ADAS on the control run represents a small departure from the control run (see Fig. 8.35), while the Shift+ADAS (shown in Fig. 8.36) forecast represents a small deviation from the phase corrected forecast without ADAS.

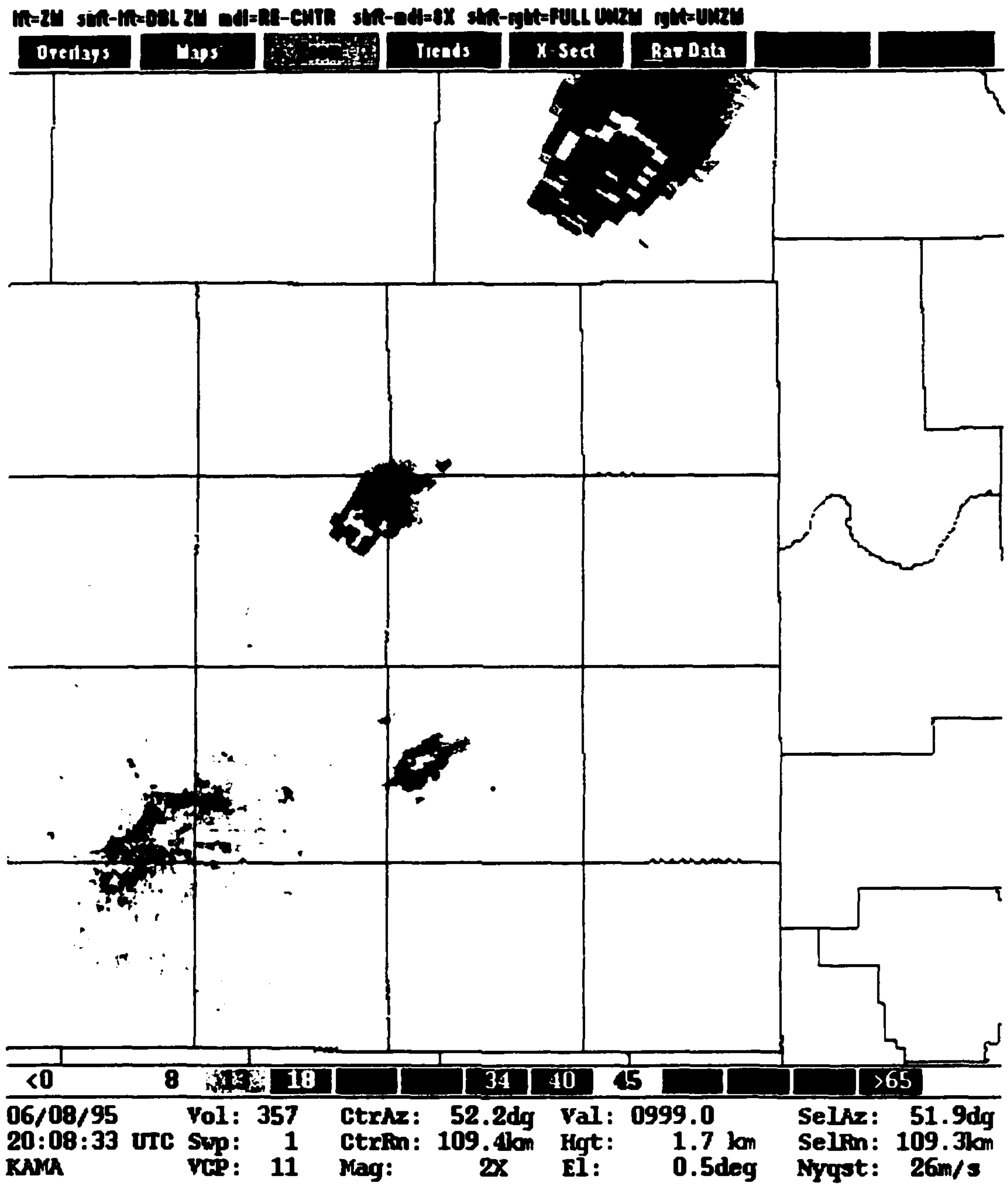

Figure 8.15 Amarillo (KAMA), Texas, radar reflectivity (dBZ). 2008 UTC 8 June 1995. 0.5 degree elevation angle.

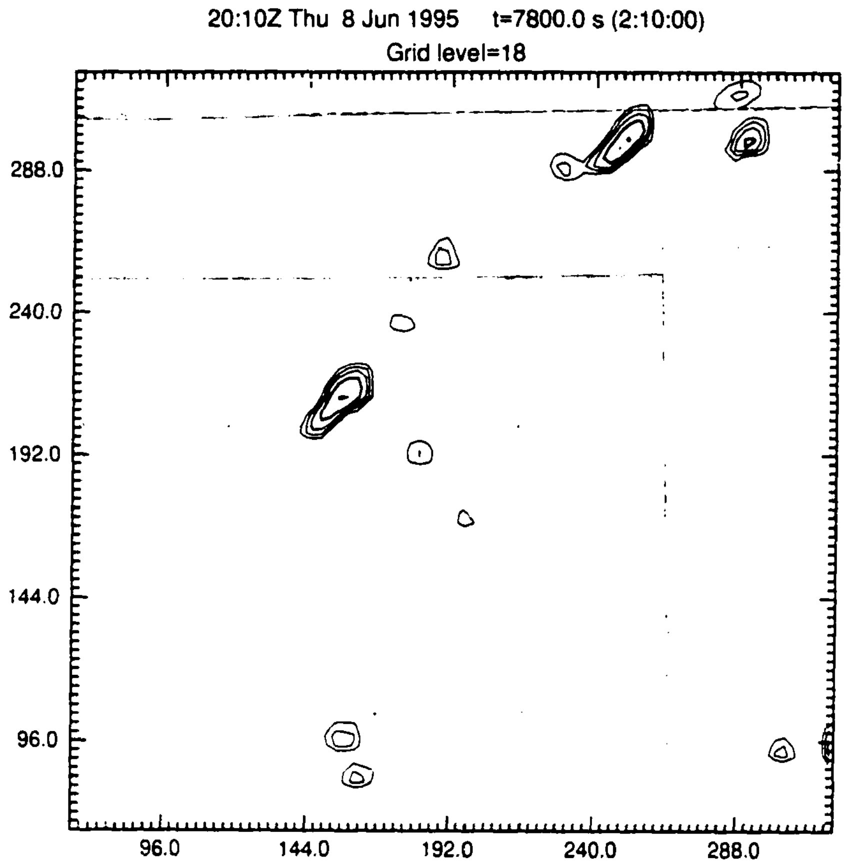

Figure 8.16 Model reflectivity (dBZ) forecast for 2010 UTC 8 June 1995.

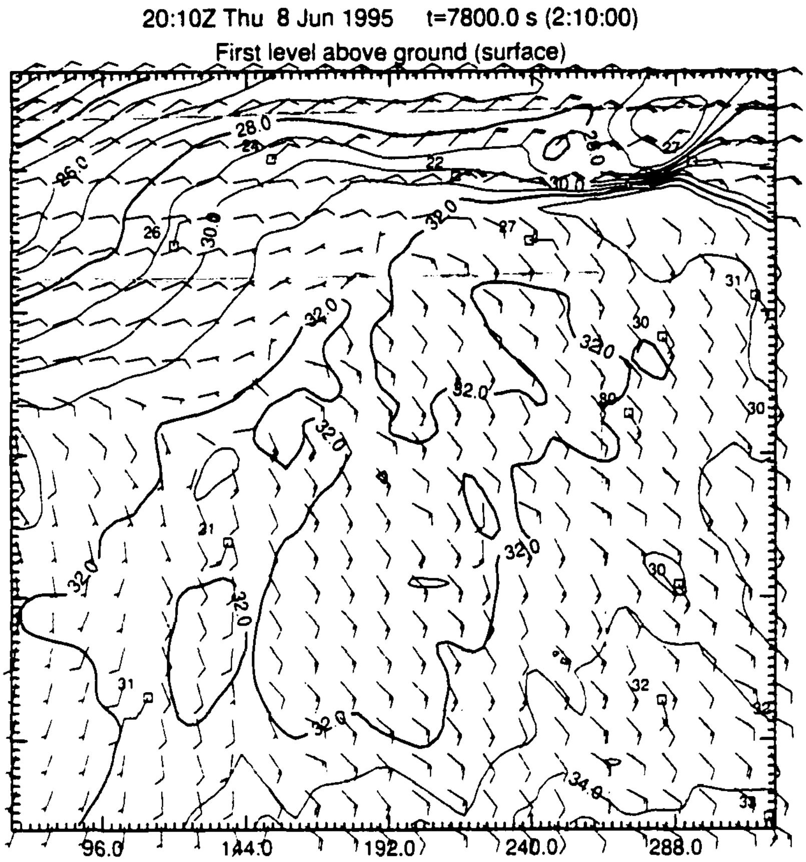

Figure 8.17 Surface temperature (C) and wind (m/s) forecast at *2010* UTC 8 June 1995.

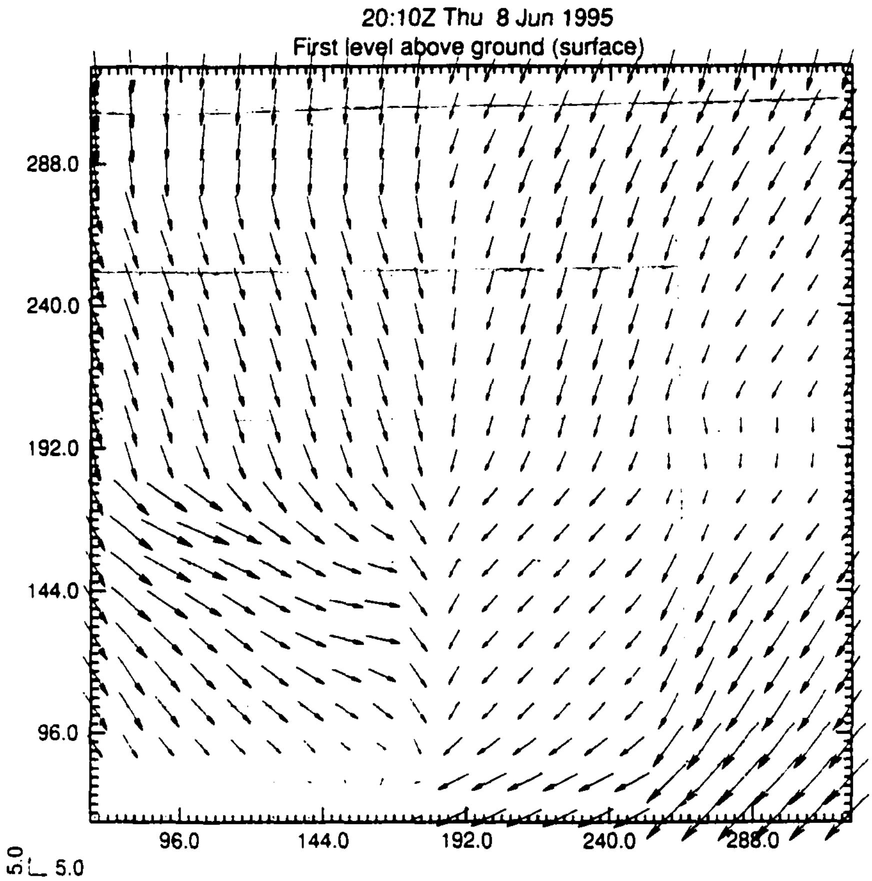

Figure 8.18 Phase shift vectors for k=2 at 2010 UTC. Vector scale in the lower-left corner is in unit grid lengths (1=3-km).

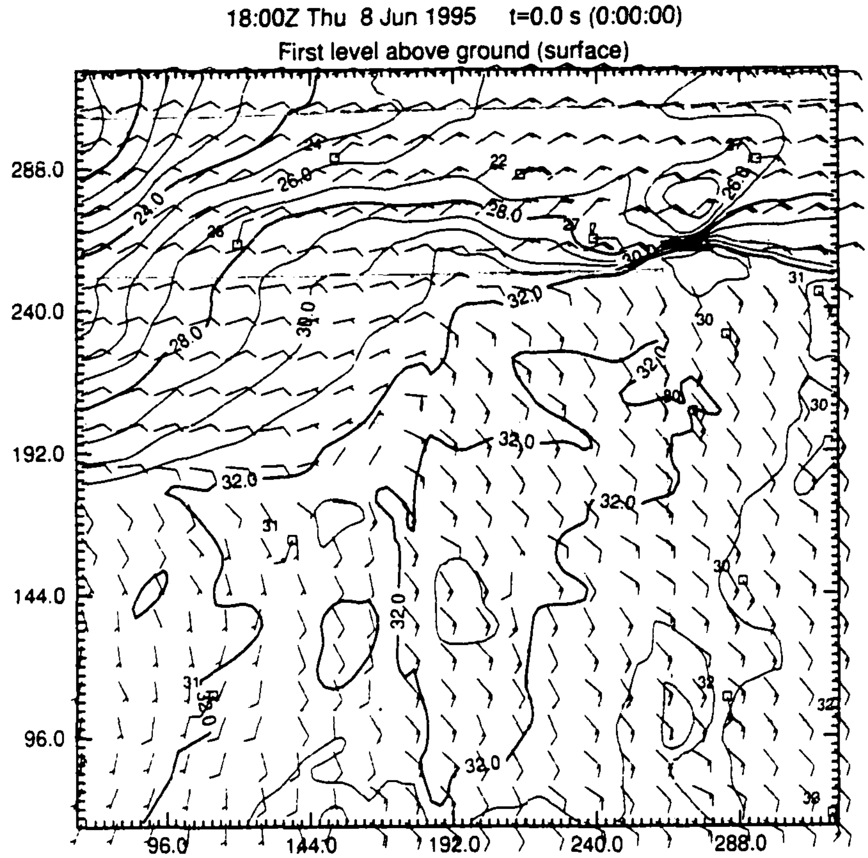

Figure 8.19 Surface temperature (C) and observations after phase correction.

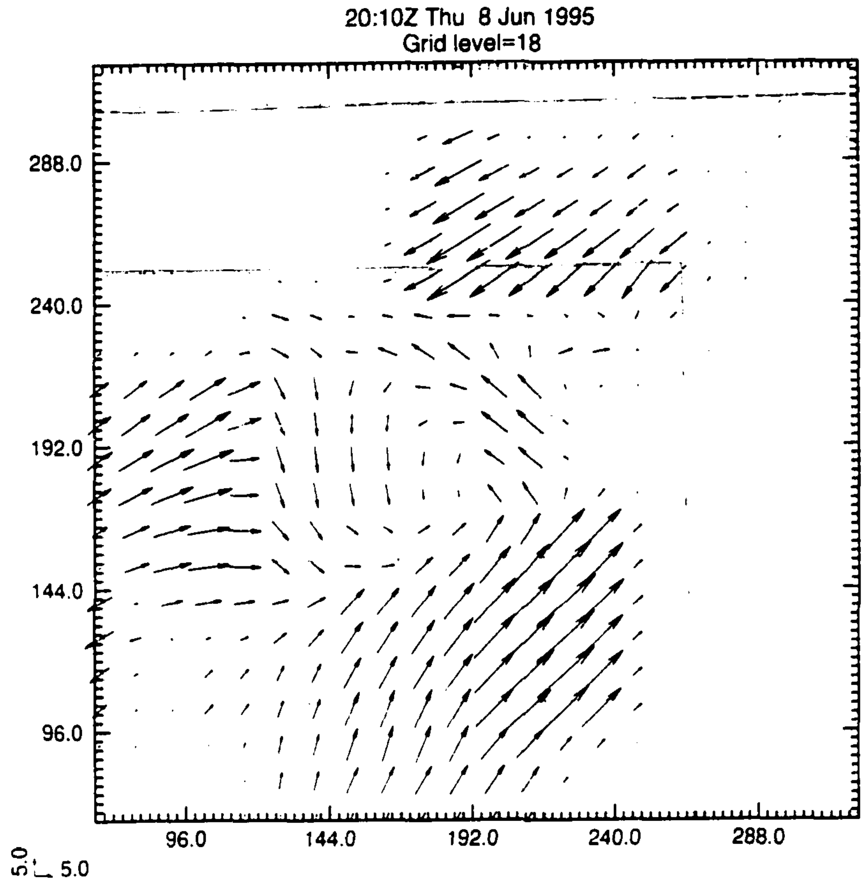

Figure 8.20 Phase shift vectors for grid level 18. Vector scale in lower-left corner is in unit grid lengths (1=3 km).

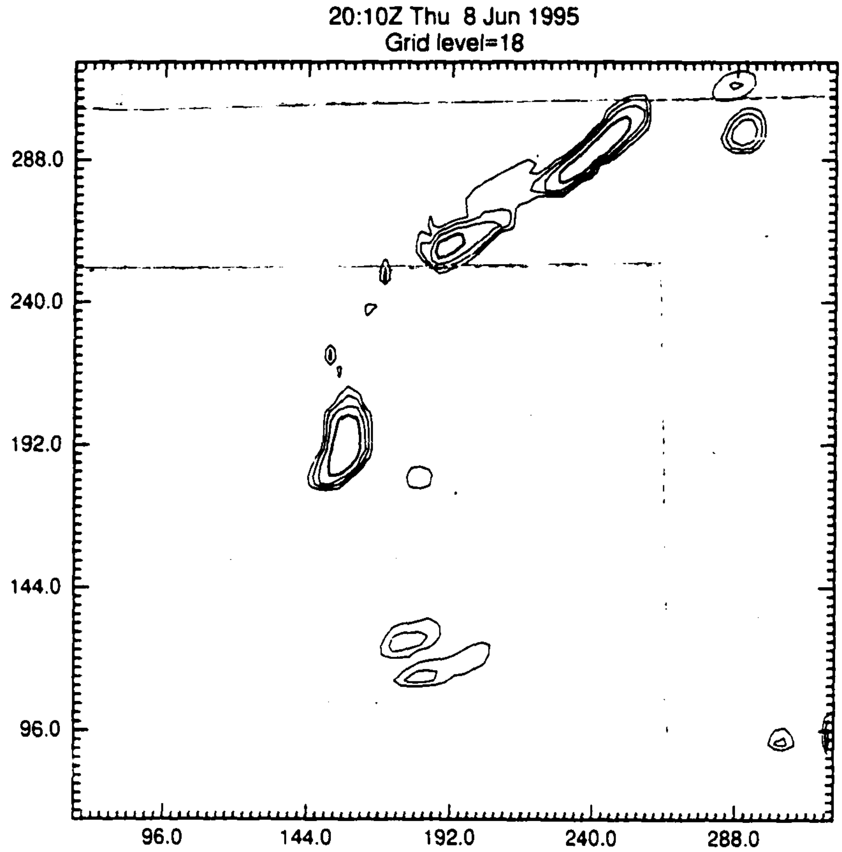

Figure 8.21 Model reflectivity at grid level 18 after phase shift applied.

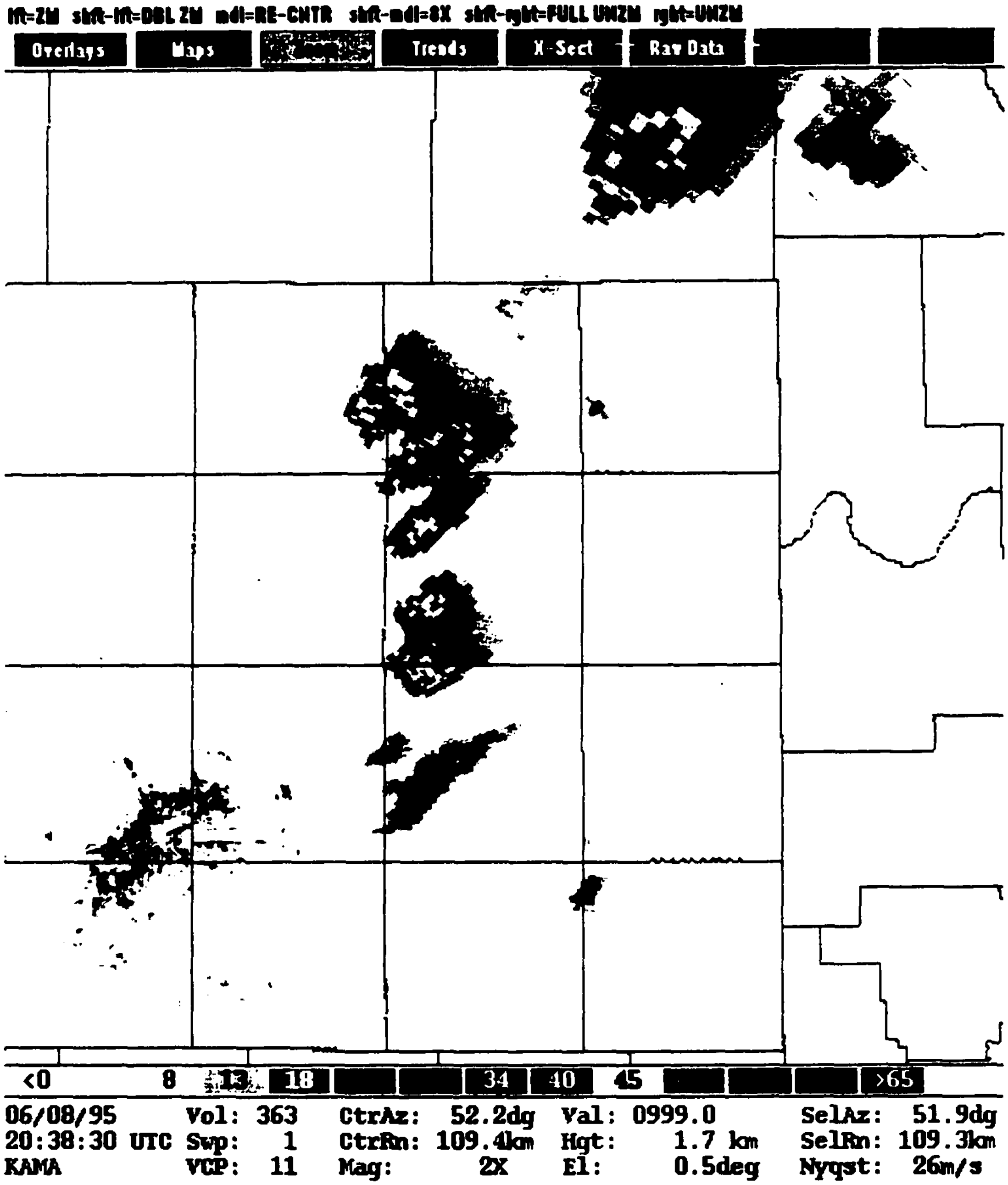

Figure 8.22 Amarillo (KAMA), Texas, radar reflectivity (dBZ). 2038 UTC 8 June 1995. 0.5 degree elevation angle.

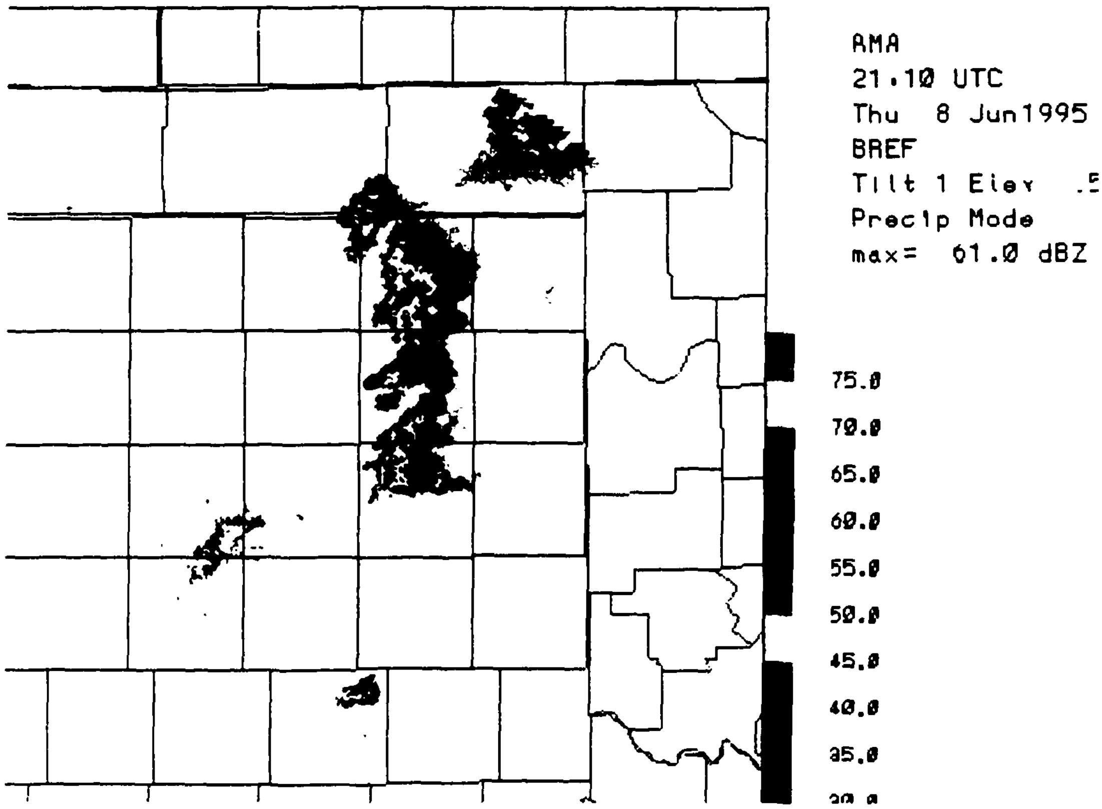

Figure 8.23 Amarillo radar reflectivity for 2110 UTC 8 June 1995, 1 hour after analysis.

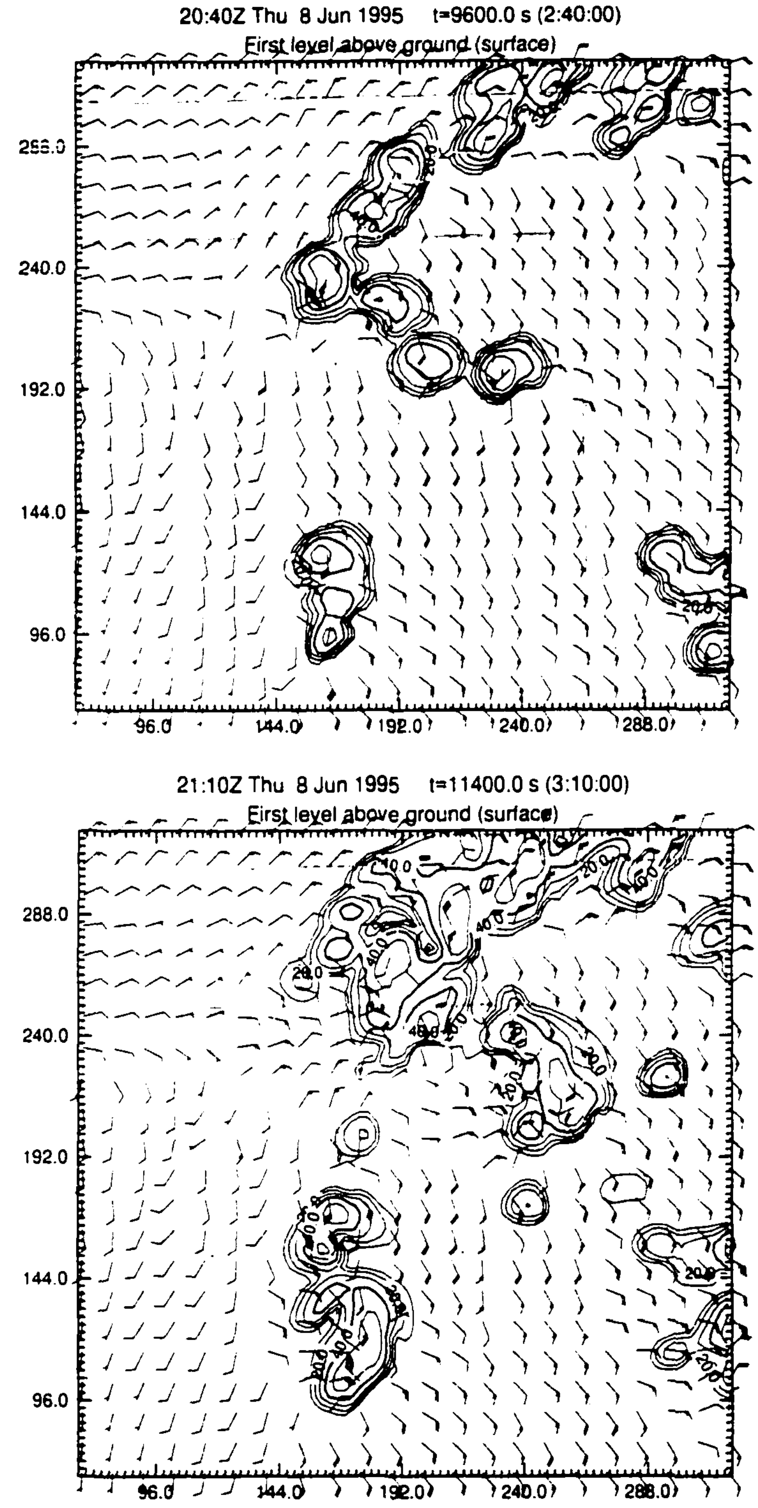

Figure 8.24 Reflectivity and surface wind forecast, control run at 2040 UTC.

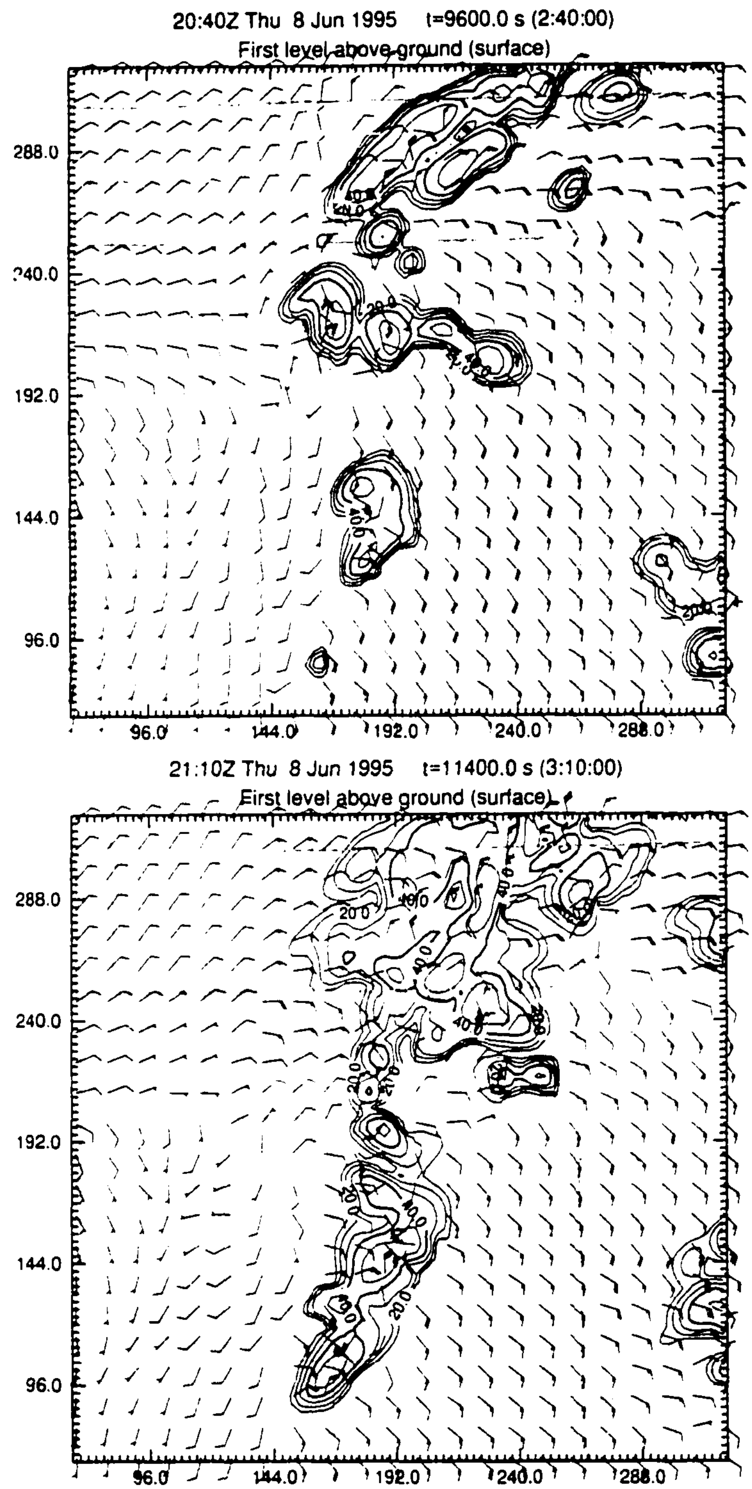

Figure 8.25 Reflectivity and surface wind forecast, phase-corrected run at 2040 and 2110 UTC.

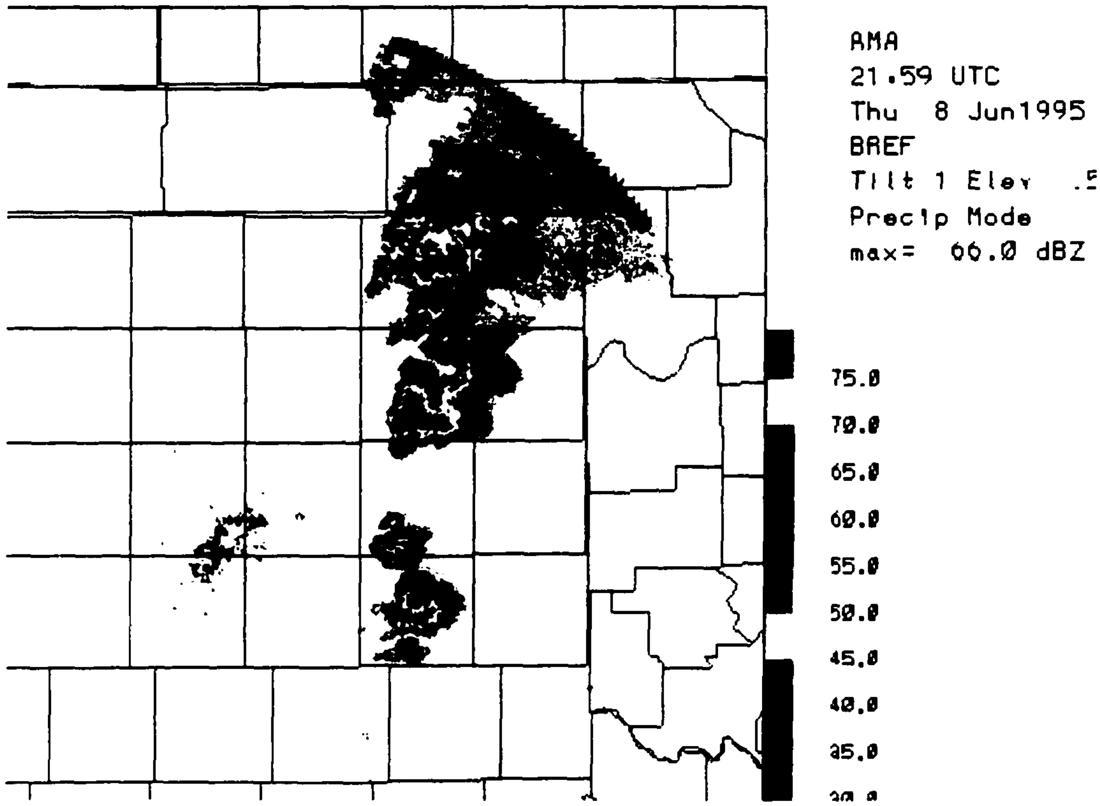

Figure 8.26 Amarillo radar reflectivity for 2159 UTC 8 June 1995, about 2 hours after analysis.

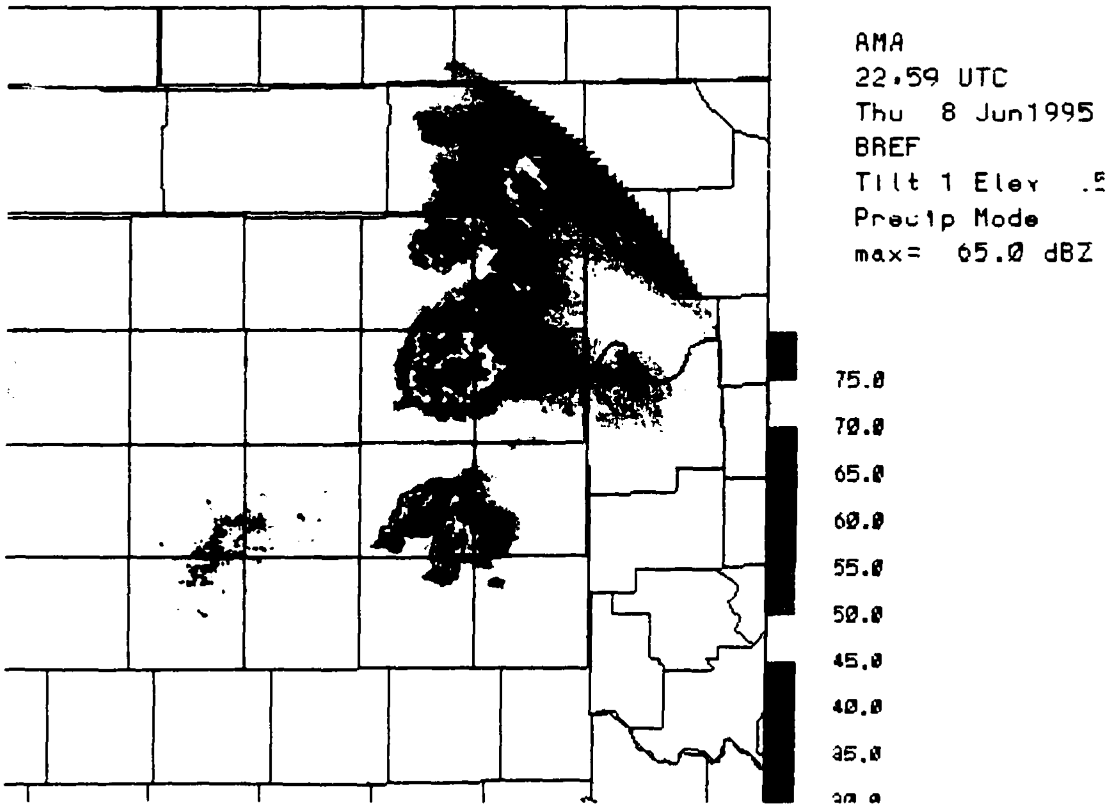

Figure 8.27 Amarillo radar reflectivity for 2259 UTC 8 June 1995, about 3 hours after analysis.

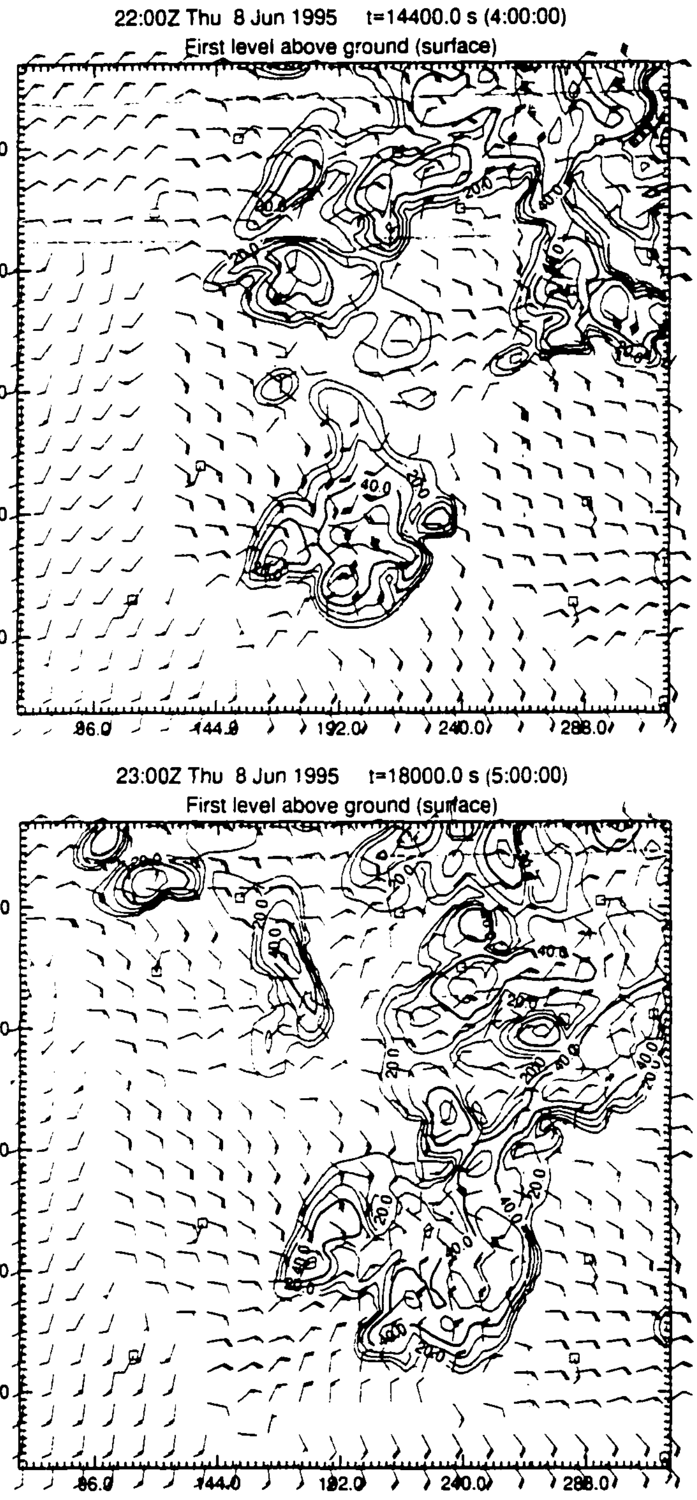

Figure 8.28 Reflectivity and surface winds at 2200 and 2300 UTC, for control forecast.

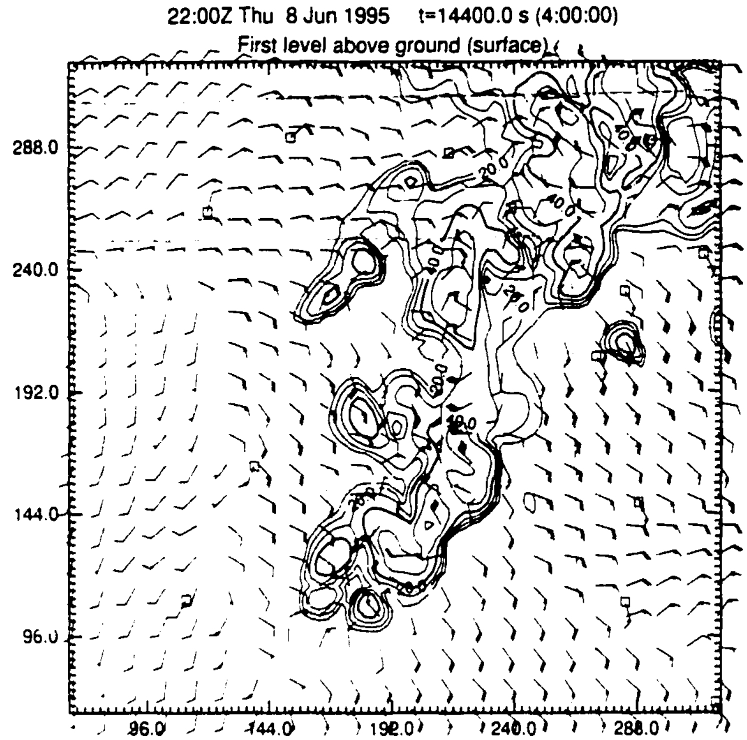

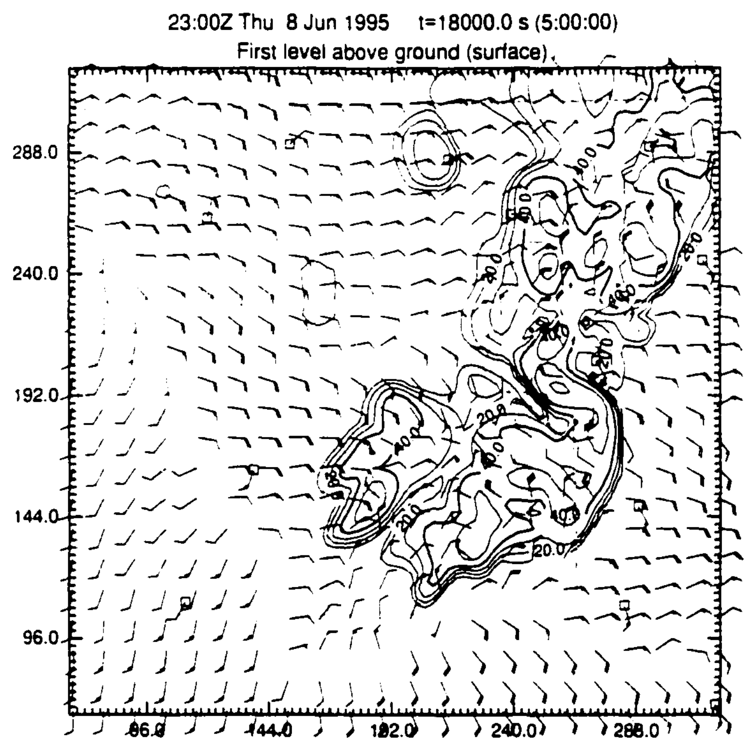

Figure 8.29 Reflectivity and surface wind at 2200 and 2300 UTC, for phase-corrected forecast.

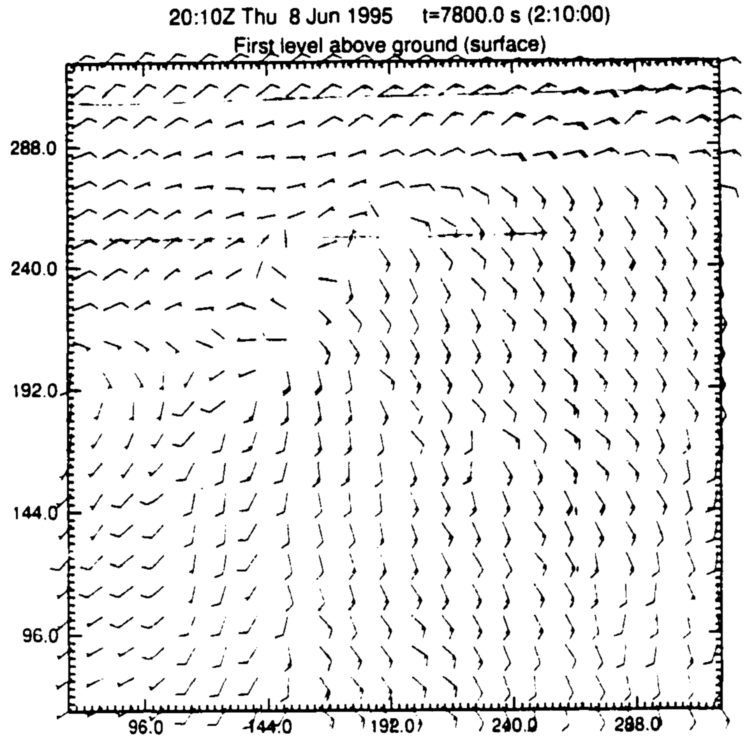

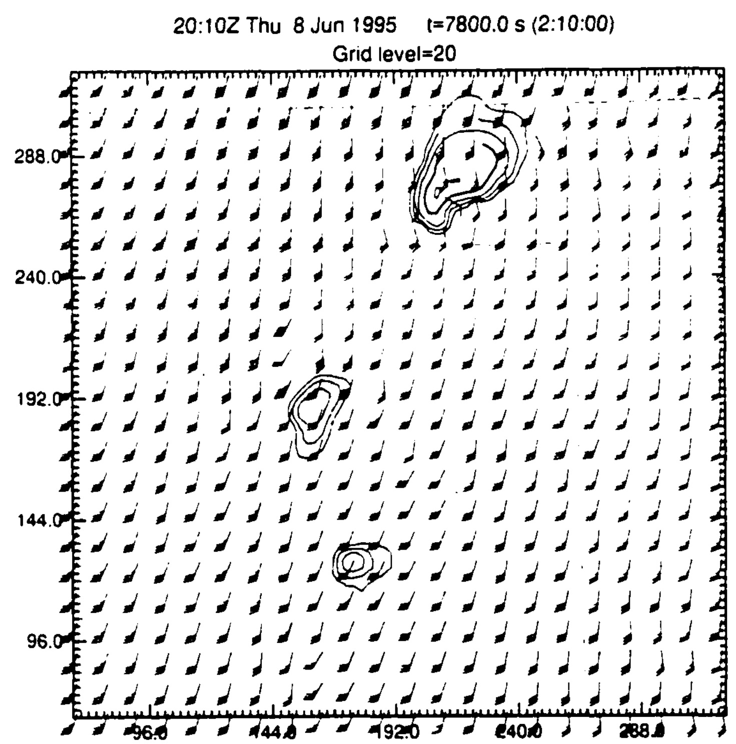

Figure 8.30 Reflectivity and wind (m/s) for ADAS-only analysis at 2010 UTC. Level 2 (surface) and Level 20.

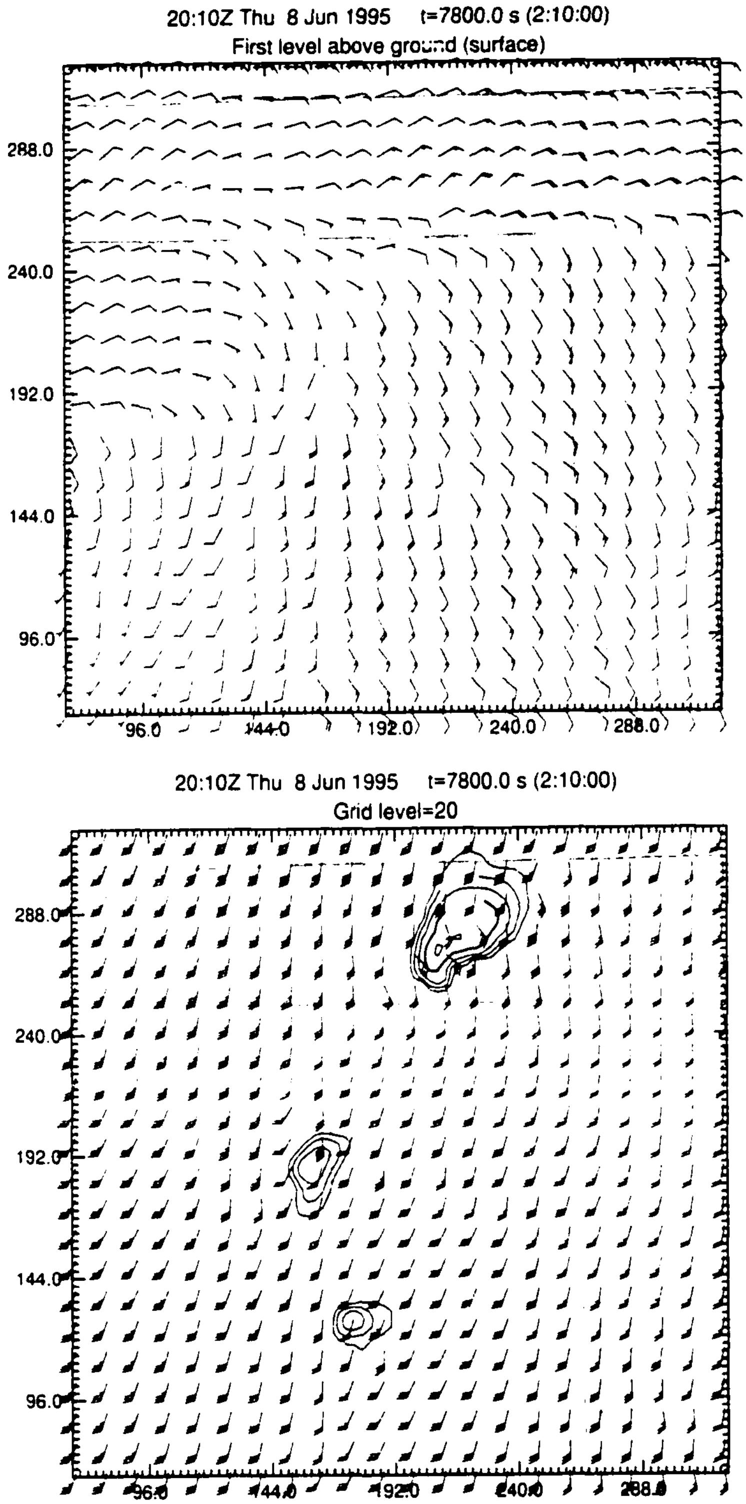

Figure 8.31 Reflectivity and wind (m/s) for ADAS analysis on phase-corrected forecast at 2010 UTC. Level 2 (surface) and Level 20.

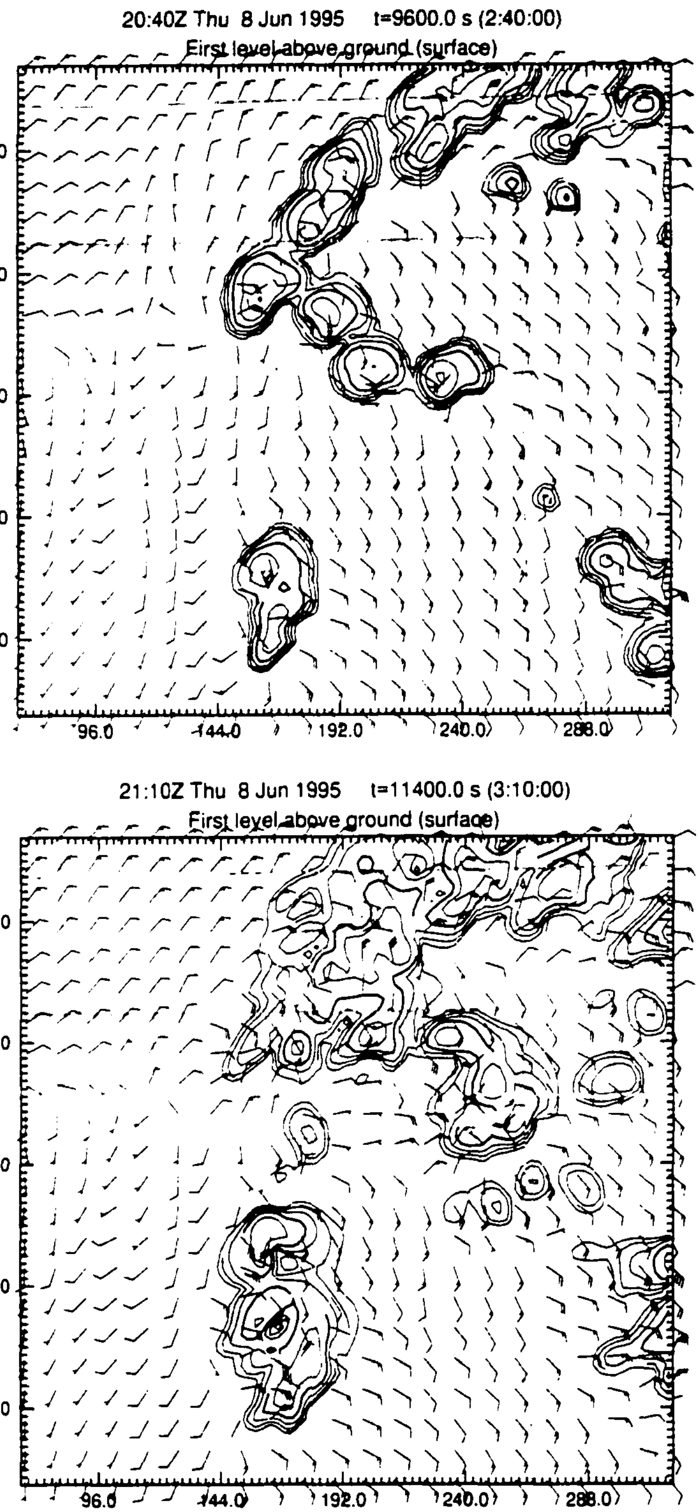

Figure 8.32 Reflectivity and surface wind forecast ADAS-only forecast at 2040 and 2110 UTC.

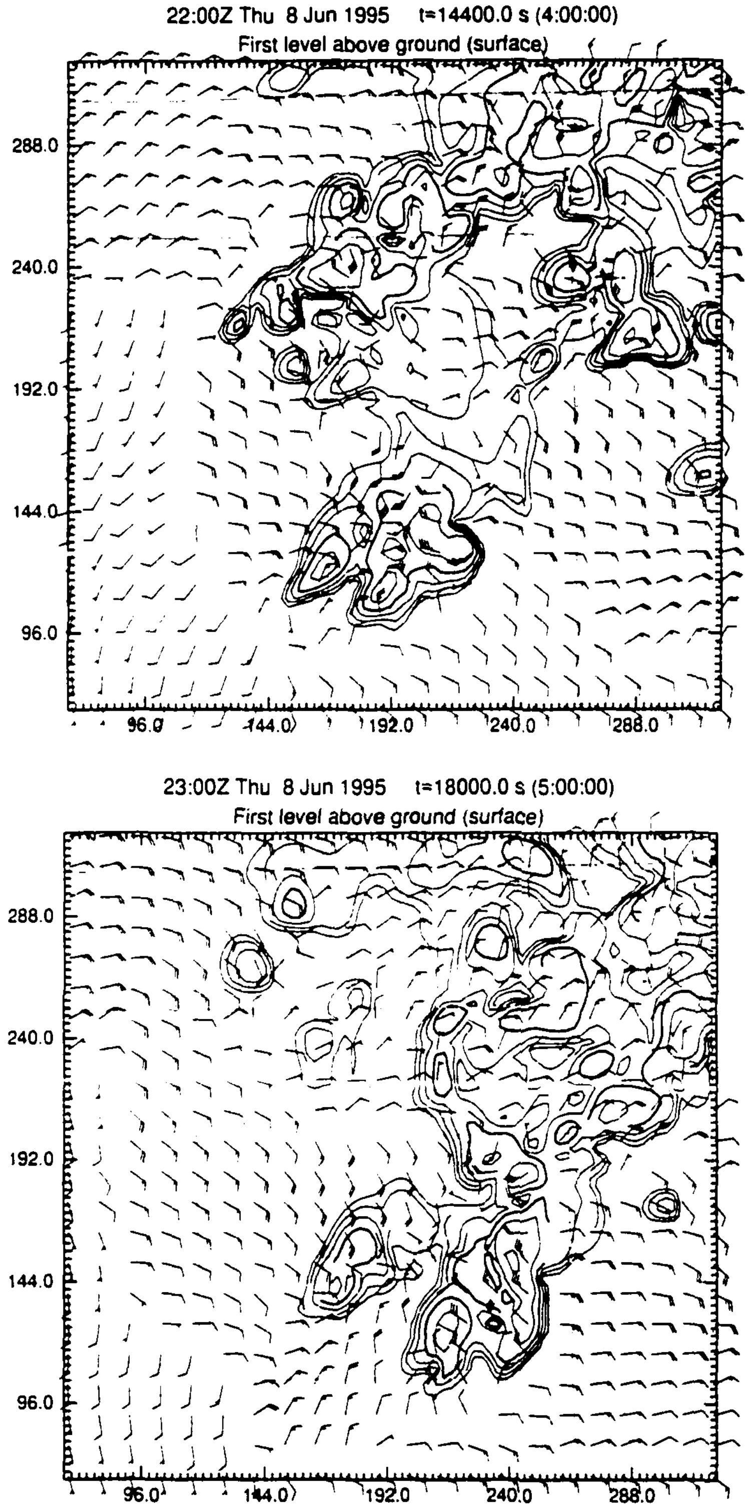

Figure 8.33 Reflectivity and surface wind forecast ADAS-only forecast at 2200 and 2300 UTC

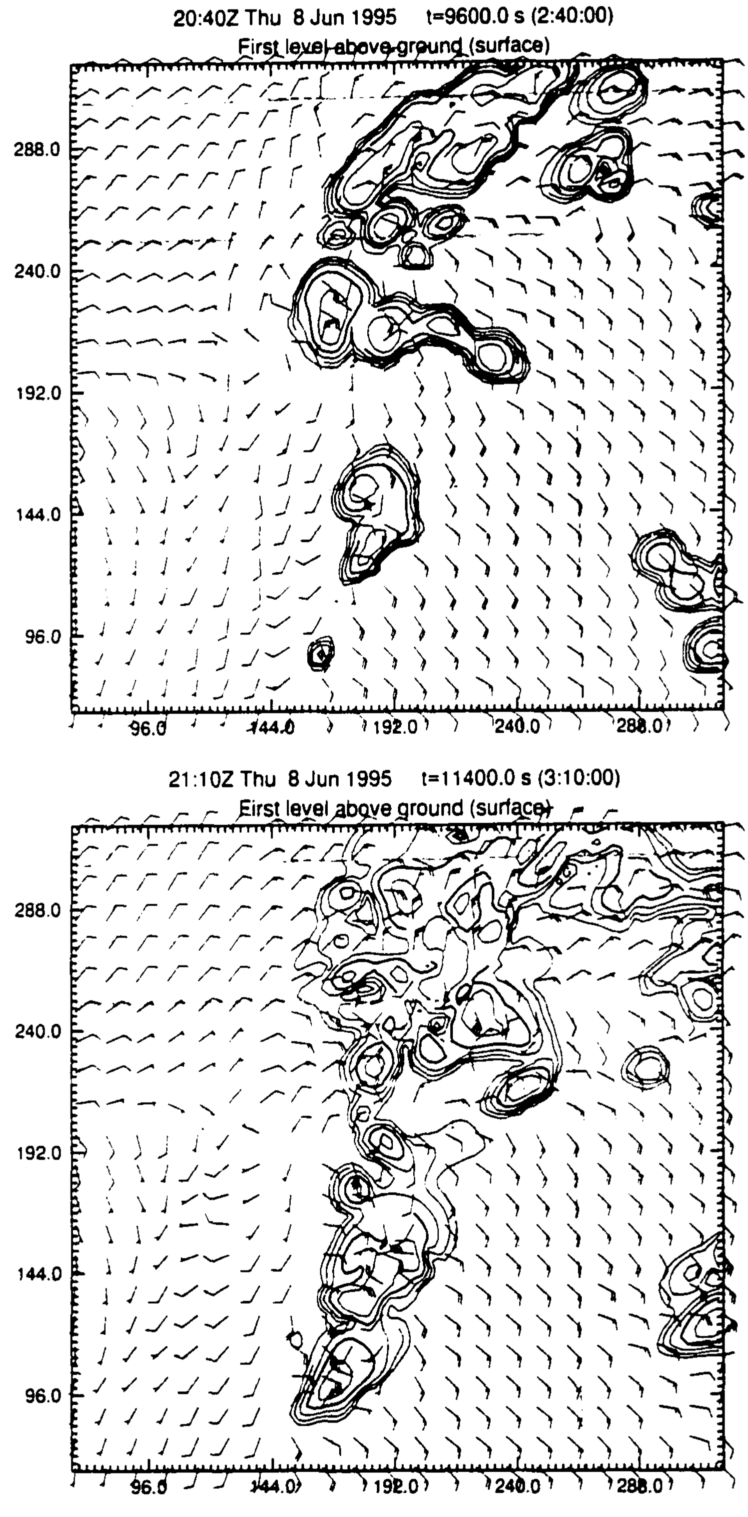

Figure 8.34 Reflectivity and surface wind forecast, Shift and ADAS forecast at 2040 and 2110 UTC.

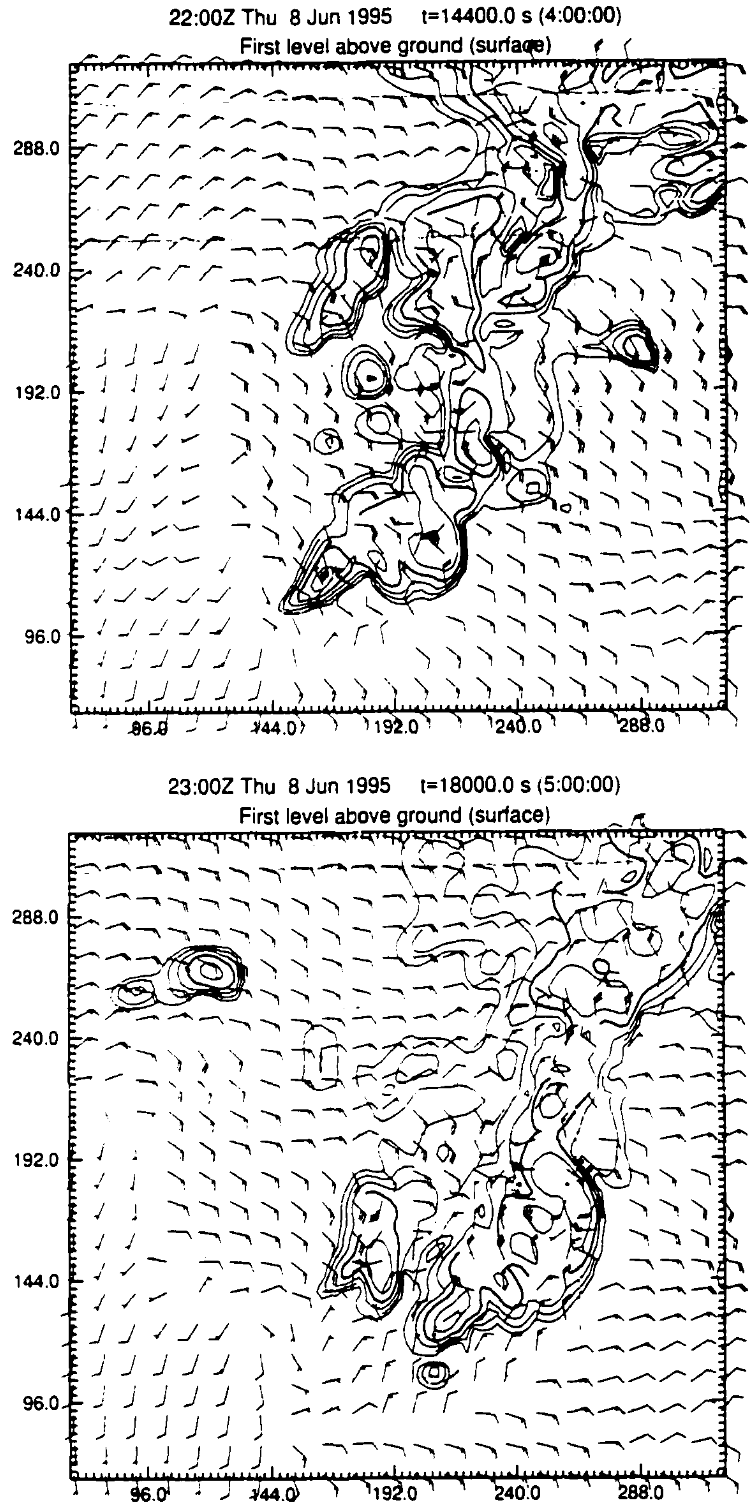

Figure 8.35 Reflectivity and surface wind forecast, Shift and ADAS forecast at 2200 and 2300 UTC

8.5 3-km Precipitation Verification

For a quantitative verification of the forecast experiments, the precipitation forecasts are compared to the hourly Stage-III precipitation fields (Fulton et al., 1998) computed by the Arkansas-Red Basin River Forecast Center (ABRFC). The observed precipitation fields are produced by estimating the rainfall rate from the radar, correcting the observations for biases based on rain gauge observations (one bias coefficient computed per radar), and mosaicking the bias-corrected rainfall data from different radar sites onto a 4-km x 4-km grid.

Three scores will be used in the forecast evaluation, the bias, threat score and the maximum threat score attainable by grid shifting (MTSS). The bias is defined as:

$$Bias = \frac{\sum_{i,j} R_{forecast}(i,j)}{\sum_{i,j} R_{verification}(i,j)}$$

where the summation is done over all i,j grid points (excluding a frame of 5 points along the boundaries), $R_{forecast}$ represents the forecast hourly precipitation, and $R_{verification}$ is the verification precipitation. In this case, the verification is provided by the ABRFC rainfall data interpolated to the forecast grid. The threat score is defined as

$$TS = \frac{C}{F + R - C}$$

where C is the number of points where precipitation over a specified threshold was correctly forecasted, F is the number of grid points with forecast precipitation over the threshold, and R is the number of points with observed precipitation above the threshold. In this work, 1 mm is chosen as the threshold for the threat score.

As described elsewhere in this work, forecasts of convective scale precipitation can often be misplaced in space. The overlap of the forecast and the observed precipitation, C, and hence the threat score, can be quite sensitive to such precipitation location errors. To measure how displacement errors affect threat score for a given forecast, Zhang (1999) defines the "maximum threat score with shifting" (MTSS) as the largest threat score that can be obtained by applying a uniform translation to the forecast precipitation field. The magnitude of the translation is reported as the MTSS distance (d_MTSS). Note that unlike the grid translations applied in the phase correction analysis technique used in this work, this shift is uniform across the entire domain.

Four forecast experiments for June 8, 1995 are scored: the Control (no data after 1800 UTC, Fig. 8.37) , ADAS Analysis alone (Fig. 8.38), Phase Shift Correction alone (Fig. 8.39), and Phase Shift and ADAS (Fig. 8.40). Hourly periods ending at 2100 UTC through 0000 UTC on June 9 were used. It should be noted that the model accumulated rainfall for 2100 is actually a 50 minute rainfall, but because the storms were in an early growth stage from 2000-2010, it is likely that not much precipitation was missed. Figures 8.36 and 8.37 show the ABRFC hourly precipitation interpolated to the 3-km ARPS forecast grid used for the June 8 case.

The rainfall bias is shown in Fig. 8.42. The model, in general, tends to overpredict rainfall in the early stages of this event, but the bias decreases with time. Generally one expects a shortfall in model precipitation early in the run, due to model spin-up delays, but the 3-km pre-forecast period has apparently provided the necessary spin-up and that spin-up occurred during a time when there was no observed precipitation -- the exception being at 2000 UTC, where the control forecast shows a slight lag in the

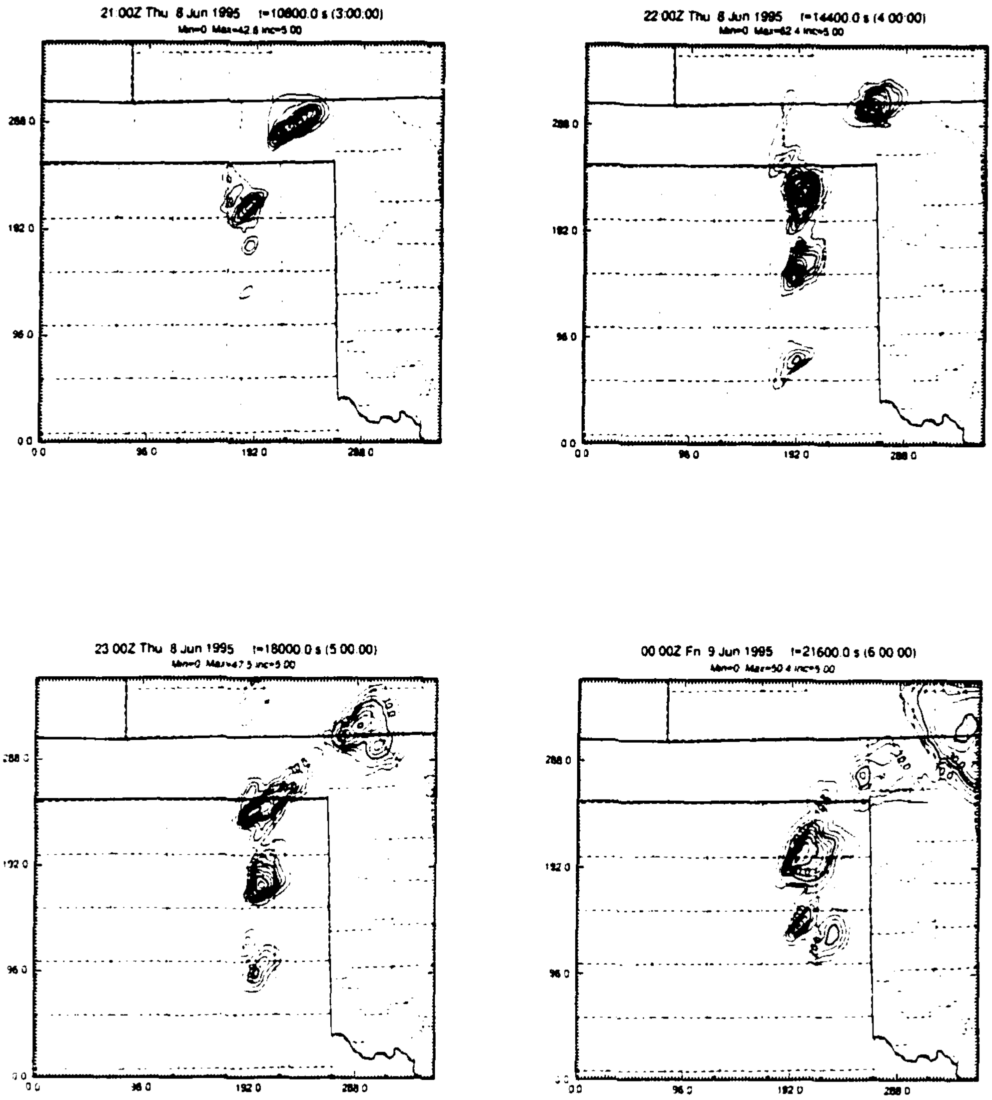

Figure 8.36 Observed hourly precipitation (mm) ending at 2100, 2200, 2300 UTC on 8 June 1995 and 0000 UTC on 9 June 1995.

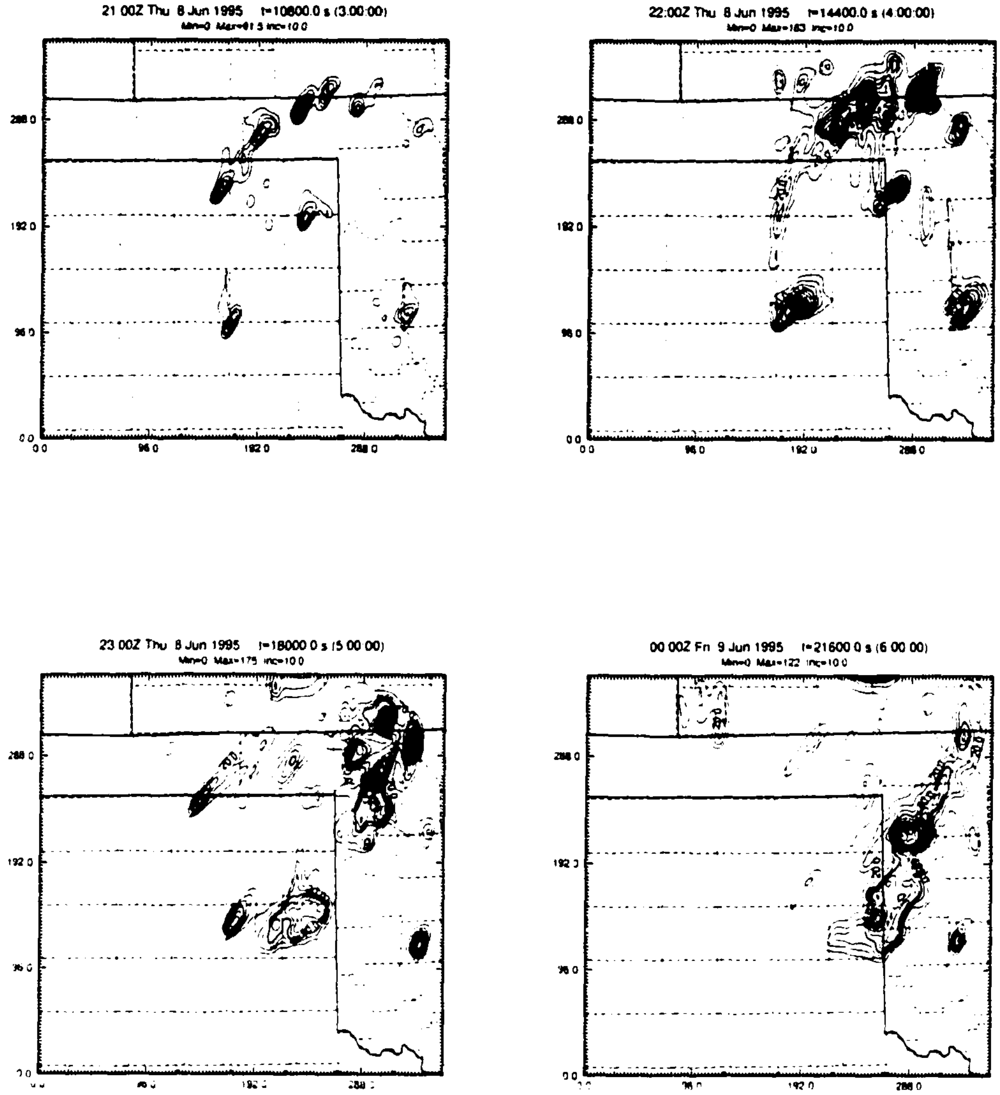

Figure 8.37 Forecast hourly precipitation (mm), Control (no data) forecast for 2100, 2200, and 2300 UTC 8 June 1995, and 0000 UTC 9 June 1995

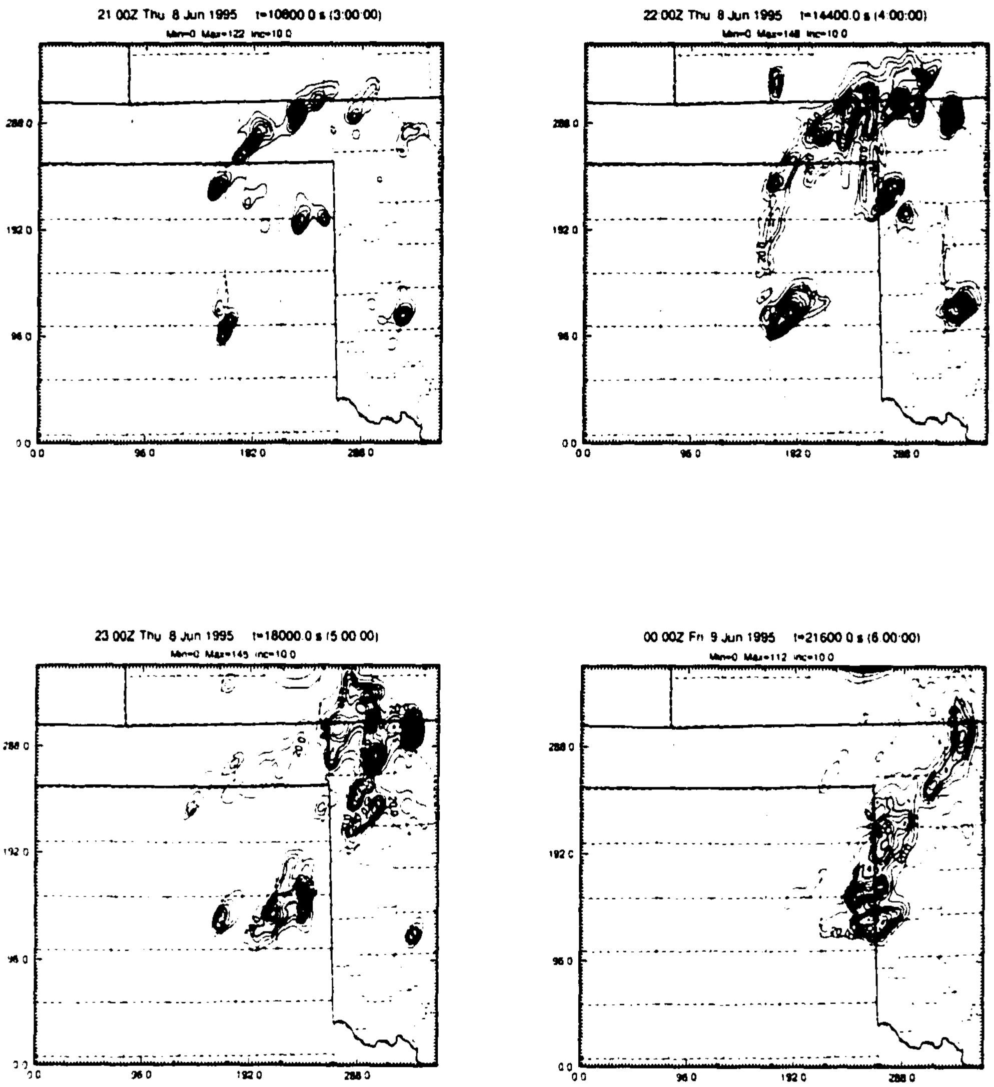

Figure 8.38 Forecast hourly precipitation (mm), ADAS-initialized forecast for 2100, 2200, and 2300 UTC 8 June 1995, and 0000 UTC 9 June 1995.

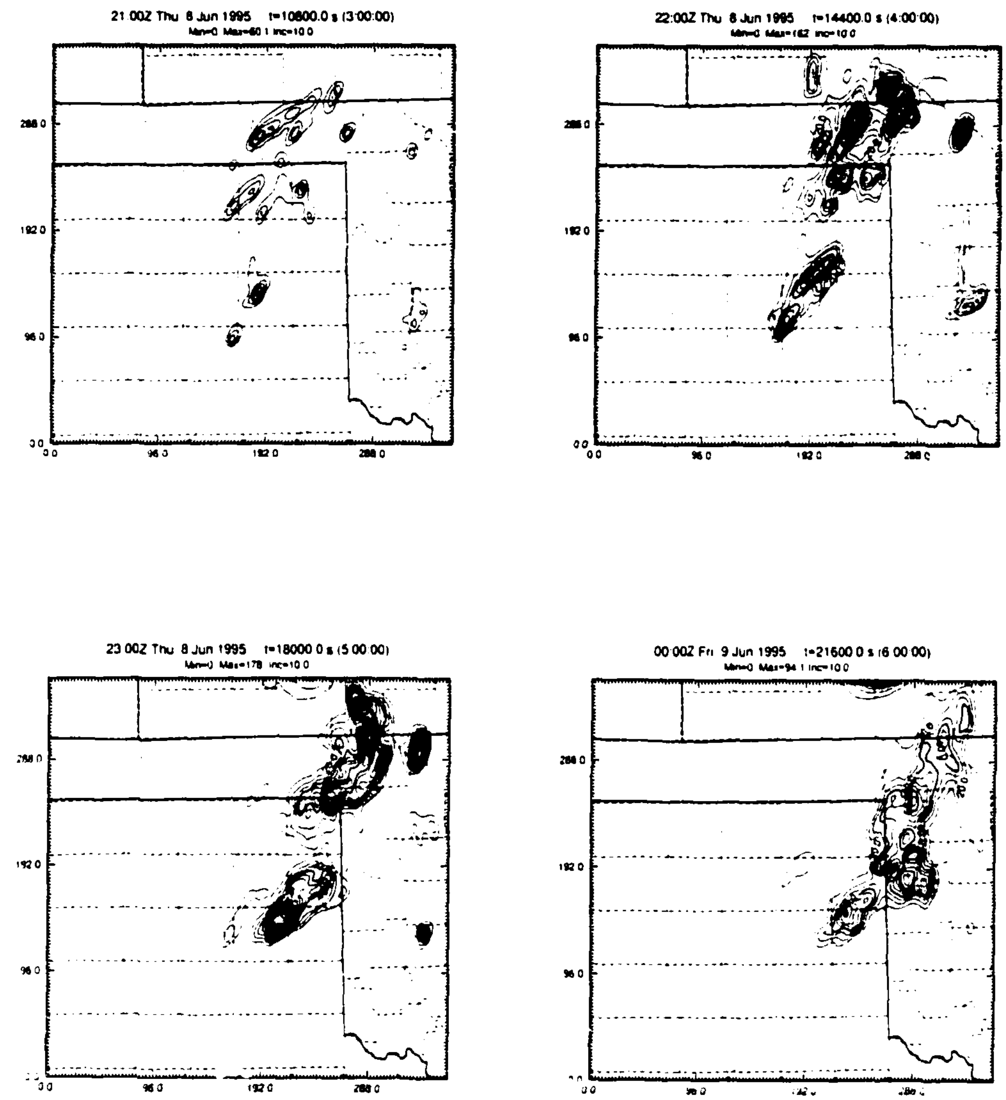

Figure 8.39 Forecast hourly precipitation (mm), Phase Shift Correction (Shift) forecast for 2100, 2200, and 2300 UTC 8 June 1995, and 0000 UTC 9 June 1995

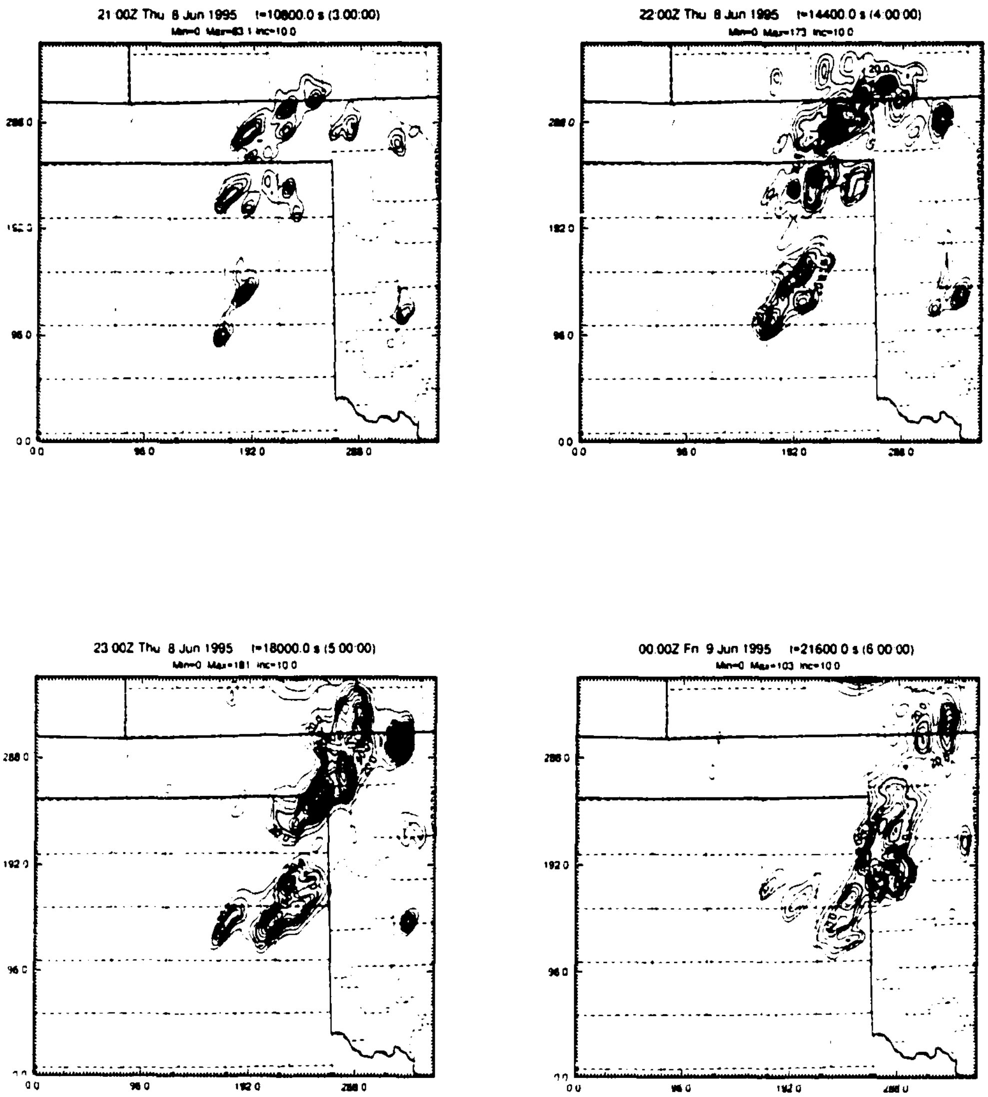

Figure 8.40 Forecast hourly precipitation (mm), Phase Shift Correction and ADAS (Shift +ADAS) forecast for 2100, 2200, and 2300 UTC 8 June 1995, and 0000 UTC 9 June 1995

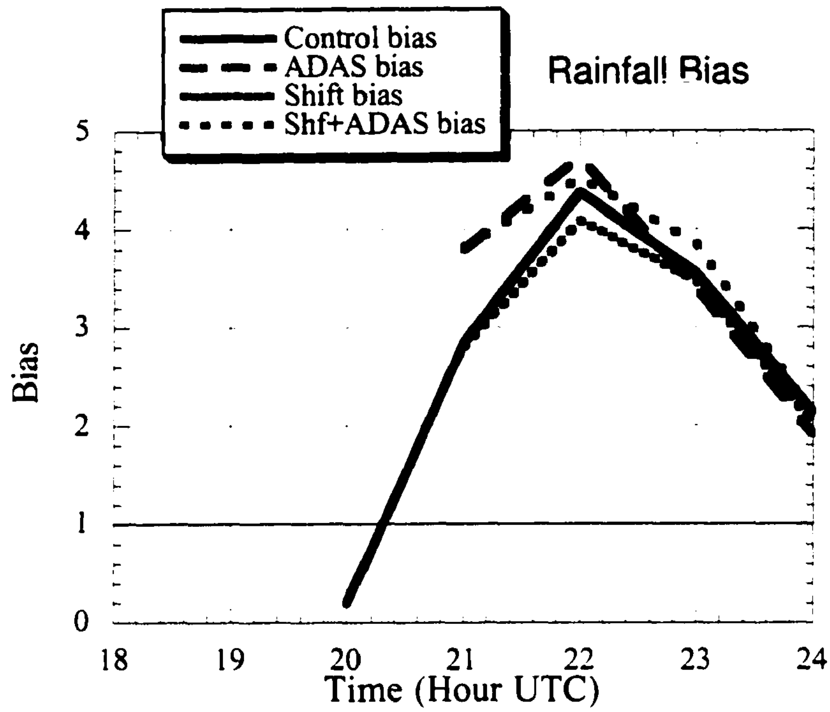

Figure 8.41 Rainfall bias for June 8 case.

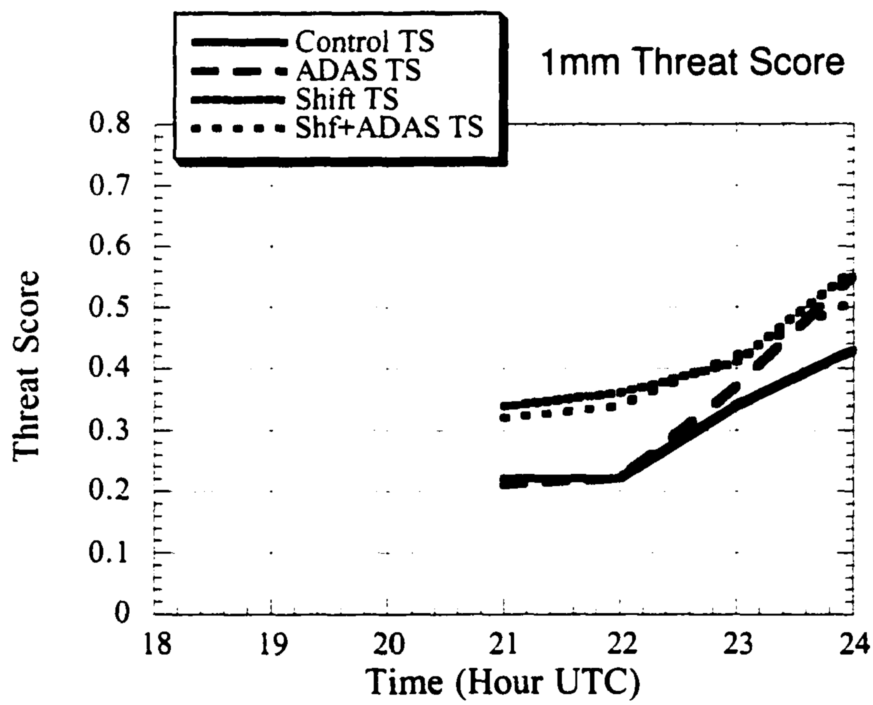

Figure 8.42 Rainfall Threat Score, 1 mm threshold.

initiation of the earliest convection resulting in one data point with bias less than unity. The other forecasts, of course, began after that time.

To help to understand why the model has such a large bias we examine closely one of the precipitation plots from the forecasts being scored. Compare the verification (Fig. 8.36) with the forecast from the Phase Corrected forecast (Fig 8.39). We can see from the precipitation plots that the rainfall is heavier in the model fields, even where it is correctly positioned. Note that the contour interval is twice that of the verification plots. There are also a few additional areas of precipitation in the model than were observed. The combined effect of these two factors leads to the high precipitation bias score. There may have been some smoothing of the verification fields due to the analysis to 4-km grids in the Stage-III processing, as we see more structure in the forecast fields, but larger area should offset any loss in peak values. There could be a problem in the ARPS model with precipitation efficiency early in the storm lifetime that causes such high biases in the early part of the run. Zhang (1999) also found positive biases in ARPS forecasts with diabatic initialization and after precipitation was spun-up in forecasts without diabatic initialization. It is beyond the scope of this work to thoroughly examine precipitation efficiency in the ARPS model.

Figure 8.42 shows the threat scores throughout the afternoon of June 8, 1995. The threat scores are pretty good for the prediction of events on this small scale, and actually increase with longer forecast time. This is most likely due to improvements with time in the forecast biases. The best threat scores were for the forecasts that included phase shifting. They are slightly better than threat scores reported by Zhang (1999) with the ARPS model and diabatic initialization of another severe weather case, which peaked at 0.4 (the forecasts using ADAS include Zhang's cloud initialization). There was very little difference coming from the addition of data via ADAS at 3-km in this case. Due to the location in the Texas panhandle, there were no mesonet data in the area of storm generation, and the use of ADAS in the 12-km spin up of the model had already helped to achieve accuracy in the forecast surface fields at initiation time.

Figure 8.43 shows the MTSS scores. Here we see improvement in the scores over the standard threat score for the control and ADAS-only runs, but little change for the runs using the phase shift technique in their initialization. From the plot of d_MTSS, Fig. 8.44, it is apparent that the runs initialized with a phase shift have a smaller phase error throughout the period of comparison, though by 0000 UTC the difference among all runs is small.

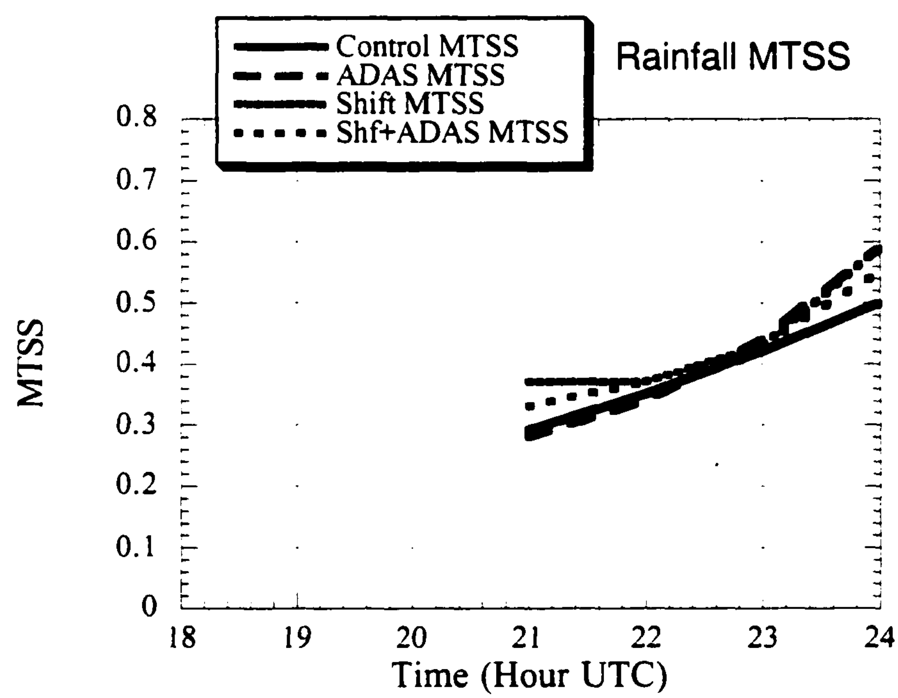

Figure 8.43 Maximum phase shifted threat score, 1 mm threshold.

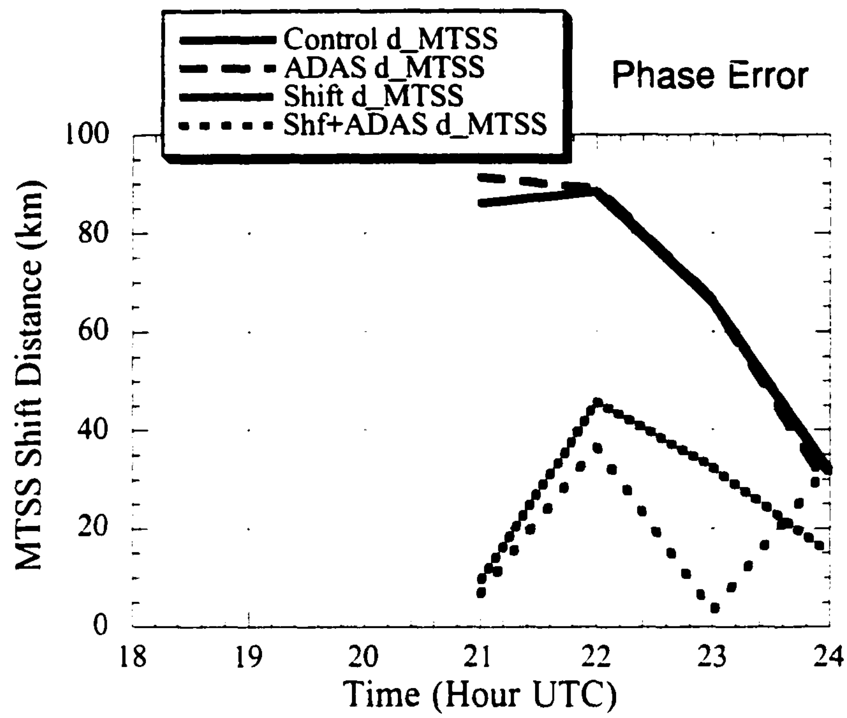

Figure 8.44 Phase shift to maximize threat score.

Chapter 9 Conclusions and Future Work

9.1 Conclusions

Two strategies for improving initial conditions for mesoscale and storm-scale numerical forecasts have been designed and tested, a unique method of objectively correcting for phase or position errors in model forecasts, and an analysis scheme that able to use Doppler radar wind data in combination with other high resolution data. The analysis scheme also includes continuous assimilation by means of analysis increment updating.

The phase correction scheme has been tested on simple models, in an observing system simulation experiment, and on real data. In simulations involving simple models in one- and two dimensions, the phase correction scheme is able to identify phase errors in the forecast and correct errors based on observations of a single variable. The effect of the phase correction extends to other variables and the improvement persists in time. The conclusions still hold in the face of random, simulated, data errors. The use of a root-mean-square error statistic to objectively identify the phase error is found to be more robust to data error than finding the error using a correlation statistic.

In the observation system simulation test, the phase correction scheme is shown to be able to find and correct position errors in thunderstorms using radar data, even when the position errors are different for neighboring thunderstorms. The improvement in the simulation due to correcting for the initial position error persists through a cycle of decline and strengthening of a thunderstorm. It was also found that making the correction for the position error in a single step was sufficient to produce a good forecast. The idea of gradually introducing the phase correction over time has merit, but details of the implementation seem to need some refinement. In particular it may be aided by a more continuous determination of the phase error during the time window in which the phase error is corrected.

In the real-data cases, it was shown that the phase correction scheme could work using mesonet and radar data as its primary input. Position errors in the forecasts of both mesoscale features and thunderstorms were identified and corrected. The impact on the forecast in the severe storm case persisted in time as forecast improvement was noted beyond 2 hours even in the face of thunderstorm interactions. By 3 hours, sufficient forecast errors had accumulated in both the phase-corrected and control runs so that the improvement was no longer discernible. This is to be expected as there is certainly a limit to the predictability of thunderstorms, and model error or biases, or near-random thunderstorm interactions will eventually compound to overcome improvements in the initial conditions.

It is demonstrated that the implementation of a ARPS Data Assimilation System can successfully combine data from multiple data sources and produce realistic simulations of thunderstorms on scales of 3-12 km, even in the presence of complex synoptic and mesoscale features. The use of a 3-hour assimilation spin-up at 12-km served well to form a mesoscale assimilated state from which to launch a high resolution (3-km) forecast for prediction of thunderstorm initiation. It was noted that many of the details of the parallel runs made to test the phase error correction were remarkably similar and had good correspondence to the behavior of storms in each sector of the region around the triple point on the test day.

9.2 Future Work

The phase correction scheme could be extended to include the use of satellite image data. Weather forecasters often use the satellite images, subjectively, for the purpose of gauging position errors in models. It may be possible to use the IR data by computing the cloud top temperature of the model data using a simple radiation model and comparing that to the observed cloud top temperature where the IR data are not sensing the ground temperature. That information would be grouped with separate data at the height in the atmosphere corresponding to the cloud-top temperature (keeping in mind the phase shift field varies in three dimensions, a height assignment is needed). Assigning a valid height to visible data is more of a problem, but perhaps not insurmountable.

Extension to the use of satellite data would pave the way for tests of the system on hurricanes. It is well know that the position of the hurricane can be subject to small scale meandering that is difficult to predict, and a hurricane represents the type of discrete feature that would have a strong signal in the metric used for finding the phase error. Both facts make the hurricane forecasting a good candidate for the phase correction technique.

The phase correction could better utilize the clear-air reflectivity information if we knew of a relationship between the non-precipitating clear air echoes and the model variables. Currently the transform to reflectivity only uses the hydrometeors. This improvement may be mitigated by the fact that the current system can, and is, using the wind data in the clear air which likely is somewhat redundant with the reflectivity data, though to the human eye the boundaries do seem to stand out more in the reflectivity data. Comparison of "spun-up" numerical model runs and radar data, with thought to theoretical radar reflectivity relations, might yield a useful relationship between high values of non-precipitating echoes and vertical velocity, horizontal wind gradients and/or moisture.

Smoothness in the field of phase error vectors is currently enforced though the use of a very simple numerical filter. There are likely more elegant ways of combining the shifts found in discrete, overlapping regions, and enforcing a specific smoothness constraint on the result.

The approach of correcting the phase error by mean of multiple small shifts may be improved. The present work employed a second order interpolation scheme which apparently had the effect of smoothing the data too much. Higher order interpolation schemes may be used, such as those developed for Lagrangian advection schemes. Such advection schemes deal with the same concerns, that is accurately finding the value of the field upstream. Similarly, a semi-Lagrangian advective method applied to the advection terms in the model itself is desirable as it would alleviate fears about the pseudo-wind advection scheme violating the CFL criterion.

Some researchers (Strum et al., 1999) have had some success in using a phase correction scheme where the phase correction is manually-determined, and rather than shift the velocity fields, the wind is broken into vorticity and divergence components, those fields are shifted, and then the velocity is reconstructed from the shifted vorticity and divergence. We did not see a specific problem in shifting the wind directly in terms of velocity components, in fact there can be benefits to allowing the divergence to vary, but it would be of interest to do some comparisons of the results of each.

Fiedler (1999) has also experimented with what he terms "storm surgery". To date, his storm surgery lacks an objective way to identify "storms" to insert and remove. It might be possible to utilize the results of the cloud analysis within ADAS to identify such regions in the following way. The output of the cloud analysis can be compared to the condition of the original background field. If areas are identified as having convective clouds (an intermediate step of the current system), and the phase corrected field does not have a storm in that region (decided based on vertical velocity and hydrometeor concentration), the methods of Fielder could be used to add the vertical wind circulation of the storm (vertical velocity as well as associated convergence at low-levels and divergence aloft). Or in the case of a spurious storm, the storm circulation could be removed if ADAS identified no storm at that location. The current

ADAS cloud analysis would have already removed or added the cloud and precipitation variables.

As with any new technique, exposure to more cases will help learn about the technique's strengths and weaknesses and will provide a better quantitative measure of forecast improvement that could be gained from its use in research or operations.

Future work on ADAS is likely to focus on the addition of more data sources and preprocessing for new data such as integrated water vapor. Although such data are more suited to 3D-VAR techniques, Kuo (1993) has shown positive impact using a scheme where local increments to the moisture field are created by simple assumptions about the distribution of the discrepancy in the model integrated quantity and the observed.

Finally, it was noted in this work that ADAS is very effective at removing biases in the background forecasts and it has been observed separately this is accomplished in early analysis passes. done with a large correlation distance factor. Since biases can affect the RMS calculations used in the RMS minimizing algorithms for phase correction a better combination of ADAS and phase correction might be to apply ADAS for a large scale pass using all available data to remove any biases that might be present, then apply the phase correction algorithm, and finish with analysis iterations in ADAS with smaller correlation distance factors.

REFERENCES

Albers, S.C., J.A. McGinley, D.A. Birkenhuer, and J.R. Smart, 1996: The local analysis and Prediction System (LAPS): Analysis of clouds, precipitation and temperature. *Wea. and Forecasting*, **11**, 273-287.

Alexander, G.D., J.A. Weinman, J.L. Schols, 1998: The use of digital warping of microwave integrated water vapor imagery to improve forecasts of marine extratropical cyclones. *Mon. Wea. Rev.*, **126**, 1469-1495.

Barnes, S.L., 1973: Mesoscale objective analysis using weighted time-series observations. NOAA Tech. Memo, ERL NSSL-62, Natinal Severe Storms Lab, Norman, OK, 60 pp. [NTIS COM-73-10781].

Benjamin, S.G., K.J. Brundage, P.A. Miller, T.L. Smith, G.A. Grell, D. Kim, J.M. Brown, and T.W. Schlatter, 1994: The Rapid Update Cycle at NMC. Preprints, *Tenth Conference on Numerical Weather Prediction*, Portland, OR, AMS, Boston, 566-568.

Bergthórssen, P. and B. Döös, 1955: Numerical weather map analysis. *Tellus*, **7**, 329-340.

Bleck, R., and S.G. Benjamin, 1993: Regional weather prediction with a model combining terrain-following and isentropic coordinates. Part I: Model description. *Mon. Wea. Rev.*, **121**, 1770-1785.

Bloom, S.C., L.L. Takacs, A.M. da Silva, and D. Ledvina, 1996: Data assimilation using incremental analysis updates. *Mon. Wea. Rev.*, **124**, 1256-1271.

Bluestein, H.B. and M.H. Jain, 1985: Formation of mesoscale lines of precipitation in Oklahoma during the spring. *J. Atmos Sci.*, **42**, 1711-1732.

Bratseth, A.M., 1986: Statistical interpolation by means of successive corrections. *Tellus*, **38A**, 439-447.

Brewster, K.A., 1991: Phase correcting data assimilation. Preprints, *Ninth Conference on Num. Wea. Prediction.*, Denver, CO., AMS, Boston, 610-613.

Brewster, K., 1996: Implementation of a Bratseth analysis scheme including Doppler radar. *Preprints, 15th Conf. on Weather Analysis and Forecasting*, AMS, Boston, 92-95.

Brewster, K.A., 1998a: Phase correcting assimilation of radar data for thunderstorm forecasting. Preprints. *12th Conference on Num. Wea. Prediction.*, Phoenix, AZ, AMS, 181-184.

Brewster, K., 1998b: *ARPS 4.0 Users Guide, Supplement 1, 3-D Analysis with the ARPS Data Assimilation System*. Available from the author at CAPS/Univ of Oklahoma, 100 E. Boyd, Norman, OK 73019. 24 pp.

Byers, H.R. and R.R. Braham, 1949: *The Thunderstorm.* U.S. Govt. Printing Office, Washington, D.C., 287 pp. (NTIS PB-234-515)

Carbone, R.E., J.W. Conway, N.A. Crook, and M.W. Moncrief, 1990: The generation and propagation of a nocturnal squall line. Part 1: Observations and implications for mesoscale predictability. *Mon. Wea. Rev.*, **118**, 26-49.

Carr, F.H., J.M. Krause, and K. Brewster, 1996: Application of the Bratseth scheme to high resolution analyses in inhomogeneous data regimes. *15th Conf. Wea. Analysis and Forecasting*, 231-233.

Chou, M.-D., and M. J. Suarez, 1994: *An efficient thermal infrared radiation parameterization for use in general circulation models*. NASA Tech. Memo. 104606, 85 pp. [Available from NASA Center for Aerospace Information, 800 Elkridge Landing Road, Linthicum Heights, MD 21090-2934.].

Cole, R.E. and F.W. Wilson, 1995: ITWS Gridded Wind Product, *Preprints, 6th Conf. on Aviation Wetaher Systems*, AMS, Boston.

Djuric', D., 1987: Arches of clouds as precursors of thunderstorms. *Mon. Wea. Rev.*, **115**, 2849-2855.

Doviak, R.J. and D.S. Zrnic', 1984: *Doppler Radar and Weather Observations*, Academic Press, Orlando, Florida, 458 pages.

Droegemeier, K.K., 1990: Toward a science of storm-scale prediction. *Preprints, 16th Conf. on Severe Local Storms*, Kananaskis Park, Alta., Canada, AMS, Boston, 256-262.

Droegemeier, K. K., M. Xue, K. Brewster, Y. Liu, S. Park, F. Carr, J. Mewes, J. Zong, A. Sathye, G. Bassett, M. Zou, R. Carpenter, D. McCarthy, D. Andra, P. Janish, R. Graham, S. Sanielvici, J. Brown, B. Loftis, and K. McLain, 1996: The 1996 CAPS spring operational forecasting period: Realtime storm-scale NWP, Part I: Goals and methodology. Preprints, *11th Conf. on Num. Wea. Pred.*, Norfolk, VA, AMS, Boston, 294-296.

Droegemeier, K.K., 1997: The numerical prediction of thunderstorms: Challenges potential benefits, and results from from real-time operational tests. *WMO Bulletin..*

Ellis, S., 1997: *Hole-filling Data Voids in Meteorological Fields*. Masters Thesis, University of Oklahoma, School of Meteorology, Norman, OK, 73019.

Fiedler, B., 1999: Storm surgery and phase correction in the ARPS and COAMPS coordinate system. Available from the author at CMRP, University of Oklahoma, 100 E. Boyd, Rm 1310, Norman, OK, 73019, or http://cmrp.ou.edu/~bfiedler/cmrp/index.html.

Fritsch, J.M. and C.F. Chappel, 1980: Numerical prediction of convectively driven mesoscale pressure systems. Part II: Mesoscale model. *J. Atmos Sci.*, **37**, 1734-1762.

Fulton, R.A., J.P. Breidenbach, D.-J. Seo, D.A. Miller, and T. O'Bannon, 1998: The WSR-88D rainfall algorithm. *Wea. and Forecasting*, **13**, 377-395.

Gal-Chen, T., 1978: A method for the initialization of the anelastic equations: Implications for matching models with observations. *Mon Wea. Rev.*, **106**, 587-696.

Gandin, L.S., 1963: *Objective Analysis of Meteorological Fields*, Gidrometeorol Izdat, St. Petersburg, Russia. (Translation published by Israel Program for Scientific Translations, Jerusalem, 1966), 266 pp.

Grammeltvedt, A., 1968: A survey of finite difference schemes for the primitive equations of a barotropic fluid. *Mon Wea. Rev.*, **97**, 384-404.

Hane, C.E. and B.C. Scott, 1978: Temperature and pressure perturbations within convective clouds derived from detailed air motion information: Preliminary testing. *Mon. Wea. Rev.*, **109**, 564-576.

Hoffman, R.N. and C. Grassotti, 1996: A technique for assimilating SSM/I observations of marine atmospheric storms with ECMWF analyses. *J. Appl. Metr.* , **35**, 1177-1188.

Hoffman, R.N., Z. Liu, J.-F. Louis and C. Grassotti, 1995: Distortion representation of forecast errors. *Mon. Wea. Rev.*, **123**, 2758-2770.

Ioannidou, L. and M.A. Pedder, 1999: Three-dimensional applications of a successive corrections analysis scheme to mesoscale observations. Mon. Wea. Rev., 127, 236-251.

Janjic', Z.I., 1984: Nonlinear advection schemes and energy cascade on semi-staggered grids. *Mon Wea. Rev.*, **112**, 1234-1245.

Kessler, E., 1969: On the distribution and continuity of water substance in atmospheric circulation. Meteor. Monogr., **10**, no. 32, AMS, Boston.

Kineman, J.J., 1992: *Global Ecosystems Database, Version 1 Users Guide, Key to Geophysical Records Documentation, No. 26*, USDOC/NOAA National Geophysical Data Center, Boulder, CO. 121 pp.

Klazura, G.E. and D. Imy, 1993: A description of the initial set of analysis products available from the NEXRAD WSR-88D system. *Bull. Amer. Meteor. Soc.* , **74**, 1293-1311.

Klemp, J.B., R.B. Wilhelmson and P.S. Ray, 1981: Observed and numerically simulated structure of a mature supercell thunderstorm. *J. Atmos. Sci.*, **38**, 1558-1580.

Klemp, J.B. and R. Rotunno, 1983: A study of the tornadic region within a supercell thunderstorm. *J. Atmos. Sci.*, **40**, 359-377.

Koch, S.E. and J. McCarthy, 1982: Evolution of an Oklahoma dryline. Part II: Boundary layer forcing of mesoconvective systems. *J. Atmos Sci.*, **39**, 237-257.

Kuo, Y-H, Y-R Guo, and E.R. Westwater, 1993: Assimilation of precipitable water measurements into a mesoscale numerical model. *Mon. Wea. Rev.*, **121**, 1215-1238.

Lazarus, S. A. Shapiro, and K. Droegemeier, 1999: Analysis of the Gal-Chen-Zhang single-Doppler velocity retrieval., *J. Atmos. Sci.* , **16**, 5-18.

Li, Y., 1994: *On the Topological Complexity of the Cost Function in Variational Data Assimilation*. Ph.D. Dissertation, Univ. of Oklahoma, School of Meteorology, Norman, OK 73019.

Lilly, D.K., 1990: Numerical predictions of thunderstorms -- has its time come? *Quart. J. Roy. Meteor. Soc.*, **116**, 779-798.

Lorenc, A.C., R.S. Bell and B. MacPherson, 1991: The Meteorological Office analysis correction data assimilation scheme. *Quart. J. Roy. Meteor. Soc.*, **117**, 59-89.

Mariano, A.J., 1990: Contour analysis, a new approach for melding geophysical fields. *J. Oceanic and Atmos. Technol.*, **7**, 285-295.

Mass, C.F., and Y-H Kuo, 1998: Regional real-time numerical weather prediction: current status and future potential. *Bull. Amer. Meteor. Soc.*, **79**, 253-263.

Mewes, J.J., 1997: *Quantitative Verification of Non-Hydrostatic Model Forecasts*. Masters Thesis, Univ. of Oklahoma School of Meteorology, Norman, OK. 205 pp.

NOAA, 1995: *Storm Data, June 1995*, Published by National Climatic Data Center, Asheville, NC, **37**, 178-179.

Noilhan, J., and S. Planton, 1989: A simple parameterization of land surface processes for meteorological models. *Mon. Wea. Rev.*, **117**, 536-549.

Parrett, C. A. and M. J. P. Cullen, 1984: Simulation of hydraulic jumps in the presence of rotation and mountains. *Quart. J. R. Met. Soc.*, **110**, 147-165.

Parrish, D.F., J. Purser, E. Rogers and Y. Lin, 1996: The regional 3D-variational analysis for the Eta model. Preprints, *11th Conf. on Num. Wea. Pred.*, Norfolk, VA, AMS. Boston.

Pielke, R. A. and M. Segal, 1986: Mesoscale circulations forced by differential terrain heating. In *Mesoscale Meteorology and Forecasting*, P. Ray, Ed., Amer. Met. Soc., Boston.

Purdom, J.F.W., 1982: Subjective interpretations of geostationary satellite data for nowcasting. In *Nowcasting*, K. Browning, Ed., Academic Press, London.

Qiu, C.J. and Q. Xu, 1992: A simple adjoint method of wind analysis for single-Doppler data. *J. Atmos. Oceanic Technol.*, **9**, 588-598.

Ramamurthy, M.K., R.M. Rauber, B.P. Collins, N.K. Malhotra, 1993: A comparative study of large-amplitude gravity-wave events. *Mon Wea. Rev.*, **121**, 2951-2974.

Rao, P.A., H.E. Fuelberg, and K.K. Droegemeier, 1999: High resolution modeling of the Cape Canaveral area land-water circulations and associated features.*Mon. Wea. Rev.*, **127**, 1808-1821.

Ray, P.S., B.C. Johnson, K.W. Johnson, J.S. Bradberry, J.J. Stephens, K.K. Wagner, R.B. Wilhelmson and J.B. Klemp, 1981: The morphology of severe tornadic storms on 20 May 1977. *J. Atmos. Sci.*, **38**, 1643-1663.

Rhea, J.O., 1966: A study of thunderstorm formation along dry lines. *J. Appl. Meteor.*, **5**, 58-63.

Rogers, E., D. Parrish, G.J. DiMego, 1998: Data assimilation experiments with the regional 3-D variational analysis at the National Centers for Environmental Prediction. Preprints, *12th Conf. on Num. Wea. Pred.*, Phoenix, AZ, AMS, Boston, 32-33.

Rogers, R.R. and M.K. Yau, 1989: *A Short Course in Cloud Physics.*, Pergammon Press, 293pp.

Sashegyi, K.D., D.E. Harms, R.V. Madala, S. Raman, 1993: Application of the Bratseth scheme for the analysis of GALE data using a mesoscale model. *Mon. Wea. Rev.*, **121**, 2331-2350.

Shapiro, A., T. Gal-Chen, J. Zhang, L. Zhao, Q. Xu, H. Gu, C-J Qiu, I. Zawadski, S. Laroche, and J. Tuttle, 1995a: Highlights from a single-Doppler velocity retrieval intercomparison project ("bake-off"). Preprints, *Sixth Conf. on Aviation Weather Systems*, Dallas, TX, AMS, Boston.

Shapiro, A., S. Ellis, and J. Shaw, 1995b: Single-Doppler velocity retrievals with Phoenix II data: clear air and microburst wind retrievals in the planetary boundary layer. *J. Atmos. Sci.* , **52**, 1265-1287.

Snook, J.S., 1998: Comments on "Regional real-time numerical weather prediction: current status and future potential." *Correspondence, Bull. Amer. Meteor. Soc.*, **79**, 2747-2748.

Stauffer, D.R., and N.L. Seaman, and F.S. Binkowski, 1991: Use of four-dimensional data assimilation in a limited-area mesoscale model. Part II: Effects of data assimilation within the planetary boundary layer. *Mon. Wea. Rev.*, **119**, 734-754.

Stauffer, D.R. and N.L. Seaman, 1994: Mesoscale four-dimensional data assimilation. *J. Appl. Meteor.*, **33**, 416-434.

Stensrud, D.J. and J.M. Fritsch, 1993: Mesoscale convective systesms in weakly forced large-scale environments, Part I: Observations. *Mon Wea. Rev.*, **121**, 3326-3344.

Strum, S., B. Fiedler, Z. Hou, 1999: Techniques for Interactive Data Assimilation, Preprints, *Third Conf. on Coastal Atmospheric and Oceanic Prediction and Processes,* New Orleans, LA, AMS, Bostorn, in press.

Sun, J., 1994: Fitting a Cartesian prediction model to radial velocity data from single-Doppler radar. *J. Atmos. Oceanic Technol.*, **11**, 200-204.

Sun, J. and N.A. Crook, 1994: Wind and thermodynamic retrieval from single-Doppler measurements of a gust front observed during Phoenix-II. *Mon Wea. Rev.*, **122**, 1075-1091.

Sun, J., D.W. Flicker, and D.K. Lilly, 1991: Recovery of three dimensional wind and temperature fields from simulated single-Doppler radar data. *J. Atmos. Sci.*, **48**, 876-890.

Sun, W. Y., and C. Z. Chang, 1986: Diffusion model for a convective layer. Part I: Numerical simulation of convective boundary layer. *J. Appl. Meteor.*, **25**, 1445-1453.

Tao, W.K. and J. Simpson, 1993: Goddard Cumulus Ensemble Model. Part I: Model description. *Terrestrial, Atmospheric and Oceanic Sciences*, **4**, 35-72.

Thiebaux, H. J. , P. R. Julian and G. J. DiMego, 1990: Areal versus collocation data quality control. *Preprints, International Symposium on Assimilation of Observations in Meteorology and Oceanography*, Clermont-Ferrond, France, WMO, Geneva, 255-260.

Ucelliini, L.W., 1975: A case study of apparent gravity wave initiation of convective storms. *Mon. Wea. Rev.*, **103**, 497-513.

Ucellini, L.W. and S.E. Koch, 1987: The synoptic setting and possible energy sources for meso-scale disturbances. *Mon. Wea. Rev.*, **115**, 721-729.

United States Department of Agriculture (USDA), 1994: *State Soil Geographic (STATSGO) Data Base, Data Use Information*, Miscellaneous Publication No. 1492, Natural Resources Conservation Service, Fort Worth , TX.

Wakimoto, R.M. and N.T. Atkins, 1994: Observations of the sea-breeze front during CaPE: Part 1: Single-Doppler, satellite and cloud photogrammetry analysis. *Mon. Wea. Rev.*, **122**, 1092-1114.

Weckworth, T.M. and R.M. Wakimoto, 1992: The initiation and organization of convective cells atop a cold-air outflow boundary. *Mon. Wea. Rev.*, **120**, 2169-2187.

Weygandt, S., A. Shapiro, and K.K. Droegemeier, 1998: The use of wind and thermodynamic retrievals to create initial forecast fields from single-Doppler observations of a supercell thunderstorm. Preprints, *16th Conf. on Wea. Anal. and Fore.*, Phoenix, AZ, Amer. Meteor. Soc., Boston.

Williams, R. T. and A. M. Hori, 1970: Formation of hydraulic jumps in a rotating system. *J. Geophys. Res.*, **75**, 2813-2821.

Wilson, J.W., J.B. Foote, N.A. Crook, J.C. Fankhauser, C.G. Wade, J.D. Tuttle and C.K. Mueller, 1992: The role of boundary-layer convergence zones and horizontal rolls in the initiation of thunderstorms: A case study. *Mon. Wea. Rev.*, **120**, 1785-1815.

Wilson, J.W., J.A. Moore, G.B. Foote, B. Martner, A.R. Rodi, T. Uttal, and J.M. Wilczak, 1988: Convection Initiation and Downburst Experiment (CINDE). *Bull. Amer. Meteor. Soc.*, 1328-1335.

Wilson, J.W. and C.K. Mueller, 1993: Nowcasts of thunderstorm initiation and evolution. *Wea. and Forecasting*, **8**, 132-146.

Wilson, J.W. and W. Schreiber, 1986: Initiation of convection by radar-observed boundary layer convergent lines. *Mon. Wea. Rev.*, **114**, 2516-2536.

Wong, V.C., M. Xue, K.K. Droegemeier, Y. Liu, X. Song, A. Sathye, M. Zou and L. Sun, 1994: Parameterization of physical processes in a storm scale model. Preprints, *Tenth Conf. on Num. Wea. Pred.*, Portland OR, AMS, Boston, J28-J31.

Wong, V., M. Xue, Y. Liu, X. Tan, L. Wang. and K. Droegemeier, 1998: Effect of land cover on the numerical prediction of convective storms. Preprints, *12th Conf. on Num. Wea. Prediction*, Phoenix, AZ, AMS, Boston, 157-158.

Xu, Q., Qiu, C-J, and J-X Yu, 1994a: Adjoint-method retrievals of low-altitude wind fields from single-Doppler reflectivity measured during Phoenix II. *J. Atmos. Oceanic Technol.*, **11**, 275-288.

Xu, Q., Qiu, C-J, and J-X Yu, 1994b: Adjoint-method retrievals of low-altitude wind fields from single-Doppler wind data. *J. Atmos. Oceanic Technol.*, **11**, 579-585.

Xu, Q., Qiu, C-J, Gu, H-D, and J-X Yu, 1995: Simple adjoint retrievals of microburst winds from single-Doppler data. *Mon. Wea. Rev.*, **123**, 1822-1833.

Xue, M., K.K. Droegemeier, V. Wong, A. Shapiro and K. Brewster, 1995: *ARPS Version 4.0 User's Guide*. 381 pp. Available from Center for Analysis and Prediction of Storms, University of Oklahoma, Norman, OK, 73019. http://www.caps.ou.edu

Xue, M., K. Brewster, K. K. Droegemeier, V. Wong, D. H. Wang, F. Carr, A. Shapiro, L. M. Zhao, S. Weygandt, D. Andra, and P. Janish, 1996: The 1996 CAPS spring operational forecasting period: Realtime storm-scale NWP. Part II: Operational summary and examples. Preprints, *11th Conf. on Num. Wea. Pred.*, Norfolk, VA, AMS, Boston, 297-300.

Zhang, J., F. Carr, and K. Brewster, 1998: ADAS cloud analysis. *Preprints, 12th Conf. on Num. Wea. Prediction*, Phoenix, AZ, AMS, Boston, 185-188.

Zhang, J. 1999: *Moisture and Diabatic Initialization Based on Radar and Satellite Observations*. Ph.D. Dissertation, Univ. of Oklahoma, School of Meteorology, Norman, OK, 73019.

Appendix A 12-km ARPS Input Variables

Table A.1 12-km Grid Options

Parameter	ARPS name	Value
grid spacing	dx,dy	12 km
domain size	nx,ny,nz	73,73,43
minimum dz	dzmin	20 m
average dz	dz	500 m
vertical stretching option	strhopt	2, tanh profile of dz
depth dz=const=dzmin	dlayer1	0.0 m
depth dz stretched	dlayer2	10000. m
stretch tuning parameter	strhtune	1.0
hgt of flat z	zflat	10000. m
center lat,lon	ctrlat,ctrlon	35.25, -97.00 (4/9/95) 35.75, -102.00 (6/8/95)
map projection	mapproj	2, Lambert Conformal
true latitudes	trulat1,trulat2	32.,40.
true longitude	trulon	-98. (4/9/95) -102. (6/8/95)
map factor option #1, #2	mfctropt,mptropt	1,1

Table A.2 12-km ARPS Runtime Options, Part 1

Parameter	ARPS name	Value
Increment Nudging		
nudging option	nudgopt	1, const over time window
nudging window	ndstop-ndstart	600 s
Numerics		
large time step	dtbig	12 s.
acoustic time step	dtsml	24 s.
acoustic numerics	vimplct	1, implicit method
pt on small step	ptsmlstp	0, no
speed of sound	csopt	csound=(cp/cv) R T
implicit wgt coef	tacoef	0.6
buoyancy option	buoyopt	1, buoyancy terms
second order buoyancy	buoy2nd	1, yes
remove density from pr gradient terms?	rhofctopt	0, no
Bousinessq approximation	bsnesq	0, no
pressure eq option	peqopt	1, normal
momentum advection	madvopt	2, fourth order horiz, second order vertical
scalar advection	sadvopt	2, fourth order horiz, second order vertical
Lateral Boundaries		
lateral boundary zone	ngbrz	5
relaxation half width	brlxhw	2.3 grid lengths
BC time interval	tintvebd	10800 s.
BC Damping coefficient	cbcdmp	0.001
Extra mixing in BC zone	cbcmix	1.0E-04
Coriolis option	coriopt	3, latitude-dependent horiz terms, no vertical terms
Geostrophic balance term	coriotrm	1, no geostrophic balancing, real data
Turbulence	tmixopt	4, Sun and Chen
Isotropic turbulence	trbisotp	0, no
TKE option	tkeopt	3, 1.5 order TKE
Implict vertical turbulence	trbvimp	1, implicit
Implicit turbulence coeff	alfcoef	1.0
Prandtl Number	prantl	1.0
Maximum Km	kmlimit	1.0

Table A.3 12-km ARPS Runtime Options, Part 2

Parameter	ARPS name	Value
Computational Mixing		
2nd order comp mix	cmx2nd	1, on
2nd order horiz coef	cfcm2h	0.
2nd order vert coef	cfcm2v	2.0e-04
4th order comp mix	cmx4th	1, on
4th order horiz coef	cfcm4h	5.0e-04
4th order vert coef	cfcm4v	0.
Scalar mixing factor	scmixfctr	0.5
Divergence damping	divdmp	1
divdmp horiz coef	divdmpndh	0.05
divdmp vert coef	divdmpndv	0.05
Rayleigh damping	raydmp	2
raydmp coef	cfrdmp	0.003333
raydmp begin hgt	zbrdmp	12 km
Asselin time filter	flteps	0.10
Moisture Option	mstopt	1, moist run
Microphysics Option	mphyopt	2, Tao Ice
Convection Parameterization	cnvctopt	0, none
Radiation	radopt	2
stagger radiation	radstgr	1
long-wave option	rlwopt	0, simple
radiation time step	dtrad	600 s.
Surface Physics	sfcphy	4
land-water drag distinction	landwtr	0
mom. drag coef land	cdmlnd	3.0e-03
mom. drag coef water	cdmwtr	1.0e-03
heat flux drag coef land	cdhlnd	3.0e-03
heat fux drag coef water	cdhwtr	1.0e-03
wv flux drag coef land	cdqlnd	3.0e-03
wx flux coef water	cdqwtr	0.7e-03
PBL depth option	pbldopt	2
length scale	lsclopt	0.20
flux distribution option	tqflxdis	1
depth of flux distribution	dtqflxdis	200. m
time step of sfc fluxes	dtsfc	60. s

Appendix B 3-km ARPS Input Variables

Table B.1 3-km Grid Options

Parameter	ARPS name	Value
grid spacing	dx,dy	3 km
domain size	nx,ny,nz	123,123,43
minimum dz	dzmin	20 m
average dz	dz	500 m
vertical stretching option	strhopt	2, tanh profile of dz
depth dz=const=dzmin	dlayer1	0.0 m
depth dz stretched	dlayer2	10000. m
stretch tuning parameter	strhtune	1.0
hgt of flat z	zflat	10000. m
center lat,lon	ctrlat,ctrlon	35.25,-97.00 (4/9/95) 35.8534, -100.9322 (6/8/95)
map projection	mapproj	2, Lambert Conformal
true latitudes	trulat1,trulat2	32.,40.
true longitude	trulon	-98. (4/9/95) -102. (6/8/95)
map factor option #1, #2	mfctropt,mptropt	1,1

Table B.2 3-km ARPS Runtime Options, Part 1

Parameter	ARPS name	Value
Increment Nudging		
nudging option	nudgopt	0, off
nudging window	ndstop-ndstart	600 s
Numerics		
large time step	dtbig	6 s.
acoustic time step	dtsml	6 s.
acoustic numerics	vimplct	1, implicit method
pt on small step	ptsmlstp	0, no
speed of sound	csopt	csound=(cp/cv) R T
implicit wgt coef	tacoef	0.6
buoyancy option	buoyopt	1, buoyancy terms
second order buoyancy	buoy2nd	1, yes
density in pr gradient term	rhofctopt	1, complete
Bousinessq approximation	bsnesq	0, no
pressure eq option	peqopt	1, normal
momentum advection	madvopt	2, fourth order horiz, second order vertical
scalar advection	sadvopt	4, Zalesak FCT
Lateral Boundaries		
lateral boundary zone	ngbrz	7
relaxation half width	brlxhw	2.0 grid lengths
BC time interval	tintvebd	1800 s.
BC Damping coefficient	cbcdmp	0.001
Extra mixing in BC zone	cbcmix	2.0E-04
Coriolis option	coriopt	3, latitude-dependent horiz terms, no vertical terms
Geostrophic balance term	coriotrm	1, no geostrophic balancing, real data
Turbulence	tmixopt	4, Sun and Chen
Isotropic turbulence	trbisotp	0, no
TKE option	tkeopt	3, 1.5 order TKE
Implict vertical turbulence	trbvimp	1, implicit
Implicit turbulence coeff	alfcoef	1.0
Prandtl Number	prantl	1.0
Maximum Km	kmlimit	1.0

Table B.3 3-km ARPS Runtime Options, Part 2

Parameter	ARPS name	Value
Computational Mixing		
2nd order comp mix	cmix2nd	1, on
2nd order horiz coef	cfcm2h	0.
2nd order vert coef	cfcm2v	2.0e-04
4th order comp mix	cmx4th	1, on
4th order horiz coef	cfcm4h	1.0e-03
4th order vert coef	cfcm4v	0.
Scalar mixing factor	scmixfctr	0.5
Divergence damping	divdmp	1
divdmp horiz coef	divdmpndh	0.05
divdmp vert coef	divdmpndv	0.05
Rayleigh damping	raydmp	2
raydmp coef	cfrdmp	0.003333
raydmp begin hgt	zbrdmp	13 km
Asselin time filter	flteps	0.10
Moisture Option	mstopt	1, moist run
Microphysics Option	mphyopt	2, Tao Ice
Convection Parameterization	cnvctopt	0, none
Radiation	radopt	2
stagger radiation	radstgr	1
long-wave option	rlwopt	0, simple
radiation time step	dtrad	300 s.
Surface Physics	sfcphy	4
land-water drag distinction	landwtr	0, land
mom. drag coef land	cdmlnd	3.0e-03
mom. drag coef water	cdmwtr	1.0e-03
heat flux drag coef land	cdhlnd	3.0e-03
heat fux drag coef water	cdhwtr	1.0e-03
wv flux drag coef land	cdqlnd	2.0e-03
wx flux coef water	cdqwtr	0.7e-03
PBL depth option	pbldopt	2, computed
length scale	lsclopt	0.20
flux distribution option	tqflxdis	1
depth of flux distribution	dtqflxdis	200. m
time step of sfc fluxes	dtsfc	60. s